Fermilab

FERMILAB-THESIS-2002-15

A Search for Large Extra Dimensions in the Jet + $\not\!\!E_T$ Final State in $\sqrt{s} = 1.8$ TeV $p\bar{p}$ Collisions at DØ

A Dissertation

Submitted to the Graduate School

of the University of Notre Dame

in Partial Fulfillment of the Requirements

for the Degree of

Doctor of Philosophy

by

Hai Zheng, M.S.

Randal C. Ruchti, Director

Department of Physics

Notre Dame, Indiana

April 2002

A Search for Large Extra Dimensions in the Jet + $\not\!\!E_T$ Final State in $\sqrt{s} = 1.8$ TeV $p\bar{p}$ Collisions at DØ

Abstract

by

This dissertation presents a search for evidence of large extra dimensions (LED) in $p\bar{p}$ collisions at a center of mass of 1.8 TeV using the DØ detector at the Fermilab National Accelerator Laboratory. Data corresponding to 78.8 $\pm$ 3.9 pb^{-1} are examined for events with large missing transverse energy, one high-p$_T$ jet, and the absence of isolated leptons. No events are observed in excess of the Standard Model background predictions. Limits are placed on the LED fundamental mass scale M_D for n = 2, 3, 4, 5, 6, and 7.

CONTENTS

TABLES

FIGURES

ACKNOWLEDGEMENTS

First of all, high energy physics experiment is a huge team effort and my appreciation goes to everyone who has worked on the experiment and made this analysis possible. And thanks to the people of high-energy group at Notre Dame, who have helped me in innumerable ways. Several require special mention. Thanks to my advisor, Prof. Randy Ruchti, for all the kindness and patience and wisdom he has given to me over the years. And I am grateful to people in the New Phenomena Group, who instructed me on the proper way to do a physics analysis, especially Prof. Greg Landsberg, whose insight and knowledge has been crucial to this dissertation. And thanks to Prof. Tom Ferbel and my EB members for comment, criticism and encouragement. Many thanks to Evegeny Popkov, Chris Hays, John Zhou, and Daniel Karmgard for always being there to answer my questions and help me through the analysis. I would also like to thank Chrisina Hebert, Brian Connolly, and Maria Sorin for spending time and energy to help me go through the struggle of Run I analyses in the end stage when resources are hard to come by.

I could not thank more to teachers and friends who inspired me to take this path of scientific research and continued to support me through this arduous journey. I am indebted in many ways to professors and teachers at the University of Science and Technology of China, who gave me a solid fundation in physics education and scientific methodology. My special thanks go to Prof. Zizong Xu, Prof. Hongfang Cheng, and Prof. Chen Li, who showed me the dedication and determination that needed to be a true researcher. I would also like to thank Zhiping Zhong, who I met during my undergraduate years, and later became both my role model and my best friend. It was she who encouraged me to challenge myself to achieve the goal of graduating a year ahead of schedule and going abroad for my continuous academic advancement. Without her support, I would never have made it into a reality. In my early years, my high school physics teacher Guangyin Yang, opened my eyes to the fascinating world of nature and encouraged me to pursue physics as my life time goal. And Zhiyi Zhang, another high school teacher of mine, always urged me to do my best and to embrace a larger outside world. The kindness and patience of my primary school teacher Shuyuan Zhou, helped me to become a good student. Without these people, I can never reach what I have achieved now.

Last but not least, I would like to thank my parents whose sacrifice for me is beyond words. I owe this to them. Also I dedicate this to my grandparents. Physics, the dream of three generations in my family is in realization.

CHAPTER 1

INTRODUCTION

It is in the nature of human being to try and understand the world around us, to gain knowledge, and to explore. Whether it is the ancient philosophers or the modern scientists, the desire is the same. At the frontier of science, high energy physics (HEP or particle physics) tries to unveil the structure of the universe itself. To understand what the basic building blocks (fundamental particles) of the world are, how they interact with each other, and why they behave like this, generation after generation of physicists devoted their lives to solving this ultimate puzzle.

The Standard Model (SM), a theory that describes what are believed to be the fundamental particles and their interactions, has been a good description of nature . It is in very good agreement with high energy physics experimental data[1].

The Standard Model includes the unified theory of weak and electromagnetic interactions (Electroweak Theory) and the theory of strong interactions (Quantum Chromodynamics or QCD). The SM Lagrangian $\mathcal{L}$ is:

$$
\begin{aligned}
\mathcal{L} = & \; \overline{q}\gamma^{\mu}(i\partial_{\mu} - g_s T_a G^a_{\mu})q - \frac{1}{4}G^a_{\mu\nu}G^{\mu\nu}_a \\
& + \overline{L}\gamma^{\mu}\left(i\partial_{\mu} - \frac{g}{2}\boldsymbol{\tau}\cdot\mathbf{W}_{\mu} - \frac{g'}{2}B_{\mu}Y\right)L \\
& + \overline{R}\gamma^{\mu}\left(i\partial_{\mu} - \frac{g'}{2}B_{\mu}Y\right)R \qquad (1.1) \\
& - \frac{1}{4}W_{\mu\nu}W^{\mu\nu} - \frac{1}{4}B_{\mu\nu}B^{\mu\nu} \\
& + \left|\left(i\partial_{\mu} - \frac{g}{2}\boldsymbol{\tau}\cdot\mathbf{W}_{\mu} - \frac{g'}{2}B_{\mu}Y\right)\phi\right|^2 - V(\phi) \\
& - G_e\left(\overline{L}\phi R + \overline{R}\phi^{\dagger}L + h.c.\right). \qquad (1.2)
\end{aligned}
$$

The SM Lagrangian in Equation 1.2 observes the $\mathrm{SU}(3)_C \otimes \mathrm{SU}(2)_L \otimes \mathrm{U}(1)_Y$ symmetry[1]. The first line describes the strong interaction, which has a strong coupling constant g_s and involves the gluon gauge field. The second, third and fourth lines describe the electroweak interaction, which has the coupling constants g and g', respectively, and involves electroweak gauge fields W and B. The SM could be completely formulated with these four lines had the masses of the particles in the theory been zero. In order to generate mass, the SM spontaneously breaks[2] its own symmetry through a mechanism called the Higgs mechanism[3]. The fifth line introduces two $\mathrm{SU}(2)_L \otimes \mathrm{U}(1)_Y$ gauge invariant terms for a scalar field (the Higgs), with the second term $V(\phi)$ being the Higgs potential. If the Higgs potential happens to be in the right form, e.g.,

$$
V(\phi) = \mu^2\phi^{\dagger}\phi + \lambda(\phi^{\dagger}\phi)^2, \qquad (1.3)
$$

with $\mu^2 < 0$ and $\lambda > 0$, the W and B field will mix to give rise to three massive gauge bosons, the $W^{\pm}$ and Z, and one massless gauge boson, the photon. The sixth line describes the Yukawa coupling between the fermions and the scalar field. This

[1]C stands for color, L stands for weak-isospin, and Y stands for weak-hypercharge.

Yukawa coupling gives mass to the fermions.

Some characteristics of the SM particles are shown in Table 1.1 and Table 1.2. The particle content of the Standard Model can be broken down into the categories of quarks, leptons, gauge bosons. Quarks and leptons are fermions that are respectively affected and unaffected by the strong force. They can be grouped into three generations according to their charge, mass and interaction pattern. The gauge bosons represent some quantized state of the electromagnetic, weak or strong fields.

The Standard Model (SM) is a great achievement in understanding of the fundamental particles and the forces of nature. However, there are some inconsistencies, such as the great disparity (the hierarchy problem) between the energy scale at which the weak and electromagnetic forces fuse together ($\sim 10^2$ GeV) and the energy scale at which gravity joins up with the other forces ($\sim 10^{19}$ GeV), which it cannot explain. Recent developments in string theory introduced the large extra dimensions (LED[2]) to solve the hierarchy problem. The topic of this dissertation is a search for the evidence of LED through the jet and missing transverse energy channel.

Chapter 2 describes the theory examined, Chapter 3 the apparatus used, Chapter 4 event reconstruction and particle identification, Chapter 5 shows the analysis techniques and Chapter 6 gives the results. Chapter 7 draws some conclusions.

[2]The author recoganizes this is the same abbreviation with light emitting diode. In this dissertation, LED always refers to large extra dimensions.

TABLE 1.1. QUARKS AND LEPTONS OF THE STANDARD MODEL. EACH PARTICLE HAS ITS ANTI-PARTICLE WITH EQUAL MASS AND EQUAL PHYSICAL PROPERTIES BUT OPPOSITE CHARGE.

Generation	Particle	Name	Mass (MeV/c^2)	Charge (e)
Quarks (spin 1/2)				
1	d	Down	~7.5	-1/3
1	u	Up	~4.2	2/3
2	s	Strange	~150	-1/3
2	c	Charm	~1100	2/3
3	b	Bottom	~4200	-1/3
3	t	Top	~174,000	2/3
Leptons (spin 1/2)				
1	e	Electron/positron	0.511	-1
1	ν_e	Electron neutrino	<15 eV	0
2	μ	Muon/antimuon	105	-1
2	ν_μ	Muon neutrino	<0.17	0
3	τ	Tau/antitau	1777	-1
3	ν_τ	Tau neutrino	<24	0

TABLE 1.2. GAUGE BOSONS OF THE STANDARD MODEL. PHOTON, GLUON AND Z ARE THEIR OWN ANTI-PARTICLES WHILE W_+ AND W_- ARE ANTI-PARTICLES OF EACH OTHER.

Particle	Name	Force	Mass (GeV/c^2)	Charge (e)
Gauge Bosons (spin 1)				
γ	Photon	Electromagnetic	0	0
g	Gluon	Strong	0	0
$W^\pm$	W	Weak	80.2	±1
Z	Z	Weak	91.2	0

CHAPTER 2

THE THEORIES

2.1 Motivation for New Physics

The Standard Model certainly has been a great achievement in particle physics. Nearly every feature of the theory has been confirmed by experimental results to a high degree of precision. However, the Standard Model still has some problems it cannot solve, such as the hierarchy problem. In nature, there are at least two seemingly fundamental energy scales, the electroweak scale $m_{EW} \sim 10^2$ GeV and the Planck scale $M_P = G_N^{-1/2} \sim 10^{19}$ GeV, where gravity becomes as strong as gauge interactions. Explaining the smallness and radiative stability of the hierarchy $m_{EW}/M_P \sim 10^{-17}$ has relied on low energy supersymmetry or technicolor. In recent years, a new framework for solving the hierarchy problem was proposed by introducing large extra spatial dimensions. The previously unreachable Planck, string and grand unification scales (M_P, M_S and M_{GUT}) may be brought down to the TeV scale. The observed weakness of gravity at long distances is postulated to be due to the existence of sub-millimeter spatial dimensions. In this picture the Standard Model fields are localized to a (3+1)-dimensional wall or "3-brane", while the graviton freely propagates in the extra dimensions. The hierarchy problem becomes isomorphic to the problem of the largeness of the extra dimensions.

In recent years, Arkani-Hamed, Dimopoulos and Dvali[4] have made the proposal that while the SM particles are confined to a 3-brane, as expected in string theory, and SM gauge interactions are therefore restricted to this brane, gravity can propagate in a higher-dimensional space. The relative feebleness of gravity with respect to weak forces is related to the size of the compactified extra dimensions, which is very large in units of TeV^{-1}. Newton's constant measured in the 3+1-dimensional space can be expressed as[4][5]

$$G_N^{-1} = 8\pi R^n M_D^{2+n}. \tag{2.1}$$

where $M_D \sim$ TeV is the fundamental mass scale, n is the number of extra dimensions, and R is the radius of the compactified space, here assumed to be a torus. The hierarchy problem is overcome because there is a single fundamental mass scale M_D, to be identified with the weak scale.

Therefore,

$$R = \frac{1}{\sqrt[n]{8\pi} M_D}(M_P/M_D)^{2/n}. \tag{2.2}$$

Assuming that the fundamental mass scale $M_D \sim 1$ TeV,

$$R \propto \begin{cases} 1.2 \times 10^{12} \text{ m} & n = 1, \\ 0.48 \text{ mm} & n = 2, \\ 3.6 \text{ nm} & n = 3, \\ 9.7 \times 10^{-12} \text{ m} & n = 4. \end{cases} \tag{2.3}$$

For $n = 1$, R is very large (of the size of our solar system), which is ruled out by the known $1/r^2$ dependence of the gravitational force at large distances. As for the $n = 2$ case, the current limit is $R < 0.19$ mm[6] as shown in Figure 2.1. This is the 95% confidence level upper limit on $1/r^2$-law violating interactions of the general expression of the Newtonian gravitational potential[6],[7]:

$$v(r) = -G\frac{m_1 m_2}{r}(1 + \alpha e^{-r/\lambda}). \tag{2.4}$$

The simplest scenario with two large extra dimensions predicts $\lambda = R$ and $\alpha = 3$ or $\alpha = 4$ for compactification on a 2-sphere or a 2-torus, respectively[7]. In

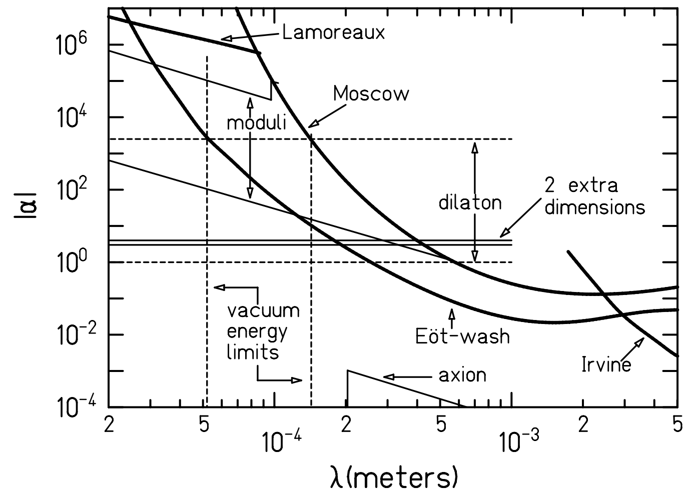

Figure 2.1. 95% confidence upper limits on $1/r^2$ - law violating interactions of the form given by Eq. 2.4 by E.Adelberger *et al.* and previous work[6].

Figure 2.1, the intersection point of the 2 extra dimensions noted by the double line and the heavy line labeled by Eöt-wash gives us the $\lambda = R < 0.19$ mm. For $n > 2$, it is completely out of the reach of direct gravitational measurements and the compactification radius drops as a power law.

The stringent astrophysical bounds on M_D come from the requirement that graviton emission does not rapidly cool the hottest system, SN1987A, preventing the occurrence of the observed neutrino flux. This bound has been estimated to be about $M_D \gtrsim 10^{\frac{15-4.5n}{n+2}}$ TeV[4], i.e. 30 TeV for $n = 2$ and 2 TeV for $n = 3$. Therefore, the astrophysical constraint excludes observable signals for $n = 2$, and limits the available region for $n > 2$. Nevertheless, even for $n = 2$, it is still interesting to have independent laboratory tests.

By first compactifying the higher-dimensional theory and constructing a 3+1-dimensional low-energy effective field theory of the graviton Kaluza-Klein (KK) excitations and their interactions with ordinary matter, the consequences of the supposition that the observed smallness of Newton's constant is a consequence of the large compactified volume of the extra dimensions could be investigated[5][8]. From the point of view of a 3+1 dimensional space time, a graviton in the extra dimensions is equivalent to a tower of an infinite number of Kaluza-Klein states with mass splittings $M_{KK} = 2\pi/R$, which is $M_k = 2\pi k/R$ ($k = 0, 1, 2, ..., \infty$). While each of these KK modes is very weakly coupled ($1/M_P$), their high multiplicity can give a large enhancement to any effect they mediate. The overall coupling becomes proportional to $1/M_D$. Since M_D is in the TeV range, the gravitational interaction is as strong as the electroweak interaction. The mass of each KK mode corresponds to the modulus of its momentum in the direction transverse to the brane. The picture of a massless graviton propagating in $D = 4 + n$ dimensions and the picture of massive KK gravitons propagating in four dimensions are equivalent.

2.2 Graviton Production and Collider Experiments

The different excitations of graviton KK modes have mass splittings[5]

$$\Delta m \sim \frac{1}{R} = M_D(\frac{M_D}{\overline{M}_P})^{2/n} \sim (\frac{M_D}{\mathrm{TeV}})^{\frac{n+2}{2}} 10^{\frac{12n-31}{n}} \mathrm{eV}, \tag{2.5}$$

where $\overline{M}_P$ is the reduced Planck mass, $\overline{M}_P = M_P/\sqrt{8\pi}$. With $M_D = 1$ TeV and n = 4, 6, 8, $\Delta m = 20$ keV, 7 MeV, and 0.1 GeV, respectively. The mass splitting only becomes comparable with the experimental energy resolution for a large number of extra dimensions, but then only a small number of KK modes can be produced and the total cross section is negligible. When the number of extra dimensions is not too large, the enormous number of accessible KK modes can compensate the $1/\overline{M}_P^2$ factor in the scattering amplitude, and it is the case of interest.

For experimental applications, it is convenient to describe the relevant observables for graviton production in terms of the inclusive cross sections. For not too large n, Δm is small enough that the sum over the different KK states can be replaced by a continuous integration. The differential cross section of inclusive graviton production is[5]:

$$\frac{d^2\sigma}{dt\ dm} = S_{n-1}\frac{\overline{M}_P^2}{M_D^{2+n}}m^{n-1}\frac{d\sigma_m}{dt}, \tag{2.6}$$

where S_{n-1} is the surface of a unit-radius sphere in n dimensions,

$$S_{n-1} = \frac{2\pi^{n/2}}{\Gamma(n/2)}, \tag{2.7}$$

and $d\sigma_m/dt$ is the differential cross section for producing a single KK graviton of mass m.

From the point of view of the D-dimensional theory, the cross section for an initial brane state $|p_1,\, p_2\rangle$ to go in a final brane state $|f\rangle$ plus a bulk graviton $|G\rangle$ is then

$$d\sigma = \frac{S_{n-1}m^{n-1}dm}{M_D^{2+n}}|\langle f, G|T^{\mu\nu}h_{\mu\nu}|p_1, p_2\rangle|^2(2\pi)^4\delta^4(P_i - P_f)\frac{d\Phi_f}{F(p_1, p_2)}, \tag{2.8}$$

where $T^{\mu\nu}$ is the energy-momentum tensor, $d\Phi_f$ is the brane final state phase space, and $F(p_1, p_2)$ is the usual flux factor for two particle collision. This equation agrees with Equation 2.6[5].

In hadron collisions, the leading graviton production comes from the subprocess $qg \longrightarrow qG$, $q\overline{q} \longrightarrow gG$, and $gg \longrightarrow gG$, as shown in Figure 2.2.

The differential cross sections for these parton processes are

$$\frac{d\sigma_m}{dt}(q\overline{q} \longrightarrow gG) = \frac{\alpha_s}{36}\frac{1}{s\overline{M}_P^2}F_1(t/s, m^2/s), \tag{2.9}$$

$$\frac{d\sigma_m}{dt}(qg \longrightarrow qG) = \frac{\alpha_s}{96}\frac{1}{s\overline{M}_P^2}F_2(t/s, m^2/s), \tag{2.10}$$

$$\frac{d\sigma_m}{dt}(gg \longrightarrow gG) = \frac{3\alpha_s}{16}\frac{1}{s\overline{M}_P^2}F_3(t/s, m^2/s), \tag{2.11}$$

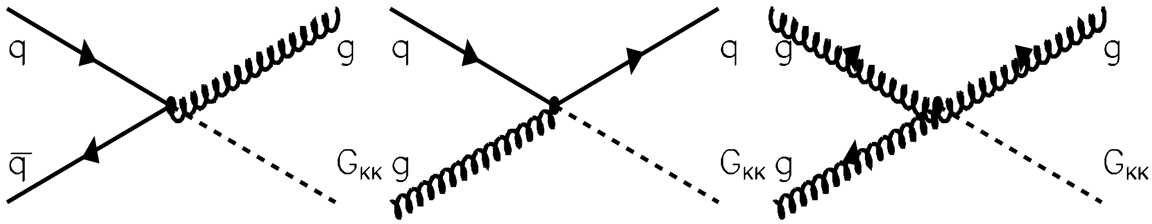

Figure 2.2. Feynman diagrams of subprocesses for leading experimental signal of graviton production.

where the Mandelstam variable t in $qg \longrightarrow qG$ is defined as $t = (p_q - p_G)^2$, and the functions F_1, F_2, and F_3 are:

$$F_1(x, y) = \frac{1}{x(y-1-x)}[-4x(1+x)(1+2x+2x^2)+ \\ y(1+6x+18x^2+16x^3) - 6y^2x(1+2x) + y^3(1+4x)], \tag{2.12}$$

$$\begin{aligned} F_2(x, y) &= -(y-1-x)F_1(\frac{x}{y-1-x}, \frac{y}{y-1-x}) \\ &= \frac{1}{x(y-1-x)}[-4x(1+x^2) + y(1+x)(1+8x+x^2) \\ &- 3y^2(1+4x+x^2) + 4y^3(1+x) - 2y^4], \end{aligned} \tag{2.13}$$

$$F_3(x, y) = \frac{1}{x(y-1-x)}[1+2x+3x^2+2x^3+x^4-2y(1+x^3) \\ + 3y^2(1+x^2) - 2y^3(1+x) + y^4]. \tag{2.14}$$

For the real graviton emission, the production cross section ranges from 10^{-2} pb to 10^2 pb for different values of n and M_D, which will be shown in Section 5.6 for the kinematic region we choose. In Figure 2.3, the total cross sections for $p\overline{p} \to$ jet + $\not{E}_T$ at $\sqrt{s} = 2$ TeV as a function of $\mathrm{E}_{T,\mathrm{jet}}^{\mathrm{min}}$ with $M_D = 1.2$ TeV fixed, and $|\eta_d| < 3$ are shown. The curves denoted by the symbol **a**, are the result of setting to zero the cross sections in Equations 2.9 - 2.11 whenever the effective center-of-mass energy in the parton collision $\sqrt{\hat{s}}$ is larger than M_D. The curves denoted by the symbol **b**, allow the cross sections grow indefinitely with $\sqrt{\hat{s}}$. This shows the applicability of the effective-theory approach. In the regions where the two curves almost coincide, the dominant contribution comes from momenta smaller than M_D and the effective theory is fully applicable. When the curves go apart, the ultraviolet contributions become important, and the calculation is not under control. And the higher the value of $\mathrm{E}_{T,\mathrm{jet}}^{\mathrm{min}}$, the larger the difference between the two curves becomes. The existence of a calculable perturbative region insensitive to the ultraviolet is related to the rapid decrease in the parton luminosities with increasing $\sqrt{\hat{s}}$ which more than compensates for the increase in the cross sections in Equations 2.9 - 2.11. The larger the value of n (δ in Figure 2.3), the faster the increase in the cross section, and thus the sooner the non-perturbative region is reached. Also the signal is flatter with increasing $\mathrm{E}_{T,\mathrm{jet}}^{\mathrm{min}}$ than the SM background, so it is helpful to go as high in E_T as is allowed while still having enough events for a statistically significant signal.

Gravitons couple to matter only gravitationally, but the $1/\overline{M}_P^2$ suppression present in their production cross section can be compensated by the large multiplicity of the KK modes or, in other words, by the D-dimensional phase-space factor. On the other hand, the $1/\overline{M}_P^2$ suppression in the graviton decay rate into ordinary matter is not compensated by the phase space and thus its lifetime is $\tau_G \sim \overline{M}_P^2/m^3 \sim (\mathrm{TeV}/m)^3 \times 10^3$ seconds with graviton mass m[5]. The $1/\overline{M}_P^2$ suppression factor can be also interpreted as the small probability that a graviton propagating in the D-dimensional space crosses the three-dimensional brane.

For experimental purposes, this means that the KK graviton behaves like a massive, non-interacting, stable particle and its collider signature is imbalance in final

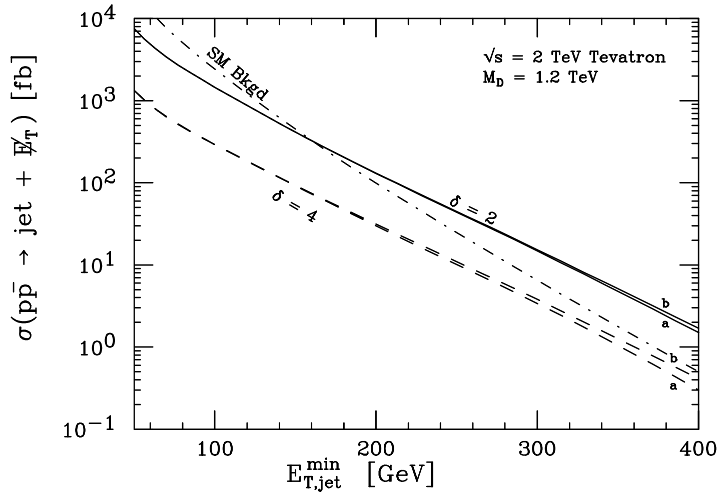

Figure 2.3. The total jet + $\not{E}_T$ cross section at the Tevatron ($\sqrt{s} = 2$ TeV) integrated for all $\mathrm{E}_{T,\mathrm{jet}} > \mathrm{E}_{T,\mathrm{jet}}^{\mathrm{min}}$ with the requirement that $|\eta_{\mathrm{jet}}| < 3.0$. The Standard Model background is the dash-dotted line, and the signal is plotted as solid and dashed lines for fixed $M_D = 1.2$ TeV with δ (n in this analysis) = 2 and 4 extra dimensions. The **a** (**b**) lines are constructed by integrating the cross section over $\widehat{s} < M_D^2$ (all $\widehat{s}$)[5].

state momenta and missing mass. The graviton has a continuous distribution in mass described by Equation 2.6. This mass distribution corresponds to the probability of emitting gravitons of different momenta into the extra dimensions. This is a specific feature of the graviton signal relative to any other new processes. Also for graviton production in the perturbative regime, each extra particle in the final state is associated with an extra suppression factor, so the missing energy signal is unlikely accompanied by a variety of leptons, photons, and hadronic activity coming from the decay of heavier particles. The emission of a single graviton into the extra dimensions violates momentum conservation along the directions transverse to the brane since translational invariance in the D-dimensional space is broken by the presence of the brane. From a four-dimensional point of view, energy and momentum are conserved, but the KK gravitons can have any arbitrary mass smaller than about M_D[5].

For this analysis, since the graviton escapes into extra dimensions, it results in a large missing transverse energy ($\not{E}_T$) signature in the DØ detector, while the quark or gluon will be presented as a high E_T jet in the detector system. Therefore, the search signature is an event with a large E_T jet and high $\not{E}_T$. The main and irreducible physics background is $Z(\nu\nu)+$ jets. In addition, there are also important instrumental backgrounds from jet mismeasurement, cosmic rays, etc.

CHAPTER 3

THE EXPERIMENTAL APPARATUS

The data set is produced using the Fermilab Tevatron I accelerator system and the DØ detector. The DØ detector measures the final state particles of high energy $p\bar{p}$ initial state collisions in the Tevatron at the Fermi National Accelerator Laboratory in Batavia, Illinois. The detector is named for its location, the DØ interaction region, which is one of the two high-luminosity beam crossing locations in the Tevatron.

3.1 The Accelerator

The accelerator[9] consists of several stages that progressively increase the energy of protons and antiprotons. Different apparatuses are used to accomplish the acceleration in different stages. A detailed description of the Tevatron may be found elsewhere;[10] here we describe it briefly. Figure 3.1 shows the layout of the system of Fermilab accelerator.

3.1.1 The Preaccelerator

The acceleration process begins with the release of hydrogen gas into a "magnetron surface-plasma source" as shown in Figure 3.2, which adds electrons to the hydrogen

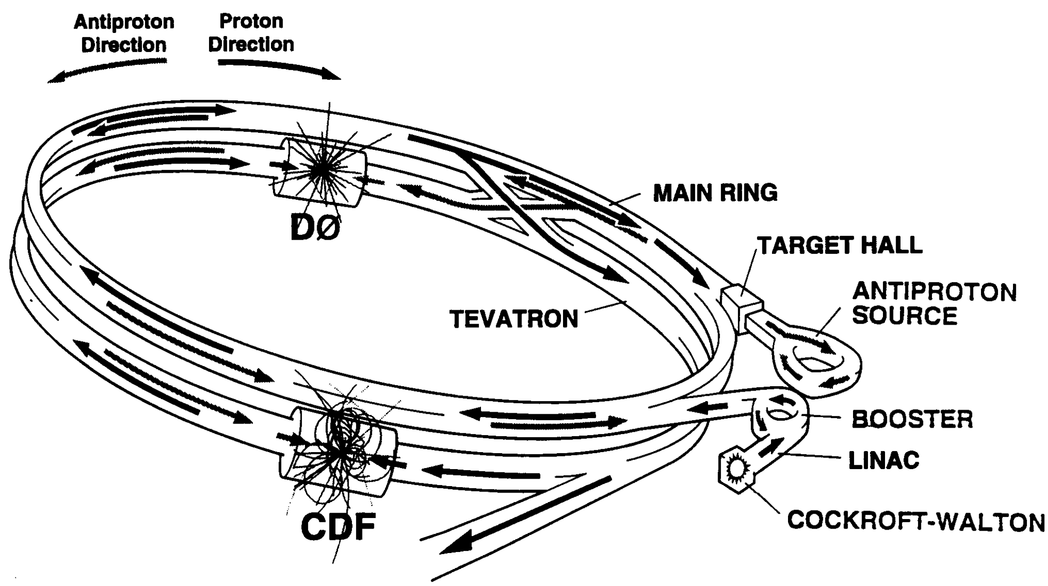

Figure 3.1. Schematic overview of the Fermilab accelerator complex.

atoms. The magnetron source uses an electric field to attract protons to the surface of a cathode. The protons collect electrons from the cathode and are disengaged by the stream of bombarding atoms. A magnetic field causes the negatively charged ions to spiral out the opposite side of the magnetron source. An "extractor plate" accelerate the ions to a kinetic energy of 18 keV. And a Cockcroft-Walton accelerator propels the H^- ions to an energy of 750 keV.

3.1.2 The Linac

The ions are then injected into a linear accelerator (the Linac) where they are accelerated to an energy of 400 MeV (was 200 MeV in Run Ia). The Linac consists of two segments which use the same method of acceleration to increase the energy of ions by step. An electric field pulls a group of ions through a beam tube. Then the

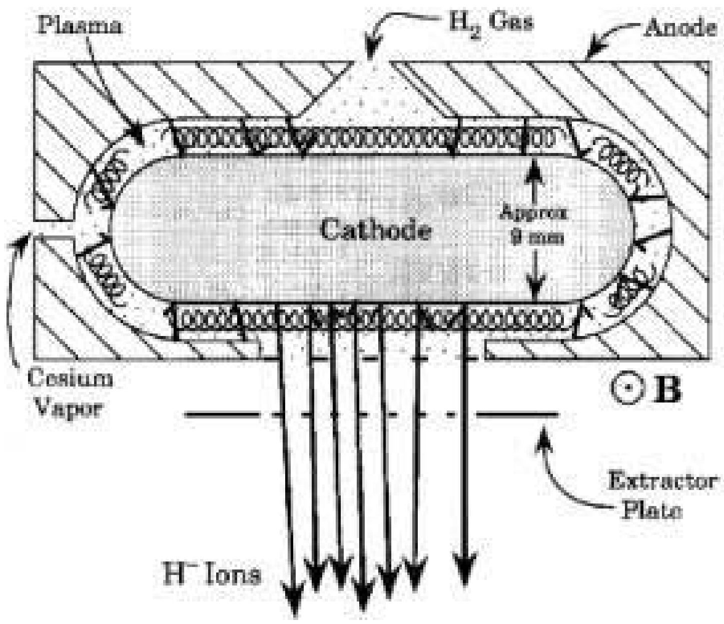

Figure 3.2. The magnetron source used to create negatively charged hydrogen ions from hydrogen gas.

field switches polarity, preventing more ions from entering the tube. The alternating fields produce a localized “bunch” of ions. After accelerating through the electric field, the ion bunch coasts through a shielded drift tube, continuing through the accelerator during the electric field reversal. When the ions reach the end of the tube, the electric field reverses again, providing another incremental boost to the ions. This step by step increase in acceleration occurs in both segments of the linear accelerator over a distance of 130 m.

3.1.3 The Booster

When the ions enter the Booster, a circular synchrotron nearly half a kilometer around, they are “debunched”, returning to a steady beam of particles. The beam passes through a thin carbon foil to strip off the electrons, leaving a beam of H^+ ions, which are bare protons. The steady beam of protons travels around the Booster, collecting more protons with each turn. After six revolutions, the Booster contains $\sim 3 \times 10^{12}$ protons, and the Linac ceases its supply. The Booster then restores the bunch structure to the beam and accelerates the protons to an energy of 8 GeV.

When the proton energy reaches 4.2 GeV, a precise "transition" in the alternating electric fields must occur in the Booster to keep the beam stable. Before the transition, a set of magnets along the beam line keeps the protons in orbit, and the alternating electric field forces the protons into bunches. However, at the transition energy, the bunch structure would destabilize without a precise shift in the timing of the alternating electric field cycle. The Booster institutes this shift, but during its application the proton beam undergoes a brief moment of instability.

3.1.4 The Main Ring

From the Booster the 8 GeV protons are injected into a larger synchrotron, the Main Ring. The Main Ring resides in an underground tunnel and is 6.3 kilometers in circumference. It provides a 120 GeV proton beam for the production of antiprotons; and it accelerates protons and antiprotons from an energy of 8 GeV to an energy of 150 GeV which are injected into the Tevatron.

The extracted 120 GeV protons are directed onto a nickel target disk to produce antiprotons. For about every 10^5 protons incident, one antiprotons results. The antiprotons are produced with a wide range of momenta. They are focused and stored in the Debuncher and Accumulator rings, where the beams are 'cooled', creating a beam of 8 GeV antiprotons to be injected into the Main Ring, and accelerated to 150 GeV. The 150 GeV antiprotons are injected into the Tevatron in the direction opposite to the proton beam.

In order to increase the numbers of protons and antiprotons in their respective bunches which in turn will increase the luminosity of collisions, the Main Ring coalesces groups of fifteen proton bunches and eleven antiproton bunches; these are the largest groups that can be coalesced while keeping the beams stable. After the coalescing procedure, proton bunches contain 1.5×10^{11} protons, while antiproton bunches contain 5.0×10^{10} antiprotons.

As with the Booster, the Main Ring provides the necessary electric field shift to maintain beam stability through transition when the protons and antiprotons have an energy of 17.6 GeV.

3.1.5 The Tevatron

The Tevatron is in the same tunnel as the Main Ring about two feet below and has the same circumference of 6.3 kilometers. In the Tevatron, the beams are accelerated to 900 GeV. It contains superconducting magnets and can achieve greater magnetic fields and thus greater beam energies. Nearly 1,000 superconducting magnets operating at a temperature of 4.6°Kelvin (-268.4°C) provide a field of 4.2 Tesla. The conventional magnets in the Main Ring can provide only about 1.8 Tesla (corresponding to a beam energy of 400 GeV).

The Tevatron can hold more than a thousand bunches, but it operates with only six bunches of protons and antiprotons (more concurrent bunches can lead to instabilities, particularly in the antiproton beam). Along the Tevatron ring are two high-luminosity collision regions, called BØ and DØ. At these locations, special superconducting magnets focus the beam to a height and width of 40 μm each (the height and width in the nonluminous region are 1.3 mm each). The proton and antiproton beams cross in these luminous regions and the beam focusing results in a substantial increase in luminosity. In each luminous region, the beams cross at a rate of nearly 300,000 per second. Experimental detectors are installed at these regions: CDF located at BØ and DØ located at DØ.

The data used in this analysis were taken during the 1994-1996 run of the Tevatron (Run 1B and Run 1C). Figure3.3 shows the integrated luminosity delivered by the Tevatron and that recorded by the DØ detector during Run I.

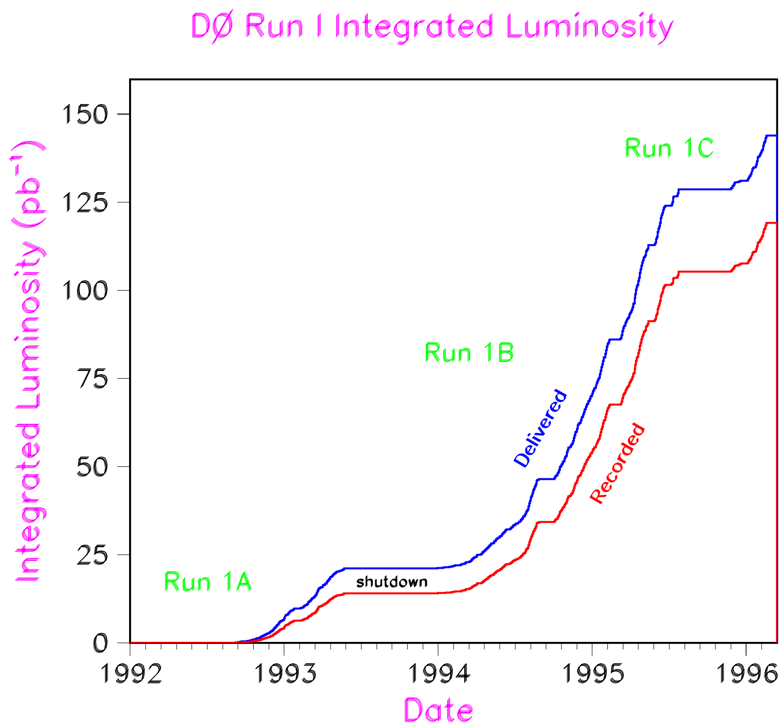

Figure 3.3. The integrated luminosity delivered by the Tevatron and recorded by the DØ detector in Run I[11].

3.2 The DØ Detector

The DØ detector is a general purpose collider detector designed, constructed and used by a collaboration of hundreds of physicists and engineers. It weighs approximately 5,500 tons and stands 13 meters in height and 20 meters in length. It is optimized for high p_T physics, for identification of both muons and electrons over a large solid angle, and for good jet and missing transverse energy measurement. Figure 3.4 shows a cut-away view of the DØ detector.

The detector consists of three major systems. From the inside out, they are the central tracking system, the calorimeter, and the muon detector. They are concentric to the beam line. Of primary importance in this analysis is the hermeticity of the calorimetry, which is crucial for good measurement of $\not{E}_T$. A detailed description of the detector is available in reference[10] and references therein; in this chapter we give a brief overview of the detector elements.

3.2.1 The DØ Coordinate System

DØ Collaboration has defined a standard right-handed coordinate system; this system shall be used throughout this dissertation. As shown in Figure 3.5, the system defines $+\hat{x}$ to be a unit vector pointing radially outward (east in the figure) from the center of the accelerator ring, $+\hat{y}$ to be a unit vector pointing vertically upward, and $+\hat{z}$ to be orthogonal to both such that the system is right-handed; this direction is also called 'south'. Protons from the accelerator move through the detector in the $+\hat{z}$ direction, and antiprotons in the $-\hat{z}$ direction. We also frequently use a spherical coordinate system, with the polar angle theta (θ) defined as the angle from the $+\hat{z}$ axis, and the azimuthal angle phi (ϕ) defined as the angle around the $+\hat{z}$ axis with $\phi = 0$ being the $+\hat{x}$ direction and $\phi = \pi/2$ being the $+\hat{y}$ direction.

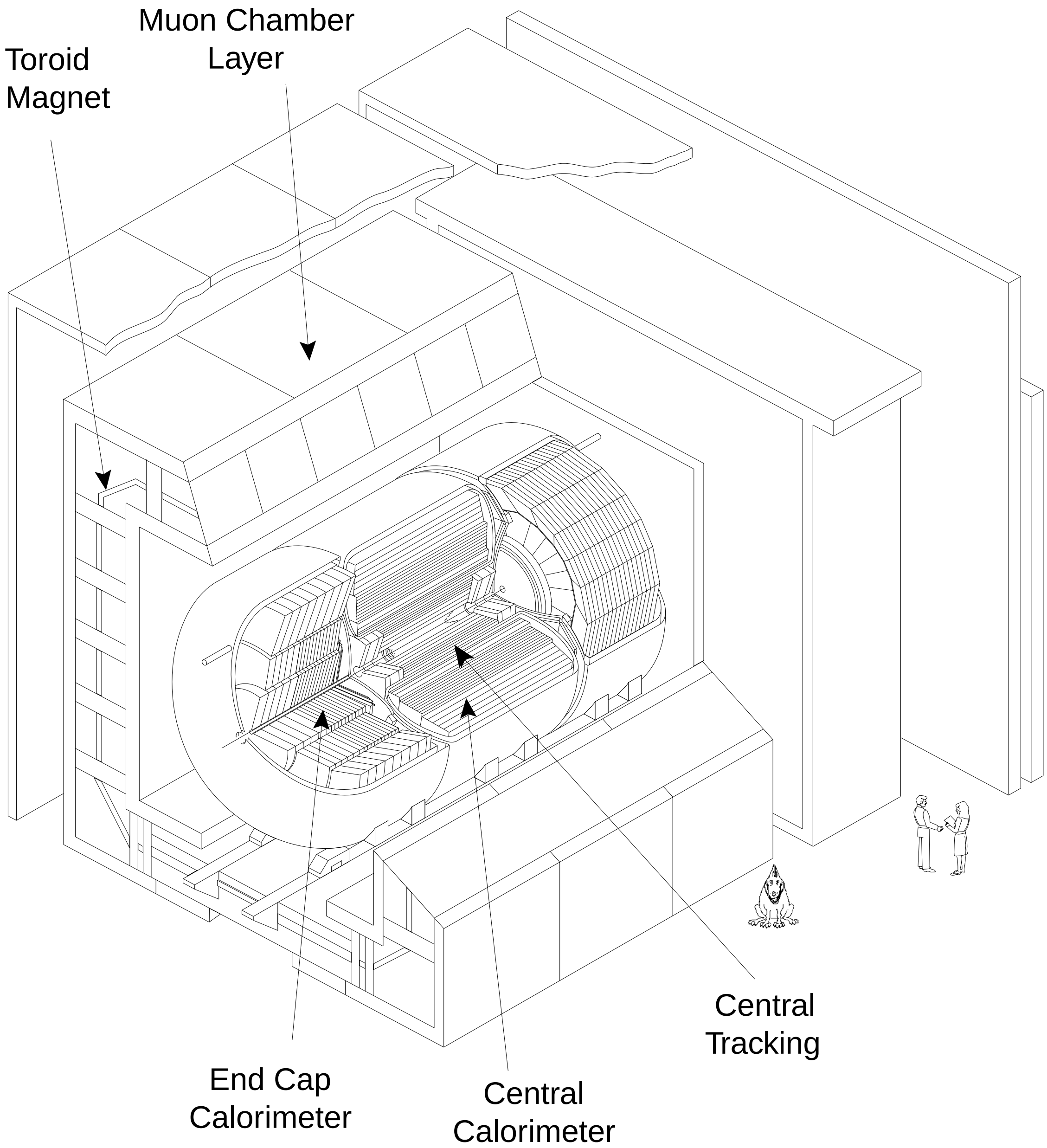

Figure 3.4. A cut-away view of the DØ detector.

Commonly used in place of θ is the pseudorapidity η, defined as

$$\eta = -\ln\left(\tan\left(\theta/2\right)\right). \tag{3.1}$$

The reason to use the (η, ϕ) coordinate is that the pseudorapidity is a convenient variable for $p\bar{p}$ collider physics; for massless particles it is the same as the Lorentz invariant rapidity y, defined by $y = \frac{1}{2}\ln\left(\left(E + p_z\right)/\left(E - p_z\right)\right)$.

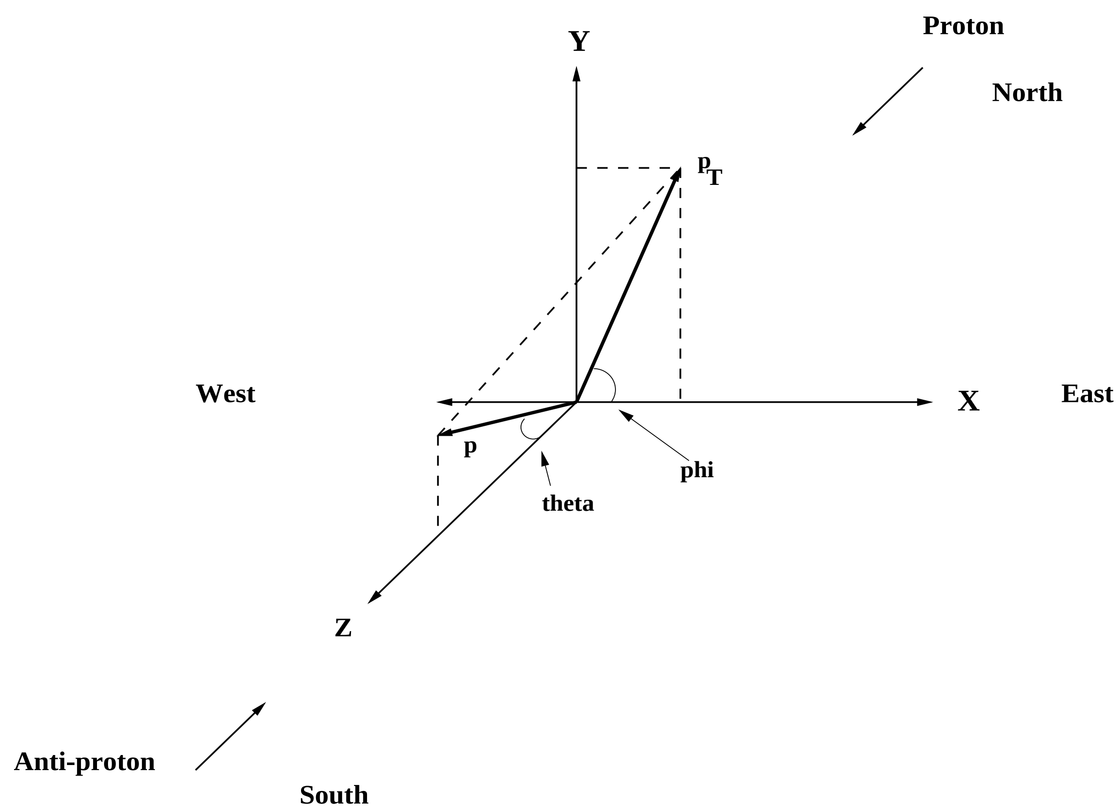

Figure 3.5. The DØ coordinate system.

The pseudorapidity defined in Equation 3.1 is usually called the physics pseudorapidity which is calculated from the actual vertex in an interaction. Since in a $p\bar{p}$ collision at Tevatron, the vertex does not in general appear at the center of the detector, another quantity called the detector pseudorapidity η_d is often used. It is defined with the zero point of the detector, instead of the vertex of the event.

3.2.2 Central Tracking System

The DØ central tracking system measures the trajectories (tracks) of particles coming out of the interaction point. From the tracks, the interaction vertex is determined. And the central tracking system also aids in the identification of leptons in the calorimeter and muon system. The central detector system contains no magnetic field, so no momentum information is available in this stage. This design was chosen to make the chambers compact. The design has been optimized to maximize two-track resolution, to obtain high efficiency, and to obtain good ionization energy measurement to distinguish single electrons from conversion pairs. The central tracking system consists of four detector subsystems; the Vertex Drift Chamber (VTX), the Central Drift Chamber (CDC), the two Forward Drift Chambers (FDC), and the Transition Radiation Detector (TRD). The VTX, CDC and TRD are arranged in concentric cylindrical shells surrounding the beam pipe and covering the central region with an inner radius of 3.7 cm and an outer radius of 78 cm. The FDCs are positioned perpendicular to the beam pipe, one at each end of the central tracking volume. Figure 3.6 shows the side view of the complete central tracking system.

The CDC and FDC detectors are important for the LED analysis for tracking and vertex finding.

3.2.2.1 The Vertex Drift Chamber (VTX)[10, 12]

The VTX drift chamber is the innermost tracking detector at DØ. It is designed to measure the interaction vertex in the z direction accurately. The chamber is filled with a mixture of carbon dioxide (CO_2, 94.5%), ethane (C_2H_6, 5%), and 0.5% of water (H_2O). The gas acts as the ionization medium. And the VTX consists of three

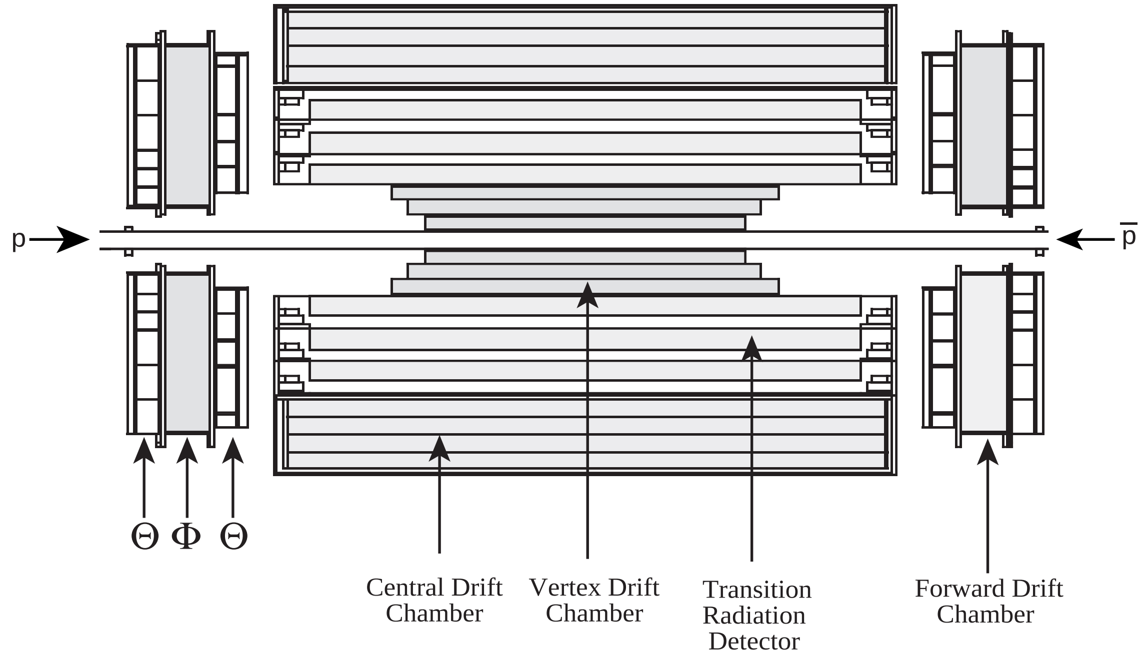

Figure 3.6. Side view of the central tracking system.

layers of sense wires, separated by carbon fiber support tubes. The sense wires are parallel to the beam line and operate at an electric potential of 2.5 kV. Incoming charged particles travelling through the drift chamber strip electrons from the carbon dioxide gas in the chamber. The electrons drift toward a positively charged wire at an almost constant speed. When they approach the wire, they accelerate and strip more electrons which creates an avalanche. With a gain of 40,000, a clear electronic signal is created. With 16 cells of sense wires for the innermost layer and 32 cells for the outer two layers span the length of the detector in the z direction, and has active length of 96.6cm, 106.6 cm, and 116.8 cm which means that particles with $|\eta_d|$ less than 2.0 can pass through if the interaction occurs in the center of the detector. The VTX extends from 3.7 cm to 16.2 cm in radius. Each cell contains 8 wires moving out radially to determine the ϕ coordinate of each hit. Adjacent wires are staggered by 100 μm to resolve left-right ambiguities. Figure 3.7 shows the cell geometry in the $r \times \phi$ plane.

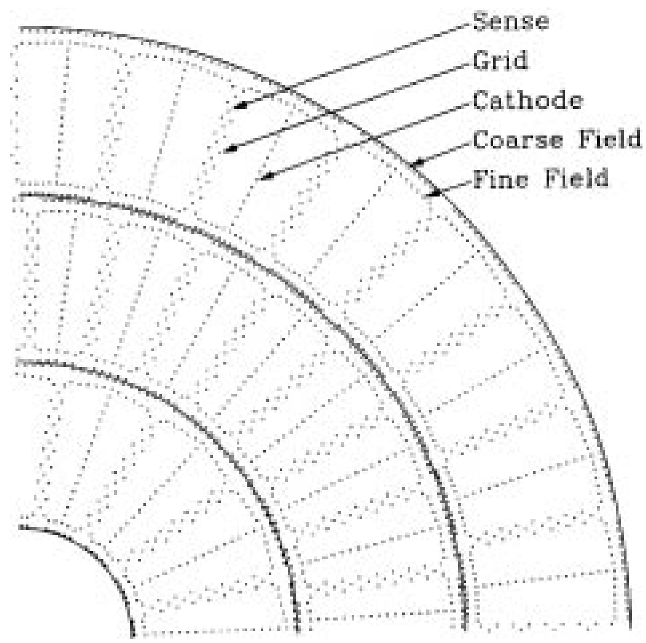

Figure 3.7. A $r \times \phi$ view of one quadrant of the VTX detector.

The distance of a charged particle from a wire is determined by drift time which is the time difference between the $p\overline{p}$ collision and the arrival of electrons at the wire since the drift speed is known. With information from the two neighboring staggered wires, the hit wire and thus it spacial position can be obtained. The spacial resolution of the VTX is about 60 μm in $r \times \phi$ and 1.5 cm in z.

3.2.2.2 The Transition Radiation Detector (TRD)[10, 13]

The TRD is located between the shells of the VTX and the CDC ($17.5 < R < 49$ cm). Particles with $|\eta_d|$ less than 1.4 pass through it. The TRD consists of three layers. Each layer contains a radiator consisting of 393 layers of 18 μm thick polypropylene foils with a mean separation of 150 μm. The gaps are filled with dry nitrogen (N_2). When highly relativistic charged particles ($\gamma \gtrsim 10^3$) traverse boundaries between media with different dielectric constants (foil and gas for the TRD), detectable transition radiation X-rays are created. The intensity of the radiation is proportional to the energy-mass ratio (γ) and is produced on a cone with an opening angle of $1/\gamma$. At the end of each set of foils is a proportional drift wire chamber filled with mixture of xenon (Xe), methane (CH_4), and ethane gas (91% : 7% : 2%). The drift chamber converts the X-rays and measures the resulting charge. Figure 3.8 shows the layout of a TRD layer.

The purpose of the TRD is to identify electrons in a manner independent of the calorimeter. Since the amount of transition radiation emitted in the TRD depends inversely on the particle's mass, the lighter the particle, the more radiation will be produced. As electrons are the lightest charged particles, thus they will emit the most radiation. Hence the measurement of the radiation is used to distinguish electrons from charged hadrons. The TRD is designed to achieve a 10^4 rejection factor against charged pions while remaining 90% efficient for isolated electrons.

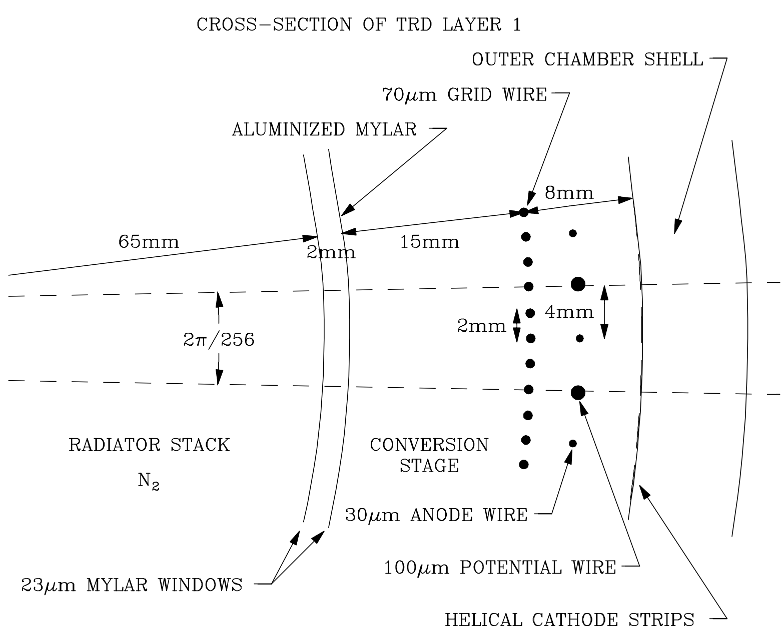

Figure 3.8. A cross section of a TRD layer

3.2.2.3 The Central Drift Chamber (CDC)[10, 14]

The CDC lies between the TRD and the calorimeter. It has a similar radial jet geometry to the VTX. As shown in Figure 3.9, the CDC consists of four concentric layers of cells extending a radius from 49.5 cm to 74.5 cm, and ± 92 cm in the z direction. Particles with $|\eta_d|$ less than 1.0 pass through all four layers of the CDC at this radius. Each layer contains 32 azimuthal cells of 7 sense wires. The cells of neighboring layers are offset by 1/2 cell in order to improve pattern recognition. Each cell includes 7 sense wires staggered by 200 μm to resolve the left-right ambiguities. The cathode is on the boundary of the cell and there are two field-shaping wires between each pair of sense wires. The active medium in the CDC is gas mixture of argon (Ar), methane, carbon dioxide, and water with the ratio of 92.5%, 4%, 3%, and 0.5%. The $r\phi$ position of a hit is determined via the drift time and the wire hit as discussed in the VTX. The z position of a hit is measured using inductive delay lines embedded in the cell walls. When an avalanche occurs nearby, the delay lines will transmit an induced electric pulse. By comparing the pulse arrival times at both ends we can infer the z position of the avalanche. The CDC provides excellent $r\phi$ resolution of about 180 μm, but z resolution is only about 2.9 mm.

The CDC has three purposes: reconstruction of the vertex z position, matching of tracks to energy deposits in the calorimeter, and measurement of the energy loss (dE/dx) of particles traversing the detector. By pointing the CDC tracks back to the beam line and averaging over the tracks (Section 4.2), we determine the z position of the interaction. And matching the tracks to the energy deposits in calorimeter can assist in the identification of photons, electrons and hadronic jets since a photon leaves no tracks (no charge); and electron leaves one track; and a hadronic jet generally leaves more than one rack. The dE/dx measurement also helps in the identification of electrons and hadronic jets, since electron energy loss

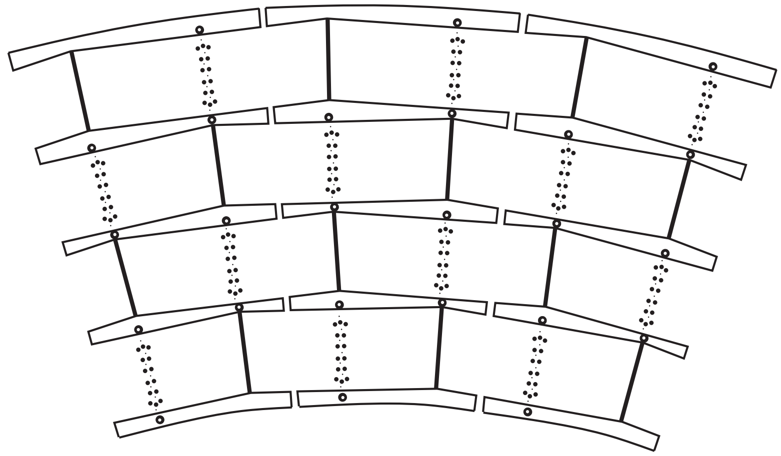

Figure 3.9. End view of part of the CDC.

differs from that of hadrons. The CDC also aids in the identification and momentum measurement of muons seen in the muon detector.

3.2.2.4 The Forward Drift Chamber (FDC)[10, 14]

The FDC extends the outer tracking coverage to $|\eta_d| \lesssim 3.2$. The FDC consists of two identical sets of chambers, oriented with their axes parallel to the beam direction. One is located at each end of the CDC. Figure 3.10 is a diagram of one of the FDCs. Similar to CDC, FDC uses the same gas mixture and similar construction to shape the electric field inside the detector. Each of the FDCs consists of three layers of chambers; one Φ chamber, with radial sense wires to determine the azimuthal coordinate (ϕ) of each hit, sandwiched by two Θ chambers, which measure the polar angle (θ) of each hit. The Φ chamber contains 36 segments each with 16 sense wires and covers the full range of azimuth. Each of the Θ chambers is made of four independent quadrants. Each of the quadrants contains six rectangular cells, with each cell's long axis tangent to circles of increasing radii about the beam axis. Each

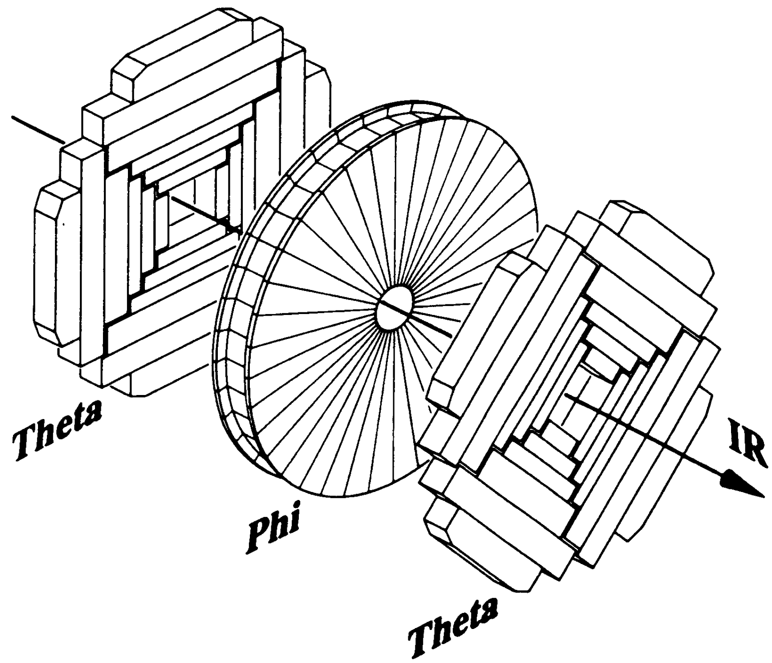

Figure 3.10. Exploded view of one of the two FDC packages.

cell contains eight sense wires and one delay line. The two Θ chambers are rotated in ϕ by $\pi/4$ to obtain optimal position resolution.

3.2.2.5 Central Detector Readout

The electronics for reading out the signals of all central detectors are about the same. There are three stages of signal processing. First, the signals from the chamber wires are preamplified by preamplifiers mounted directly on the chambers themselves. These preamplified signals are fed into analog pulse shaping cards located on the support platform underneath the detector. Finally, the shaped signals are sent to

Flash Analog-To-Digital converters (FADCs) located in the moving counting house, where the signals are sampled and digitized at the rate of 106 MHz (starting with the beam crossing). If the event is not accepted by the Level-1 trigger (see Section 3.2.5), the data is overwritten by the next crossing. Otherwise, the data is compressed by eliminating the flat portions of the signal between the pulses, a process known as *zero suppression*, and sent on to the Level-2 trigger.

3.2.3 The Calorimeter[10, 15, 16, 17]

Because of the absence of a central magnetic field at DØ in Run I, the experiment relies heavily on the calorimeter for energy measurements. The calorimeter also plays an important part in the identification of electrons, photons, hadrons and muons as well as the determination of the transverse energy balance in the event. After traveling through the central detector system, all particles except for muons and neutrinos[1] lose their energy through radiation and collisions in the calorimeter. The calorimeter measures a fraction of this energy (the "sampling fraction"), allowing for an inference of the particle's initial energy.

In construction, the DØ calorimeter is a finely segmented sampling calorimeter. It uses depleted uranium as the absorbing material and liquid argon (LAr) as the active material. Using a heterogeneous combination of active medium and heavy absorber produces a significant stochastic term in the resolution function, but has the advantage of allowing a more compact detector than using a homogeneous (non-sampling) calorimeter. The cost of a sufficiently large homogeneous calorimeter is generally not worth the gain in resolution. The calorimeter is subdivided into zones since electromagnetic particles and hadronic particles lose energy through different

[1]Muons with energy below certain threshold (Section 3.2.4) can be stopped ("range out") in the calorimeter.

mechanisms. A high-energy electron (>>10 MeV) loses its energy primarily through radiating high energy photons when colliding with uranium atoms (bremsstrahlung), while a high-energy photon loses it energy primarily through electron-positron pair production when interacting with uranium. The particles emitted in these processes can themselves undergo bremsstrahlung and pair production, producing secondary electrons, positrons, and photons. This process is called an electromagnetic shower. The rate of energy loss for electrons and photons is described in Equation 3.2

$$\frac{dE}{E} = -\frac{dx}{X_0}, \tag{3.2}$$

where X_0 is called the radiation length, which is the thickness of the collision material required for these particles to lose all but 1/e of their initial energy. For uranium, it is about 3.2 mm. To ensure containment of all photons and electrons, the DØ calorimeter has (at $\eta_d = 0$) a uranium thickness of 65.6 mm (20.5 X_0) in the electromagnetic (EM) region.

Hadrons lose energy primarily through inelastic collisions with uranium nuclei, spraying more hadrons through the uranium. These secondary hadrons can collide with the uranium or (if they are π^0 particles) decay into photon or electron-positron pairs. Hadrons travel greater distances before losing their energy because of the short range of the nuclear interaction. The "nuclear interaction length" (λ) for uranium is 10.5 cm. The DØ calorimeter consists of (at $\eta_d = 0$) 33.6 cm (3.2 λ) of uranium in the "Fine Hadronic" (FH) region, and 46.5 mm (3.2 λ) of copper in the "Coarse Hadronic" (CH) region.

Hadrons interacting with nuclei can produce electrons and photons, so a hadronic shower includes an electromagnetic part. π^0 and η mesons will also be absorbed electromagnetically since they quickly decay to two photons. And in a hadron cascade roughly 30% of the incident hadron energy is lost by the breakup of nuclei, nuclear excitation, and evaporation neutrons and protons, and does not give an observable signal. So without compensation, The calorimeter response to electrons is thus greater than that compared to hadrons with the same energy; $e/h > 1$. This difference in response has disastrous effects on a hadron calorimeter's performance: the resolution will not improve, the signal shape for monoenergetic hadrons will be nongaussian (and thus asymmetric), and the hadronic response will not be linear with the incident energy. Using uranium as the cascade medium, the "invisible" energy losses from nuclear breakup can be compensated by the extra energy released by fast neutron and photon fission of uranium. The DØ calorimeter achieved e/π ratio (the ratio of the calorimeter responses to electrons and pions) close to 1, so it is nearly compensating.

3.2.3.1 Overview

The calorimeter is housed in three cryostats, one for the Central Calorimeter (CC) covering the region $|\eta| < 1.2$, and two for Endcap Calorimeters (EC north and EC south) extending the coverage to $|\eta| \approx 4$. In the space between the calorimeters is deployed a set of scintillating tiles and associated phototubes called the Inter-cryostat Detector (ICD). Each of the calorimeters is divided into electromagnetic and hadronic layers; the electromagnetic layers are optimized for the identification and measurement of electrons and photons and the hadronic layers are optimized to contain and measure jets. Figure 3.4 shows the layout of the calorimeter in the DØ detector.

The calorimeter is constructed from separate modules consisting of readout cells. The basic calorimeter cell has three components as shown in Figure 3.11: A grounded uranium plate, with which incoming particles collide; a liquid argon gap, which the

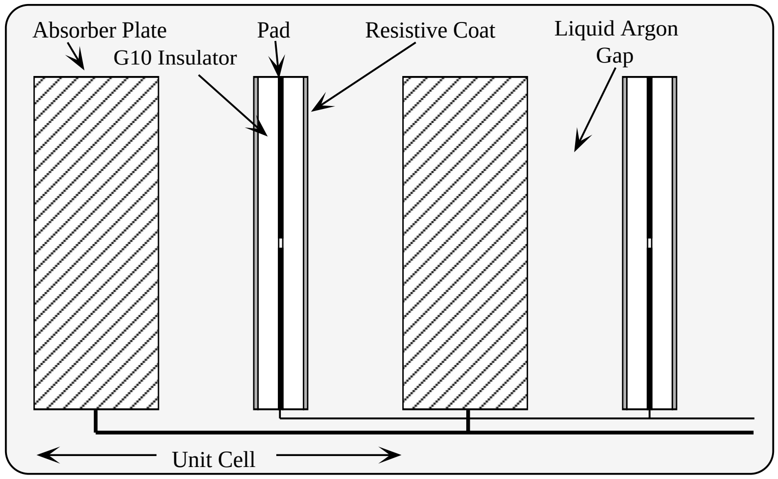

Figure 3.11. Schematic view of a DØ calorimeter cell.

showering charged particles ionize; and a signal readout board is 2.3 mm thick. The signal boards for most of the calorimeter consist of two laminated sheets of 0.5 mm thick G10. The outer surface of each sheet are coated with a high resistivity epoxy and are held at high voltage (approximately 2.5 kV) to act as the "anode". One inner surface is left bare while the other retains its original copper cladding but milled into the desired readout pad shape and size. The pad shapes are typically square and sized to match the transverse dimensions of electromagnetic and hadronic showers. Signals from several pads at the same η and ϕ are ganged in depth to form a readout layer.

There are $\sim$ 47,000 readout channels in the DØ calorimeter. The cell signals, which consist of pulses with widths of 450 ns, are read out in three steps. First, the signals are carried through four ports in the cryostats to charge sensitive preamplifiers mounted on top of the cryostats. Output signals from the preamplifiers are transported to the baseline subtractor (BLS) modules located in the platform underneath the detector. The BLS modules perform analog signal shaping, then split the signal into two. The first is used as input to the calorimeter Level-1 trigger after

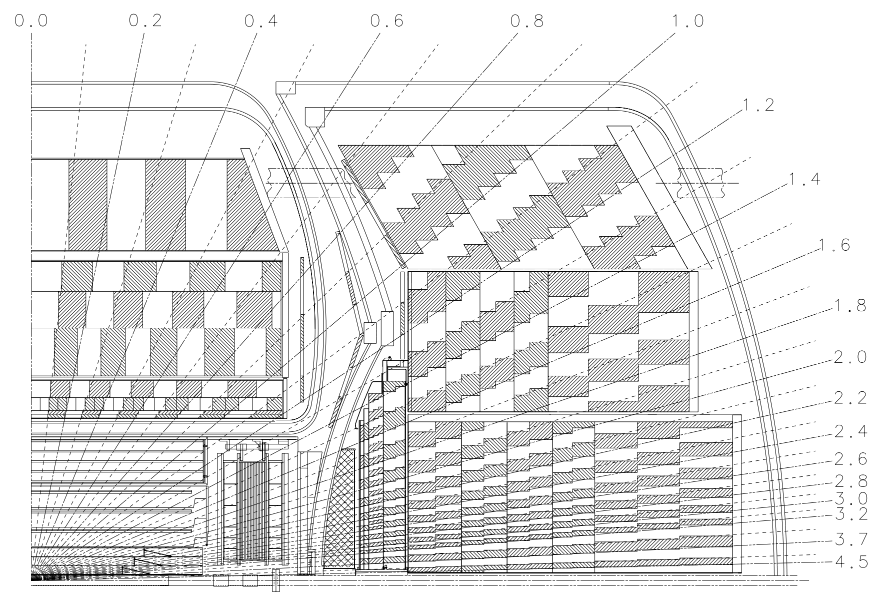

Figure 3.12. A side view of one quarter of the DØ calorimeters and the central tracking detectors.

summing the signals into 0.2×0.2 trigger towers and large tiles (see calorimeter trigger in Section 3.2.5). The second signal is used for data readout: it is sampled just before the beam crossing and 2.2 μs later. The difference between the two samples is a dc voltage proportional to the collected charge. Finally, if the event is accepted by the Level-1 trigger, this difference is sent to ADCs which digitize, then zero-suppress the signal before sending it on to the Level-2 trigger.

The structure of the readout layers is shown in Figure 3.12, the calorimeter modules form pseudoprojective towers with their centers following lines of constant pseudorapidity, while the module boundaries are aligned perpendicular to the absorber plates. The transverse segmentation of the calorimeter is shown in Figure 3.13. A map of the detector indicating the placement of different calorimeter sections is displayed in Figure 3.14. An brief description of each section will be given below.

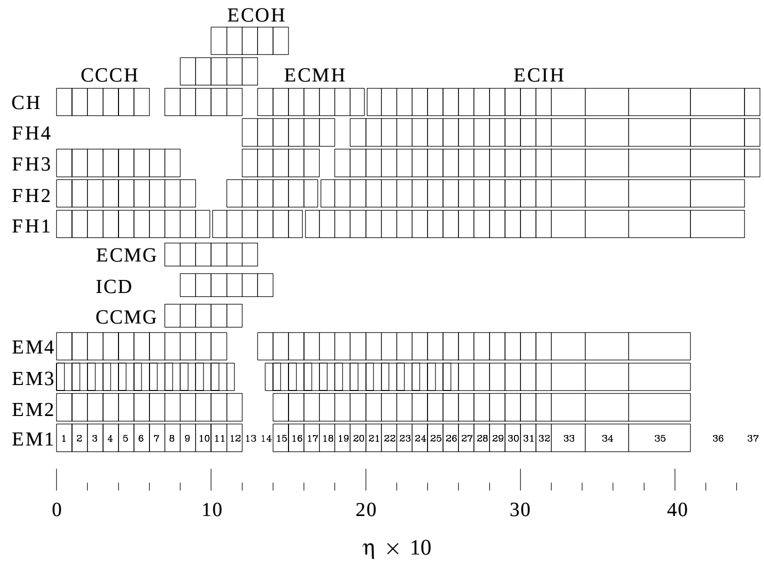

Figure 3.13. Segmentation of the DØ calorimeter towers.

3.2.3.2 Central Calorimeter (CC)

The Central Calorimeter is composed of three cylindrical concentric shells 226 cm in length. It has a radial coverage of $75 < r < 222$ cm from the beam pipe and an angular coverage of $35° < \theta < 145°$, or $|\eta| < 1.2$. The inner shell consists of 32 electromagnetic modules, thick enough to contain most electromagnetic showers. The middle shell, made of 16 fine hadronic modules, measures showers of hadronic particles, while the outer layer, made of 16 coarse hadronic modules, measures any leakage out of the FH layer while minimizing *punchthrough*, the energy flow out of the calorimeter and into the muon system. The EM modules consist of 21 radial cells, arranged in four readout layers (EM1 through EM4). Each cell is composed of a 3 mm depleted uranium absorber plate and a 2.3 mm LAr gap for a sampling

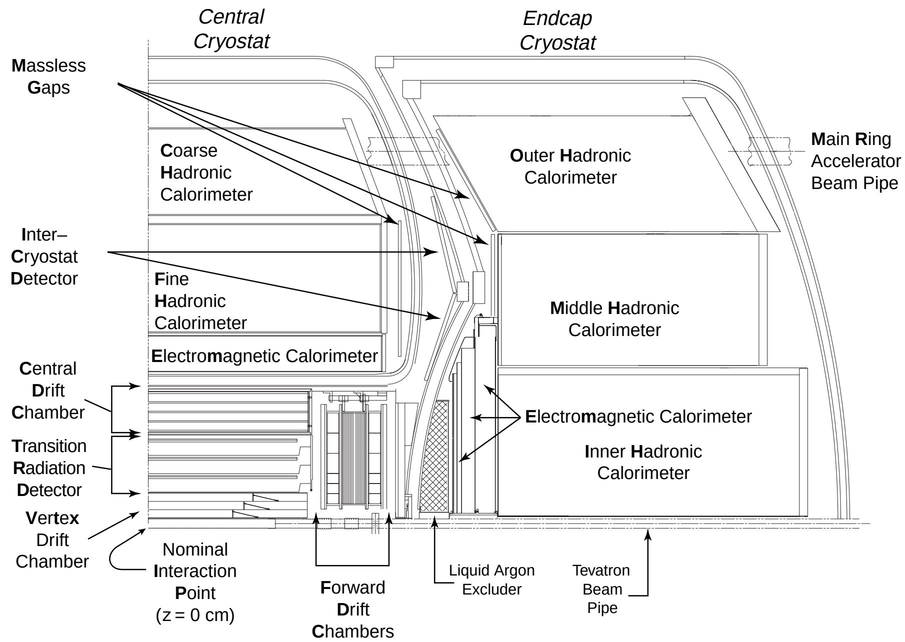

Figure 3.14. Map of the calorimeter and central detector. A one quarter view showing half of the CC and one EC cryostat is displayed. All of the parts displayed except for the MR accelerator beam pipe are symmetric in azimuthal angle, φ, about the Tevatron beam pipe.

fraction of 12.9%. The FH modules consist of 50 radial cells, arranged in three readout layers (FH1 through FH3), with each cell made from a 6 mm uranium-niobium alloy (U-Nb) absorber plate and a 2.3 mm LAr gap for a sampling fraction of 6.9%. Finally, the CH modules consist of 9 radial cells, but only one readout layer. The CH cells use 4.75 cm copper absorber plates with a 2.3 mm LAr gap for a sampling fraction of 1.7%.

The transverse segmentation of the calorimeter is 0.1×0.1 in $\eta \times \phi$ space, except in the third EM layer (EM3) (see Figure 3.13). This layer, corresponding to the EM shower maximum, has its segmentation increased to 0.05×0.05 in $\eta \times \phi$ space in order to fully optimize the distinguishability between electron and hadronic showers. In addition, each concentric shell (EM, FH and CH) is rotated azimuthally to avoid any continuous cracks.

3.2.3.3 Endcap Calorimeters (EC)

The two Endcap Calorimeters provide coverage on either side of the CC from a pseudorapidity of $1.3 \leq |\eta| \lesssim 4$. This corresponds to an angular coverage of $2^\circ < \theta < 30^\circ$, and $150^\circ < \theta < 178^\circ$. Each EC cryostat is divided into four sections: the electromagnetic, the inner hadronic (IH), the middle hadronic (MH), and the outer hadronic (OH). The EM modules in the EC (ECEM) are disk shaped and occupy the center of the EC cryostat. The radial coverage starts at 5.7 cm and extends to an outer radius varying between 84 cm to 104 cm, corresponding to an angular coverage of $3^\circ < \theta < 27^\circ$. The modules consist of 18 radial cells with absorber plates made from 4 mm thick depleted uranium. The cells are arranged into four readout layers (EM1 through EM4). The transverse segmentation is mostly 0.1×0.1 in $\eta \times \phi$ space; however, for $|\eta| > 3.2$, the pad size becomes too small so the segmentation is coarsened to 0.2×0.2. As in the CC, the third ECEM layer has finer segmentation to improve electron/hadron shower resolution. The segmentation is $\Delta\eta \times \Delta\phi = 0.05 \times 0.05$ for $|\eta| < 2.7$, 0.1×0.1 for $2.7 < |\eta| < 3.2$, and 0.2×0.2 for $|\eta| > 3.2$ (see Figure 3.13).

The IH module, located directly behind the ECEM, is cylindrically shaped with inner and outer radii 3.92 cm and 86.4 cm respectively. Longitudinally, the IH is divided into fine hadronic (IFH) and coarse hadronic (ICH) sections. The IFH consists of 16 cells – each made from 6 mm thick semicircular uranium absorber plates – that are arranged in four readout layers (FH1 through FH4). In order to avoid cracks, each alternate plate is rotated by 90° in ϕ. The ICH consists of a single readout layer made from 13 cells, each using 46.5 mm stainless steel absorber plates. The IH transverse segmentation matches that of the ECEM: $\Delta\eta \times \Delta\phi = 0.1 \times 0.1$ for $|\eta| < 3.2$, and 0.2×0.2 otherwise; however, for $|\eta| > 3.8$ (beyond the ECEM coverage), it is 0.4×0.2 (see Figure 3.13).

Surrounding the inner core of EM and IH modules in the EC is the MH ring. This ring, consisting of 16 wedge shaped modules, extends from an inner radius of 33 cm to an outer radius of 152 cm. Like the IH, each MH module is divided longitudinally into fine hadronic (MFH) and coarse hadronic (MCH) sections. The MFH consists of 60 radial cells arranged in four readout layers (FH1 through FH4). Each cell uses 6 mm U-Nb alloy absorber plates. The MCH is a single readout layer consisting of 14 cells. Each cell uses 46.5 mm stainless steel absorber plates. The transverse segmentation of the MH is exactly like the IH.

The OH ring surrounds the MH ring at an inner radius of 162 cm and an outer radius of 226 cm. Each of the 16 OH modules are coarse, and form a parallelogram with an inner face at an angle of $27.4°$ with respect to the xy plane. An OH module consists of 25 radial cells, read out in three layers. Each cell uses 46.5 mm stainless steel absorber plates.

3.2.3.4 Intercryostat Detectors (ICD) and Massless Gaps (MG)

In the intercryostat region (ICR) between CC and EC (see Figure 3.14), there are gaps in coverage in the form of uninstrumented material due to support structures for calorimeter modules and cryostat walls. To partially compensate for the energy loss in this material, two different types of detectors are used. First, an additional layer of liquid argon sampling is included on the face of each MH and OH module of the EC and on each end of the FH modules in the CC. These *massless gaps* (MG) have no significant absorber material but do sample the shower energy before and after the dead material between the cryostats. The η coverage for the MG is $0.7 < |\eta| < 1.2$, with a typical segmentation of 0.1×0.1 in $\eta \times \phi$ space. The second, called the Intercryostat Detector (ICD), consists of two arrays of 384 scintillation counter tiles mounted on the front surface of each EC cryostat. The tiles match the LAr calorimeter cells in size. The locations of ICD and MG are shown in Figure 3.14.

3.2.3.5 Calorimeter Performance

The calorimeter energy resolutions of electrons and pions can be determined from test beam data. They are:

$$\frac{\sigma(E)}{E}|_e = \frac{15\%}{\sqrt{E(GeV)}} \oplus 0.3\%, \tag{3.3}$$

$$\frac{\sigma(E)}{E}|_{\pi^{\pm}} = \frac{40\%}{\sqrt{E(GeV)}}, \tag{3.4}$$

where symbol $\oplus$ means addition in quadrature.

The energy resolution for hadronic jets is determined by studies done by a dijet balance method. The result is:

$$\frac{\sigma(E)}{E}|_{jet} = \frac{80\%}{\sqrt{E(GeV)}}. \tag{3.5}$$

3.2.4 The Muon System[10, 18]

Since muons are minimum ionizing particles (MIP), they do not lose significant energy in the calorimeter. Muons with energy greater than some threshold ($\approx$ 3.5 GeV at $|\eta|= 0$; 5GeV at larger $|\eta|$) will make it all the way through the calorimeter. Thus the detection and momentum measurement of muons are achieved by the outermost part of the DØ detector, the muon system. The DØ muon detector consists of three superlayers of proportional drift tubes (PDTs), to detect the passage of charged

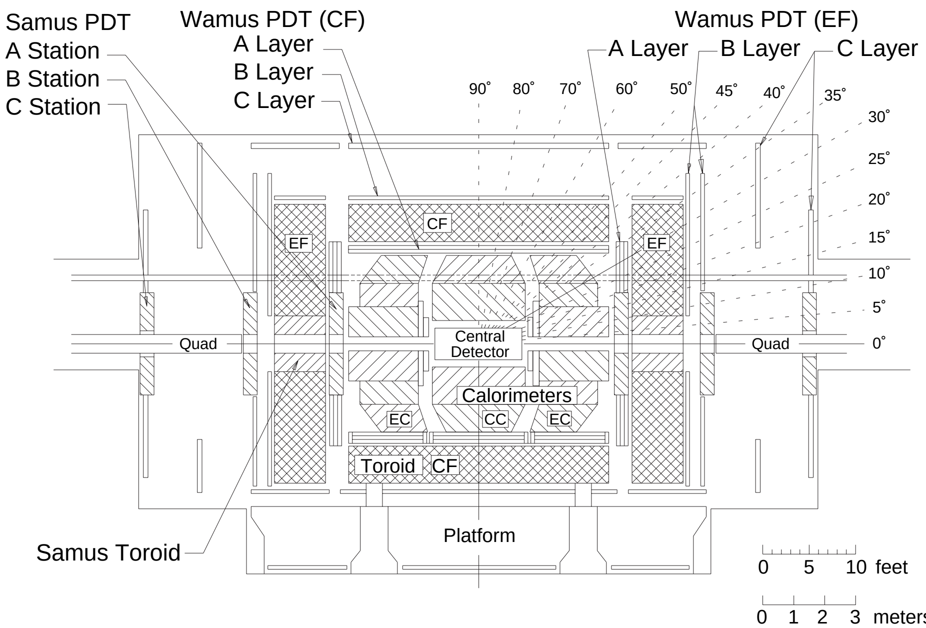

Figure 3.15. Side view of the DØ muon system.

particles, and five iron toroid magnets with a field strength of ~ 2 Tesla, to allow measurement of the momentum of particles traversing the detector. Figure 3.15 is a cross section view of the entire DØ detector, showing the location of each of the toroids, the superlayers, and the calorimeters and central detector within. In this analysis, the muon system is used to identify and reject events containing one or more muons from the interaction region. Therefore momentum resolution is less important than coverage of as much solid angle as possible. Also important is the extreme thickness of the calorimeter and the muon toroids which makes the likelihood of hadronic punchthrough very small, thus allowing measurement of muons within jets. The muon system coverage extends down to approximately 3 degrees from the beam pipe, and the thickness of the detector (before the outer layer of PDTs) is typically more than 12 nuclear interaction lengths. The thickness profile of the DØ detector is shown in Figure 3.16.

One central Fe toroid (CF) covers the range of pseudorapidity $|\eta| < 1.0$; the two

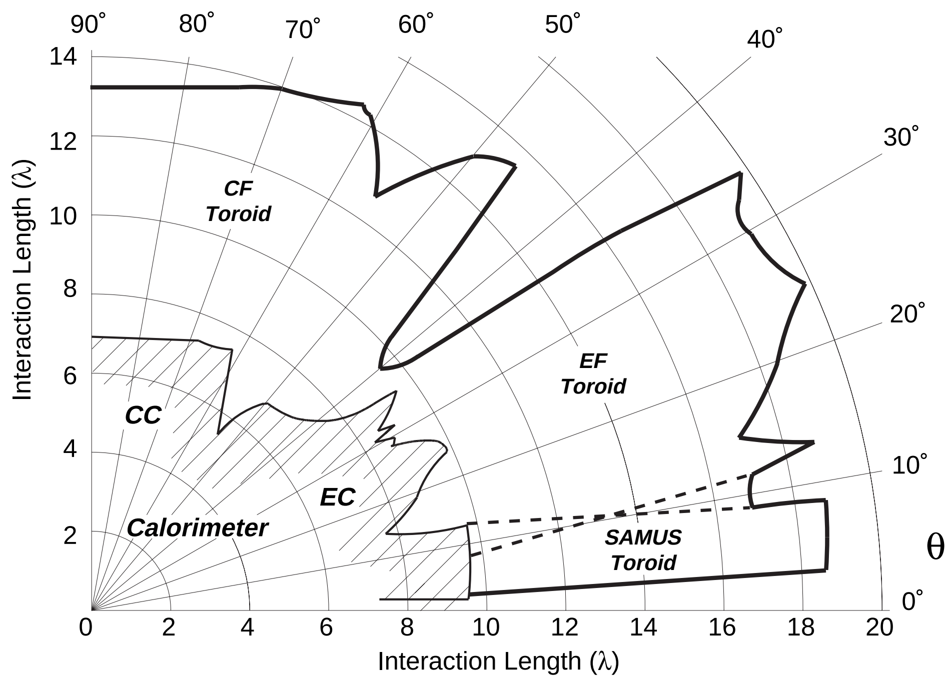

Figure 3.16. Thickness of the calorimeters and muon toroids in units of nuclear interaction length vs. polar angle.

end Fe toroids (EF) extend this coverage to $|\eta| < 2.5$. Together these two regions form the Wide Angle Muon System (WAMUS). The WAMUS PDTs are distributed into three superlayers. Inside the toroids is the A layer, which contains four planes of PDTs. Outside the magnet are the B and C layers, each containing three planes of PDTs. The B and C layers are separated by about one meter, to provide a lever arm for momentum measurement. Adjacent planes of PDTs within each layer are offset to help eliminate the left-right ambiguity associated with hit finding in drift tubes.

The PDTs are oriented such that the bend direction of the magnets matches the direction of greatest accuracy of position measurement. The non-bend coordinate, along the length of the wire, has less accuracy; the hit location along the length of the wires is determined by a combination of timing and pad signals. Layer A can determine the incident direction of a muon to 0.6 $m$rad and its position to 100 μm;

layer B and C can determine the direction and position of an outgoing muon to 0.2 $m$rad and 170 μm, respectively. This accuracy results in a resolution of the muon momentum p (in GeV) parameterized by:

$$\sigma(1/p) = 0.18(p - 2.0)/p^2 \oplus 0.003, \tag{3.6}$$

for muons with momentum $p > 4.0$ GeV/c.

The two Small Angle Muon System (SAMUS) toroids occupy the center of the EF toroids. They extend the coverage for detection of muons to $|\eta| = 3.6$. The design and functioning of the SAMUS is similar to that of the WAMUS although the high hit occupancy of the forward regions forces the use of smaller drift tubes than in the central region.

3.2.5 Triggering and Data Acquisition(DAQ)[10]

The Tevatron, during Run I, operated with a 3.5 μs interval between bunch crossings, which amounts to a rate of about 286 kHz ($\approx 1/3.5$ μs). It is neither practical, nor of interest, to record information of each beam crossing. Most of the physics processes of interest have a very small cross section compared to the total (elastic and inelastic) $p\bar{p}$ cross section[2]. The solution is to *trigger* on events of interest.

A schematic overview of the DØ trigger system is shown in Figure 3.17. It consists of three different levels, each with increasingly sophisticated event characterization. The Level-Ø trigger, using a set of scintillator counters, indicates the presence of an inelastic collision: it distinguishes between beam-beam ($p\bar{p}$) and beam–gas or beam–halo collisions. It reduces the 286 kHz rate down to about 150–200 kHz. The Level-1 trigger is hardware based: hardware elements issue decisions based on fast

[2] At $\sqrt{S} = 1.8$ TeV, the total $p\overline{p} \to X$ cross section is 70 mb.

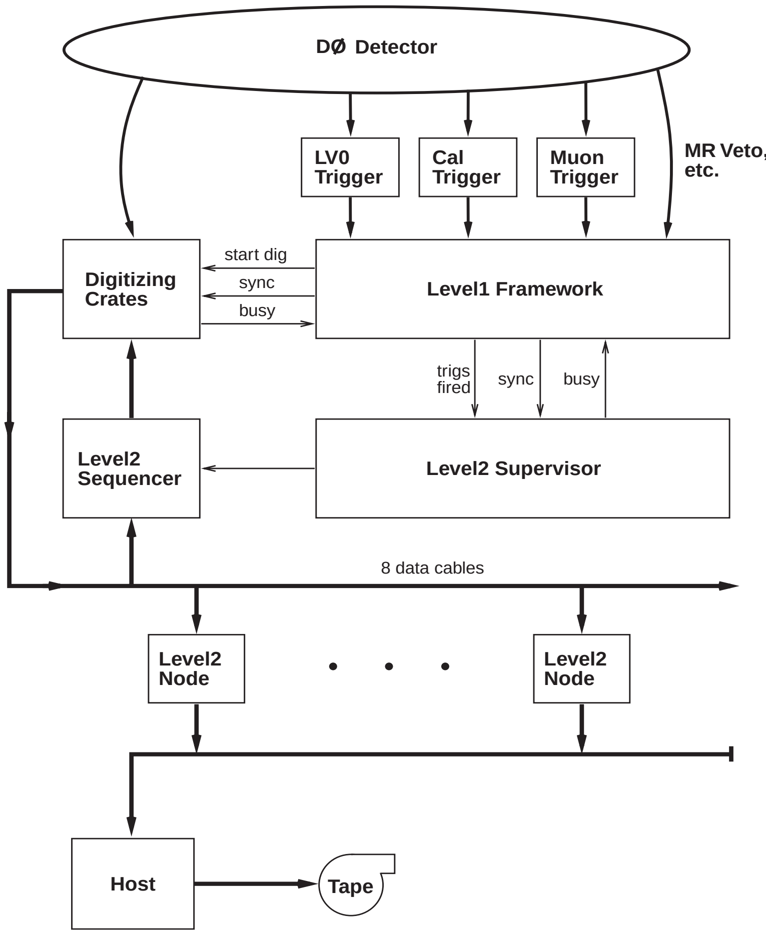

Figure 3.17. DØ trigger and data acquisition system.

detector pick-offs (see overview in Section 3.2.3). Most trigger decisions incur no dead-time penalty: they are made within the 3.5 μs interval between beam crossings. However, some triggers, called Level-1.5, may require additional time. The event rate out of Level-1 is roughly 800 Hz (Level-1.5 200 Hz). Events that pass the Level-1 trigger are fully digitized, and the data is sent to a farm of 48 microprocessors, which make up the Level-2 trigger. The Level-2 trigger is software based, and relies on the reconstruction of the events with a simplified and fast version of the reconstruction program. If an event passes the Level-2 trigger, it is passed along to the host system, where it is written to magnetic tape. The rate out of Level-2 is approximately 2 Hz, a rate limited by the speed of the magnetic recording medium.

3.2.5.1 Level-Ø[10, 19]

The Level-Ø system performs several functions:

- Detection of inelastic $p\bar{p}$ collisions;
- Instantaneous luminosity monitoring;
- Identification of multiple interactions within one beam crossing;
- Determination of the z-coordinate of the interaction vertex.

The Level-Ø system consists of two arrays of hodoscopes mounted between the FDC and EC. Each hodoscope consists of rectangular scintillation counters which provide partial coverage of the rapidity range $1.9 < |\eta| < 4.3$, and nearly full coverage in the range $2.3 < |\eta| < 3.9$. The spectator quarks in an inelastic $p\bar{p}$ collision will hadronize in the far forward region. The Level-Ø trigger exploits this by looking for a coincidence between signals from the hodoscopes at each end of the detector. The Level-Ø system is ≥ 90 % efficient for detecting non-diffractive inelastic collisions.[20]

In addition, the arrival times of the signals from the two hodoscopes is used in determining the z-coordinate of the collision vertex. Due to the large spread of the vertex distribution ($\sigma = 30$ cm), knowledge of z position of the vertex improves all E_T and $\not\!\!E_T$ calculations at Level-1 and Level-2. A fast z-coordinate (fast z) determination, with a resolution of ± 15 cm is available 800 ns after the collision, and is used by Level-1. At 2.1 μs after the collision, a more accurate determination is made with a resolution of ± 3.5 cm (slow z), and this is provided to the Level-2 trigger. The time distribution of the counter hits is also used to determine if an event contained multiple interactions: a flag is set and made available to the trigger system.

The rate of the Level-Ø system is also used to determine the luminosity delivered to the DØ detector. At low luminosities, there are very few multiple interactions, hence, the coincidence rate is almost exactly proportional to the instantaneous luminosity. At higher luminosities, the rate of multiple interactions increases, and the coincidence rate starts to saturate[3]. A correction is introduced in order to properly calculate the luminosity.[20]

3.2.5.2 Level-1[10, 21, 22]

The Level-1 trigger is a hardware trigger which bases its decision on fast and coarse information from the calorimeter, the muon system, the Level-Ø hodoscopes, and the accelerator timing signals(see Section 3.2.3), and makes most of its decisions within the 3.5 μs interval between beam crossings. The Level-1 trigger framework is a flexible and programmable hardware processor which is responsible for combining the decisions of the individual Level-1 components, for coordinating various vetoes which can inhibit triggers, for providing a large number of scalers which allow for accounting of trigger rates and dead-times, and for managing the readout of the digitization crates before handing the event to the Level-2 trigger. The trigger vetoes are related to any Main Ring activity (recall that the Main Ring passes through the calorimeter), as well as to any required prescales[4] to reduce the output rate.

The Level-1 trigger framework consists of a network of 256 AND–OR terms(called latch bits). Each of these bits contains specific requirements, such as the presence of an trigger tower with $E_T > 5$ GeV. The 256 input AND–OR trigger terms are

[3] Saturation occurs when a crossing with multiple interactions is recorded as a single coincidence.

[4] Setting the prescale to some integer value N causes the trigger to pass the event once in every N times that its trigger is satisfied.

reduced to 32 output terms, corresponding to 32 specific Level-1 triggers. Each Level-1 trigger is a logical combination of the 256 input term, whether that term is required to be asserted, negated, or ignored. Each trigger has also a programmable prescale that can be used to control the input rate to the Level-2 trigger.

3.2.5.3 Main Ring Veto[24]

During normal Tevatron operations, the Main Ring is continually used for antiproton production: this minimizes the down-time between stores, thus maximizing the total delivered luminosity to the detectors. Since the Main Ring passes through the DØ detector, losses in the Main Ring will show up in the detector, thus creating a high noise level (especially in the calorimeter and muon system). Therefore, events are not accepted during these noisy periods by enabling veto signals in the framework.

The largest Main Ring losses occur during injection and transition. Injection occurs every 2.4 s with transition occurring 300 ms later. To deal with this situation, a `MRBS_LOSS` veto trigger is implemented, which rejects any events within a 400 ms window following injection. The dead-time is about $0.4/2.4 \approx 17\%$. Another period of heavy Main Ring losses occurs when Main Ring bunches pass through the detector. A veto trigger, called `MICRO_BLANK`, is utilized to reject events when Main Ring bunches occur within a 1.6 μs window of the Tevatron beam crossing[5]. This incurs an additional dead-time of about 8%. All muon, all jets + $\not\!\!E_T$, nearly all jet and some electron triggers are inhibited if either `MRBS_LOSS` or `MICRO_BLANK` terms are set.

Since electrons are well defined objects and are measured in regions of the detector far from the Main Ring pass through, an active vetoing system was developed

[5]This situation occurs every 21 μs.

in order to keep the deadtime and lost luminosity down to a minimum. Instead of using timing signals from the accelerator, scintillator counters were mounted near the Main Ring beam pipe to measure the losses directly. Only when the rate in the counters exceeds a threshold are the so called `MAX_LIVE` triggers inhibited. Certain triggers are also inhibited for an additional 100 μs after the counter rate drops below threshold to allow the calorimeter signals to return to base line levels. The advantage of the active veto scheme is that the trigger deadtime is directly linked to the losses in the Main Ring. If the Main Ring is running cleanly, then the live time can be increased dramatically for those triggers. Since $\not\!\!E_T$ is very sensitive to any spurious energy in the detector, the active veto is not used in the triggers that include $\not\!\!E_T$ requirement.

3.2.5.4 Calorimeter Trigger[22, 23]

The calorimeter Level-1 trigger operates on the fast pick-off signals provided by the calorimeter's BLS cards (see Section 3.2.3), which sum cells into 1280 trigger towers of size 0.2×0.2 in $\eta \times \phi$ space out to $|\eta| = 4.0$. Very large E_T jet triggers use the signals summed over entire calorimeter quadrants of size 0.8×1.6 in $\eta \times \phi$ space (*large tiles).* Separate inputs are provided for the EM and the FH modules[6]. Each energy measurement is analog-weighted by the sine of the polar angle of the trigger tower in order to obtain the transverse energy, and then it is digitized by an 8-bit FADC. The corrected transverse energy is then computed by using the Level-Ø "fast z" measurement of the interaction vertex.

In addition, all trigger towers are summed to produce seven global variables: the global corrected EM transverse energy (E_T), hadronic E_T, and total E_T, and the

[6]The CH modules as well as ICD and Massless Gaps are not used at Level-1.

global uncorrected EM transverse energy (E_T), hadronic E_T, and total E_T, as well as $\not{E}_T$. Level-1 $\not{E}_T$ is calculated using signals from the trigger towers with $|\eta| < 2.6$ and does not include information from the ICD detector, the Massless Gaps and the CH Calorimeter. The Level-1 global quantities can be compared with up to 32 programmable thresholds. Each of these comparisons yields a trigger term which is input to the trigger framework. This makes it possible to specify triggers such as 'missing E_T above 40 GeV', or 'total corrected E_T above 100 GeV'.

Certain electron triggers (e.g. one might require at least one electromagnetic tower with $E_T > 7$ GeV) will ask for a Level 1.5 confirmation if their requirements are met. The calorimeter Level 1.5 system consists of 12 digital signal processors (DSPs) that examine the 1280 towers to apply an isolation requirement. While the Level 1 calorimeter trigger can only count towers exceeding thresholds, Level 1.5 is able to compare energies in towers near a high energy EM tower. If an EM tower is isolated, that is there is little energy in towers nearby, then Level 1.5 is passed and the specific Level 1 trigger passes as well. The calorimeter Level 1.5 DSPs may take up to 250 μs to reach a decision, thus introducing some experimental deadtime since all Level-1 activity is stalled. But it provides a rejection factor of 5 with greater than 95 % efficiency for electron confirmation which is a reasonable trade-off between event quality and experimental livetime.

3.2.5.5 Muon Trigger[25]

The muon Level-1 hardware trigger receives a bit from each muon chamber tube indicating whether or not it was hit, for a total of about 16,700 bits. By looking for patterns of hit tubes in different regions of the detector, the muon trigger can count tracks (contiguous muon hits leading back to the interaction vertex) representing possible muons. The Level 1 muon system only looks quickly for patterns and cannot measure muon p_T. Some specific muon triggers require a Level 1.5 confirmation where the hit patterns are examined more closely with specialized hardware for a rough p_T determination so that p_T requirements can be made. Depending on the number of hits in the muon system, the decision made by Level 1.5 can take up to 5 μs for WAMUS regions and can exceed 100 μs for SAMUS.

3.2.5.6 Level-2[10]

The Level-2 system functions as the DØ data acquisition system and the Level-2 software trigger. The fully digitized data is sent to a farm of 48 Microvax 4000/60 computers operating in parallel which make up the Level-2 filter system. Level-2 reconstructs and identifies specific objects such as jet, electron, photon, muon candidates, or event characteristics such as $\not\!\!E_T$ and scalar E_T. Many different (up to 128 at one time) software filters can run in the Level-2 nodes, each connected to one of the Level-1 triggers. The filters usually select events passing requirements on the E_T, p_T, η, and ϕ as well as the number of objects of a specific type. A given event goes to a single Level-2 node where all the appropriate filters, as defined by the current trigger menu and the Level-2 trigger that passed the event, are run. If any of the filters pass the event, it is sent to the DØ host computer where it is written to tape. The data are stored in a format based on Zebra[26], an extension of FORTRAN that allows dynamic memory allocation.

CHAPTER 4

EVENT RECONSTRUCTION AND OBJECT IDENTIFICATION

Level-2 does not utilize detailed information from the full tracking system or shower shape. So the raw data in the form of digital signals: pulse heights, widths and times, needs to be converted into physics objects. This task is performed by the DØ Reconstruction Program (`RECO`). `DØRECO` starts by processing the raw data into high-level objects, such as energy clusters in the calorimeters or tracks in the tracking and muon systems. These objects are in turn combined to form the physical particles that originated in the $p\bar{p}$ collisions: electrons, photons, jets, muons, and weakly interacting neutral particles ($\not\!\!E_T$). These particles and their measured kinematic properties form the basis of all analyses; therefore, it is essential to fully understand the reconstruction process. The output of `DØRECO` is saved in two different formats: the Standard output (STA) and the Data Summary Tapes (DST). The STA files store both the HITS (event hit information from the detectors) and the processed information. The RAW data banks are dropped from STAs while other online information such as filter information appended at Level-2 are kept. The DSTs are compressed version of the STAs containing only the processed information including the reconstructed z-vertex information for primary vertices, track information from central detector, information from TRD and muon chambers, calorimeter clusters, information on loosely-defined electron, photon, muon, and jet candidates, and $\not\!\!E_T$ information[27]. There is also a compressed DST format: the Micro DST (μDST)[28]. The μDST files contain a subset of the information on the DSTs.

This chapter mainly describes the identification and reconstruction algorithms used in this analysis. For further details, see reference [27].

4.1 Track Finding

One of the first steps in `RECO` is to process the FADC output from the tracking chambers. The central detector and muon FADC signals are analyzed, and the points where particles ionized the gas in the drift cells are located. A pattern recognition algorithm searches for contiguous lines of these *hits* to build *tracks*. A track reconstructs the path of a particle within the tracking volume and indicates the direction the particle took through the detector. The amount of ionization can also be determined from the raw data to calculate the dE/dx for each track.

4.1.1 Central Detector

Raw ADC information in the central detector is used first in the $r\phi$ view and then in the rz view. The algorithm of track finding using CDC is:

1. The outermost hits in each of the four cylindrical layers are paired with innermost hits in that layer within a segment of ϕ. Hits between each pair are added to form a track segment if they lie on the line defined by the pair.

2. The track segments are combined into tracks traversing all four layers of the CDC by beginning with the track segment in the outermost layer, adding the best-fitting segment in the next-outermost layer, and so on until the best-fitting segment in the innermost layer have been added. Up to one layer may be skipped if collinear segments are found in the remaining three layers.

3. After fitting tracks in the $r\phi$ view in this manner, delay line measurements are used to determine the rz positions of the tracks.

Tracks obtained in this way have a resolution of about 2.5 $m$rad in ϕ and 28 $m$rad in θ. Tracks in the FDC are found using a similar algorithm. Track-finding efficiencies measured from $Z \rightarrow ee$ sample are $80 \pm 1\%$ in the CDC and $74 \pm 1\%$ in the FDC.

4.1.2 Muon chamber

Track-finding in the muon chamber is complicated by the geometry of the detectors and by the bending of the muon in the field of the toroid magnet. A muon passing through layer A of the muon system (Section 3.2.4) which is inside of the magnet will leave hits in up to four PDTs; while muon passing through layers B and C will leave hits in up to three PDTs in each layer. Track segments inside the magnet are defined in layer A which require at least two hits; segments outside the magnet are defined in layers B and C which require at least four hits. All segments are required to point to less than 3-5 m from the center of the detector in order to reduce cosmic background[27]. Segments from layer A are combined with nearby segments from layers B and C to form muon track candidates.

4.2 Event Vertex

The *vertex* is the position within the detector where the proton–antiproton collision occurred and is the location from where the particles in the event emanate. Quantities involving the polar angle (θ) of a particle's direction, such as η, E_T, and, P_T, all depend on the vertex position, so it is a very important measurement.

The beam size is constrained to be approximately 40 μm $\times$ 40 μm in the $x \times y$ plane (well within the beam pipe). The $x \times y$ vertex position changes little from store to store except when some accelerator maintenance or realignment was performed during a shutdown. The average $x \times y$ vertex position for a store is determined online and is used by `RECO`.

Because the proton and antiproton bunches are about 30 cm long in the Tevatron, the z position of the vertex must be measured event by event. `RECO` determines the vertex z position from a histogram of track z-intercepts (see Figure 4.1) using the CDC and the FDC detectors in several steps.

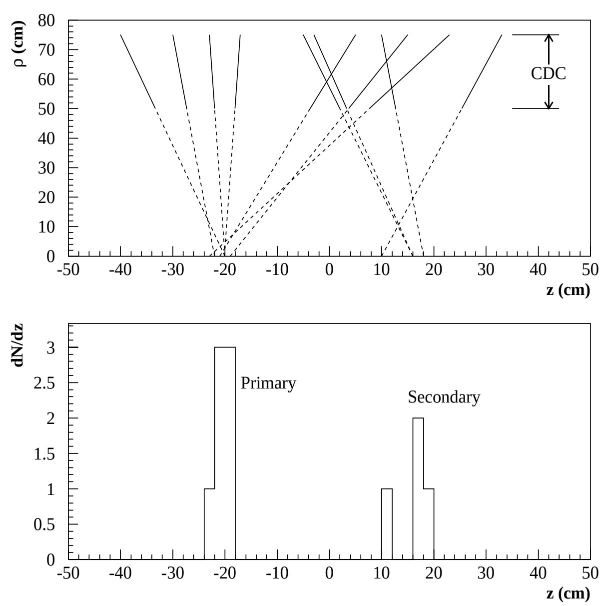

Figure 4.1. Vertex z coordinate determination by the histogram method. Top: projections of CDC tracks to the beam-line (view is integrated over all azimuthal angles ϕ). Bottom: resultant distribution of z-intercepts from which vertices are determined.

1. CDC tracks in the event are extrapolated back to the beam axis to determine where they cross the z axis. The z positions of the intersections are recorded

in a histogram. If the CDC has no tracks, then tracks from the FDC are used.

2. A clustering algorithm is applied to the histogram to find groups of tracks that emanate from the same point in z. A cluster must have at least three tracks, unless only one cluster is found. A Gaussian is then fit to each cluster and the means are recorded as the event vertices.

3. If more than one vertex is found, then the vertex with the most tracks emanating from it is the *primary* vertex. The secondary event vertices are deemed to come from minimum bias interactions[1].

The primary vertex is used to calculate the physics θ and η that go into E_T, P_T, and the $\not{E}_T$ measurements. The vertex z resolution can be as good as 6 mm if many tracks are involved. If a single CDC track determines the vertex, the resolution worsens to 2-3 cm assuming that the track originated from collision. The resolution is $\sim$10 cm if `RECO` must resort to FDC tracks. Multiple vertices are separated if they are at least 8 cm apart. The presence of multiple vertices indicates possible multiple interactions which may cause `RECO` to choose the wrong vertex as discussed in Section 5.3.11.

4.3 Jet Reconstruction

A quark or gluon will hadronize and reveal itself in the detector as a collimated beam or *jet* of hadrons. The algorithm chosen to reconstruct jets affects the number of jets detected, as well as their kinematic features.

[1]The trigger requirement for a minimum bias interaction is that an inelastic collision has happened. Because of the large cross section of QCD parton scattering most minimum bias events are low P_T QCD multijet events.

At DØ jets are identified by the calorimeter. Starting with the cell energy, defined as the directed energy vector $\vec{E}_i$ associated with a calorimeter cell i as

$$\vec{E}_i = \hat{n}E_i, \tag{4.1}$$

where $\hat{n}$ is the unit vector pointing from the interaction point to the center of cell i, and E_i is the magnitude of the energy deposit in cell i. The quantity $\vec{E}_k^{\text{tower}}$ is the energy vector associated with projective tower k; it is the vector sum over all cells in tower k of the cells' energy vectors. The transverse energy of the tower is the magnitude of the projection of this vector into the transverse plane. Thus we define

$$E_T^{\text{tower}} = E^{\text{tower}} \frac{\sqrt{(E_x^{\text{tower}})^2 + (E_y^{\text{tower}})^2}}{\sqrt{(E_x^{\text{tower}})^2 + (E_y^{\text{tower}})^2 + (E_z^{\text{tower}})^2}}. \tag{4.2}$$

Jet finding in DØ starts from these tower E_T values.

In $p\bar{p}$ physics the standard definition of a jet has used a fixed cone algorithm.[29] This algorithm uses a cone of fixed radius R in $\eta \times \phi$ space($R = \sqrt{\eta^2 + \phi^2}$). A radius of $R = 0.5$ is used for this analysis. On average, 91.2% of the initial quark or gluon energy is enclosed by the 0.5 cone[30]. In DØ the cone finding algorithm is implemented as a three step process: preclustering, cone clustering, and splitting/merging. `RECO` is nearly 100% efficient for identifying 0.5 cone jets with $E_T >$ 20 GeV.[31]

4.3.1 Preclustering

1. From an E_T ordered list of calorimeter towers (size $\Delta\eta \times \Delta\phi = 0.1 \times 0.1$), select those with $E_T \geq 1$GeV as seeds.

2. Beginning with the highest E_T seed on the list, All adjacent towers ($E_T \geq 1$ GeV and not already assigned to another precluster) within ± 0.3 units in η

and ϕ are added into the precluster. The towers included in the precluster are removed from the seed list. The total precluster E_T is determined and an E_T-weighted (η, ϕ) centroid is calculated from the component towers.

3. Repeat step 2 until all seed have been examined. Sort the preclusters by E_T.

4.3.2 Cone Clustering

1. Starting with the highest E_T precluster, the E_T weighted (η, ϕ) centroid of the precluster is found and identified as the jet axis. All towers within a radius of R (0.5 for this analysis) in $\eta \times \phi$ are assigned to the jet. The jet axis is recalculated using these towers, and the process is iterated until the jet axis stabilizes, i.e., it moves a distance less than 0.001 in $\eta \times \phi$ space between iterations. A maximum of 50 iterations is allowed to prevent the rare case of a bistable solution from using an unreasonable amount of processing time. The resulting clusters are jets.

2. Recalculate jet variables using towers in the cone:

$$E_i = \sum_{\text{cells } k} E_i^k, \tag{4.3}$$

$$E_T = \sum E_T^k, \tag{4.4}$$

$$E = \sum E^k, \tag{4.5}$$

$$\phi = \arctan(E_y/E_x), \tag{4.6}$$

$$\theta = \arccos\left(E_z/\sqrt{E_x^2 + E_y^2 + E_z^2}\right), \tag{4.7}$$

$$\eta = -\ln\tan(\theta/2), \tag{4.8}$$

where E_i is the directed energy in cartesian direction $i = x, y, z$. Note that E_T is the sum of the individual tower transverse energies, not the magnitude of the vector components, and similarly E is the sum of the individual tower energies. Note also that η and θ are defined with respect to the interaction vertex which is not always at $z = 0$. When reference to a location in the detector is needed we use detector η (η_{det}) which is defined as the pseudorapidity as measured from $z = 0$. Besides jet kinematic quantities, the fractions of the jet energy and E_T in the EM, FH, and CH calorimeters are calculated. These variables are important quality variables in identifying jets. In this analysis, EM fraction and CH fraction are used to identify good jets (Section 5.3.8). The EM fraction is the fraction of the jet's energy that comes from cells in the electromagnetic layers of the calorimeter. CH fraction is the fraction of the jet's energy from coarse hadronic calorimeter cells.

3. If the resulting jet has $E_T > 8$ GeV, the reconstruction threshold, it is stored.

4. Repeat step 1, 2, and 3 on the next precluster. If a precluster is within R (0.5 for this analysis) of any previously found jet, that precluster is skipped.

4.3.3 Splitting and Merging

The first jet by definition can share no energy with a previously found jet. Beginning with the second, each new jet is checked to see if it shares any towers with a previously found jet. If one or more towers are shared, the jets axes are compared; if they are separated by a distance of less than 0.01 in $\eta \times \phi$, the 'new' jet is merely a re-finding of the old jet. This can happen due to roundoff error in the calculations. In this case the 'new' jet is dropped. If they are not identical a decision on whether the system is one or two jets is necessary. To decide, we determine the fraction f_{SM}, defined by

$$f_{\rm SM} = \frac{E_T^{\rm shared}}{E_T^{\rm min}}, \tag{4.9}$$

where $E_T^{\rm shared}$ is the sum of the transverse energies of the common towers, and $E_T^{\rm min}$ is the lesser of the transverse energies of the two jets clusters. If $f_{\rm SM} \leq 0.5$ then two jets are made and each contested cell (not tower) is assigned to the jet whose center is nearest that cell; otherwise, the system is a single jet and all the towers are assigned to it. In either case the jet axis is recalculated one last time, including all the appropriate towers; this is not iterated.

Details of jet resolutions can be found in Reference [32].

4.4 Reconstruction of Transverse Missing Energy

In DØ the calculation of $\not\!\!E_T$ is based upon energy deposits considered at the level of individual cells. With the cell energy vector $\vec{E}_i$ defined in Equation 4.1, the vector $\vec{\not\!\!E}_T$ is defined by

$$\not\!\!E_x = -\sum_{\text{cells } i} E_{xi}, \tag{4.10}$$

$$\not\!\!E_y = -\sum_{\text{cells } i} E_{y_i}, \tag{4.11}$$

$$\vec{\not\!\!E}_T = \hat{x}\not\!\!E_x + \hat{y}\not\!\!E_y, \tag{4.12}$$

$$\not\!\!E_T = \sqrt{\not\!\!E_x{}^2 + \not\!\!E_y{}^2}, \tag{4.13}$$

$$\phi_{\vec{\not\!\!E}_T} = \arctan\left[\begin{array}{c} \not\!\!E_y \\ \not\!\!E_x \end{array}\right]. \tag{4.14}$$

where the sums are over all cells in the calorimeter. $\not\!\!E_x$ and $\not\!\!E_y$ are the x and y components of $\vec{\not\!\!E}_T$, respectively and $\phi_{\vec{\not\!\!E}_T}$ is the azimuthal direction of the $\vec{\not\!\!E}_T$ vector.

The $\not{E}_T$ resolution has been studied elsewhere[33] and is parameterized with S_T defined as the scalar summed transverse energy in the calorimeter. The $\not{E}_T$ resolution is given by,

$$\sigma_{\not{E}_T} = a + b \times S_T + c \times S_T^2, \tag{4.15}$$

where $a = 1.89 \pm 0.05$ GeV, $b = (6.7 \pm 0.7) \times 10^{-3}$, and $c = (9.9 \pm 2.1) \times 10^{-6}$ GeV^{-1}.

4.5 Electron and Photon Reconstruction

Electron and photon candidates are reconstructed using a nearest neighbor clustering algorithm[34]. Starting with the most energetic tower in the EM calorimeter, neighboring towers with $E_T > 50$ MeV are added. A neighboring tower is defined as a tower being adjacent or immediately diagonal in $\eta \times \phi$ space. This process is repeated with the next most energetic tower in the EM calorimeter not already clustered until all unclustered EM towers have $E_T < 50$ MeV. A cluster which satisfies the following criteria is considered as an electron or photon candidate:

- $E_{total} > 1.5$ GeV;
- $E_T > 1.5$ GeV;
- at least 90% of its energy is in the EM calorimeter;
- at least 40% of its energy is in a single tower.

An EM cluster centroid $\vec{x}_{cog}$ is defined as

$$\vec{x}_{cog} = \frac{\sum_i w_i \vec{x}_i}{\sum_i w_i}, \tag{4.16}$$

where the sum is over all the cells in the cluster. w_i is the weight of the ith cell and is defined as

$$w_i = \max(0.0, w_0 + \ln(\frac{E_i}{E_{clus}})), \tag{4.17}$$

and the parameter w_0 was chosen to optimize the position resolution[35]. Electron and photon candidates are then distinguished from each other by whether the cluster has a CDC or an FDC track within a road of size 0.1×0.1 in $\eta \times \phi$ space pointing from the primary vertex to the cluster centroid.

Prompt photon or photon pairs from π° decay can mimic an electron if the shower is overlapped with a random track. Carefully chosen variables have been developed to enhance the selection of purer electrons. These variables are EM fraction of the cluster (f_{em}), shower shape H-matrix chi-squared (χ^2_{hm}), track energy loss per unit path length dE/dx, track match significance (σ_{trk}), and the TRD transition efficiency (ε_{TRD}). Because the TRD only extends to $|\eta_d| = 1.1$, only the first four variables are used for electron candidates in the EC calorimeter. Each variable has different strength in rejecting different backgrounds. For details of these variables, see Reference [36].

4.5.1 Electron likelihood

Each of the five identification variables discussed above has distinguishing power in selecting electron against backgrounds. Some analyses selected electrons by cutting directly on the variables. However, electron and background may not be separated exclusively by a five-dimension box, making straight cuts on several dimensions less optimal. In order to have an optimal discrimination of electron against background, a likelihood ratio is defined:

$$L^e = \frac{p(\vec{x}|b)}{p(\vec{x}|e)}, \tag{4.18}$$

where $p(\vec{x}|b)$ and $p(\vec{x}|e)$ are the likelihood of the variable vector $\vec{x}$, given that they come from background and from an electron, respectively. L^e is called the "electron likelihood" even though it is actually a likelihood ratio. It is found that to a good approximation these five identification variables are independent of each other[37]. Thus $p(\vec{x}|H)$ can be written as

$$p(\vec{x}|H) = p_1(f_{em}|H)\times p_2(\chi^2_{hm}|H)\times p_3(dE/dx|H)\times p_4(\sigma_{trk}|H)\times p_5(\varepsilon_{TRD}|H), \quad (4.19)$$

where H can be b (background) or e (electron).

The last multiplication in Equation 4.19 is not included for EC electrons because there is no TRD coverage in the EC region.

4.5.2 Electron isolation fraction

There is one more variable which helps distinguish electrons from background. It is called the electron isolation fraction, f_{iso}, and is defined as

$$f_{iso} = \frac{E^{tot}_{0.4} - E^{EM}_{0.2}}{E^{EM}_{0.2}}, \quad (4.20)$$

where $E^{tot}_{0.4}$ ($E^{EM}_{0.2}$) is the total energy (EM energy) in a cone of size 0.4 (0.2) in $\eta\times\phi$ space around the centroid of an EM cluster.

This variable is useful in selecting isolated electrons, e.g., those from W decay. It is not included in the electron likelihood because f_{iso} is not really a measure of the electron cluster but rather its environment and is therefore rather sensitive to the physics process being studied.

4.6 Muon Reconstruction

For each muon track candidate (Section 4.1.2), MIP traces are searched for in the hadronic layers of the calorimeter in a wide road of the primary vertex. If layers do not contain energy, searches are conducted in roads formed from secondary vertices. For tracks confirmed by the calorimeter, a road is formed in the central tracking chambers to search for a matching track. At each stage of the track finding, a set of quantities defining the quality of the track is calculated.

The combined information on vertex, the best matching central track, the muon track in the calorimeter, and the tracks in the muon spectrometer are put in a global fit. The muon P_T is determined from the bend of the track due to the muon passing through one of the toroid magnets[38]. Sixteen data points are fit to seven parameters. The sixteen data points include the vertex position in the x and y direction, the angles and positions of track segments, and two angles representing the multiple scattering of the muon in the calorimeter. Of the seven parameters, four describe the position and angle of the track before the calorimeter, two describe the effects due to multiple scattering and the last is the inverse of the muon momentum[27].

Many variables can be used to enhance the muon selection purity against background. Those used in this analysis are

- The quality word of the global track fit (IFW4). IFW4 starts at zero and is increased for each failure of the WAMUS muon track to meet the following quality criteria[39].

  1. Every WAMUS module along the track contributes hits.
  2. Nonbend view impact parameter $\leq$ 100 cm.
  3. Bend view impact parameter $\leq$ 80 cm.
  4. Nonbend view track fit has hit residual RMS $\leq$ 7 cm.

5. Bend view track fit has hit residual RMS ≤ 1 cm.

- Missed layer word (IFW1). IFW1 indicates if the muon is an "A-stub" with only hits in the A layer. If IFW1 $\neq 5$, then the muon is not a A-stub and has hits in the B or C layer.

- MTC quantities: The muon tracking is also possible in the DØ calorimeter using a package (MTC)[40] that runs during reconstruction. Then MTC package uses calorimeter information to identify and reconstruct energy deposits in the calorimeter which appear to lie along a track. It has two primary sections, the muon identification utility and the muon finding utility.

  The muon identification utility takes a given vertex, η and ϕ for a muon candidate and looks at energy deposits in calorimeter cells in a road (5 cell $\times$ 5 cell) or a "core" road (3 cell $\times$ 3 cell) surrounding the muon candidate. The results from this search are the muon calorimeter track, a χ^2 for the track fit, track energy deposits, and the calorimeter layer at which the muon seems to emerge from a jet. The information obtained from this utility is used in the muon identification for the isolated muon veto (Section 5.3.5):

  - The Hfrac value is the fraction of hadronic layers that have a cell contributing to the muon track out of the total number of hadronic layers the track transverses.

  - The Efrac(H1) is the fraction of energy in the outermost layer of the calorimeter within the core road out of the total energy (sum of all layers) within the core.

And χ^2 is used in the MTC cuts (Section 5.3.6) which is defined by

$$\chi^2 = \frac{1}{N_{Layers}} \sum_{i=1}^{N_{Layers}} \frac{(E_i - \lambda_i)^2}{\sigma_i^2}, \tag{4.21}$$

where N_{Layers} is the number of calorimeter layers with a hit cell in the path of the muon candidate, E_i is the energy measured in layer i, λ_i is the most probable value of the energy for a calorimeter cell at that layer and η obtained from the fit results on the test beam muon energy distributions.

The muon finding utility performs a scan of the calorimeter on a cell by cell basis from a given vertex position to find candidate tracks emerging from the vertex. Information from this utility besides the energy associated with the track and the (η, ϕ) of the track are used in the MTC cuts (Section 5.3.6):

- MTC Hfrac is the fraction of hadronic layers used with nonzero energy for the track.

4.7 Corrections

Various corrections must be applied to the physics objects. Only those concerning jets and $\not\!\!E_T$ are described here.

4.7.1 Jet Corrections

A sampling calorimeter measures only a small fraction of the energy it absorbs. Data from a test beam, where the response of calorimeter modules from electrons and pions of known energies is measured, are used for basic calibration and determination of the sampling weights. Test beam data, however, cannot give the final corrections. So after reconstructing electromagnetic and hadronic jets, we calibrate their energies and measure their energy resolutions.

One would like to determine the energy of the original parton that produced the jet. The calorimeter measures the energy "flow" of the jet, which is related to the energies of the constituent particles in the jet, and, in some way, is related to the energy of the original parton. The energy scale determines the correction factor that gives, on average, the energy of the jet at the particle level when applied to the measured jet energy. The particle level energy should be close to the energy at the parton level, but the details depend on the model of parton fragmentation. The corrections described here do not attempt to go back to the parton level, which is fine for the purposes of this analysis. In any detector, a particle's true energy (E_{true}) can be expressed as a function of the measured jet energy ($E_{measured}$); studies have shown that in the DØ calorimeter, the following function applies over the full range of energies used in this analysis:

$$E_{true} = \alpha E_{measured} + \beta. \tag{4.22}$$

Thus, our energy calibration involves only the measurement of α (the "scale") and β (the "offset"). Jet corrections are described in much detail elsewhere.[41] The main corrections that are made to the reconstructed jet energy are listed below:

Scale correction: **Overall calorimeter response correction:** There are some inaccuracies in the energy calibration prior to the Run. Unlike test beam data, in $p\bar{p}$ collision data, resulting clusters of hadronic particles incident on the calorimeter will not always strike the center of the calorimeter cells, nor will they always strike at a 90° angle. Some energy is lost in intermodule cracks and other dead (uninstrumented) material. In addition, the calorimeter response non-linearity at low energy and the calorimeter non-uniformity must be taken into account.

Out-of-cone showering correction: The cone used by the jet algorithm may not be large enough to enclose for all of the energy of a jet. A correction is made for the energy leaking outside of the cone.

Offset correction: The contributions to the offset come from energy within the jet which did not originate from the initial high energy particles. The remnants of the proton and antiproton that are not involved with the hard scattering may deposit some energy in the detector. In addition, soft $p\bar{p}$ collisions that occur in the same beam crossing as the hard scattering, may contribute to the energy of the jets. There is also noise in the calorimeter system due to the radioactivity in the uranium plates and electronic noise. Finally, the *pileup* effect resulting from the calorimeter response to the $p\bar{p}$ interactions in previous beam crossings may affect jet energies.

Some details on how these corrections are applied are given below.

4.7.2 Electromagnetic Energy

We use the $Z \rightarrow ee$, $J/\psi \rightarrow ee$, $J/\psi \rightarrow \gamma\gamma$, and $\pi^0 \rightarrow \gamma\gamma$ data to measure the electromagnetic offset, and the Z sample to determine the scale. Since the masses of the Z, J/ψ, and π^0 have been measured to a high degree of precision, the correction factors can be obtained by reconstructing the masses using the measurements of the energies of the two electrons or photons in the x, y, and z directions.

4.7.3 Hadronic Energy

The basic form of the hadronic jet energy correction is,

$$E_{true}^{\text{jet}} = \frac{E_{measured}^{\text{jet}} - O(R, \eta, \mathcal{L})}{R_{\text{jet}}(R, \eta, E_T) S(R, \eta, E_T)}, \tag{4.23}$$

where E_{true}^{jet} is the "true" energy of the jet at the particle level, O is the offset correction, S is the out-of-cone showering correction, R_{jet} is the overall calorimeter response correction, R is the cone size, and $\mathcal{L}$ is the instantaneous luminosity.

The hadronic offset correction is determined from data taken every thousandth beam crossing (*zerobias*) and data taken every hundredth inelastic collision (*minbias*)[2]. The minbias data provides an estimation of the contribution of the proton and antiproton remnant from an inelastic collision, while the zerobias data provides an estimate of the other contributions to the hadronic offset. The hadronic offset is cone size, pseudorapidity and luminosity dependent.

The out-of-cone showering correction is determined from Monte Carlo events overlayed with test beam data. This correction depends on jet cone size, E_T and η.

The overall response correction is measured from data using the Missing P_T Projection Fraction (MPF) method.[41] The basic idea is that the hadronic energy scale is determined by balancing jets against a highly electromagnetic object (a high quality photon or electron). For unbiased results, the EM object is used to trigger the event. Since the EM energy scale is well known and the EM calorimeter resolution is very good, EM objects are measured precisely. Any $\not\!\!E_T$ in the event is then due to mismeasurement of the hadronic jets, since no neutrinos are expected. The hadronic energy scale is computed by projecting the $\not\!\!E_T$ vector along photon direction. There are few photon events with high E_T jets, and so Monte Carlo samples are used to

[2] *Minbias* data is collected when the Level-Ø hodoscopes indicate a hard $p\bar{p}$ collison has occured with no additional trigger requirements. *Zerobias* data is collected during a beam crossing without regard to Level-Ø information.

extend the response measurement. The overall response correction and it's error are parameterized as a function of the jet cone size, E_T and η.[41]

4.7.4 Missing Transverse Energy Corrections

Since the jet corrections change the E_T of the jets in the event, the $\not{E}_T$ should change as well. The only corrections that are applied to the $\not{E}_T$ vector are those from the electromagnetic and hadronic response. Thus, the $\not{E}_x$ and $\not{E}_y$ components of $\not{E}_T$ are adjusted to reflect the response corrections to each jet in the event.

The other corrections are not made to $\not{E}_T$ for various reasons. The offset correction, O, is assumed to be ϕ independent. Since $\not{E}_T$ is calculated by summing over all the cells in the calorimeter, the effects of O cancel. Similarly, the out of cone corrections, S, reflect energy lost by the algorithm. $\not{E}_T$ is independent of the jet algorithm, and so S does not apply as well.

The error on the $\not{E}_T$ is the cumulative effect of applying the energy scale error to each jet and then adjusting the $\not{E}_T$ accordingly.

4.8 Anomalous Energy Deposits

Anomalous energy deposits, or hot cells, are isolated calorimeter cells measuring a large amount of energy. Since electrons, photons, and jets typically span many cells, these hot cells are probably caused by intermittent shorts or sparks in calorimeter modules due to contaminants in the liquid argon or contaminants inside the modules themselves. A hot cell can generate $\not{E}_T$ and spurious jets. Since events with hot cells will quickly drive up trigger rates and swamp high $\not{E}_T$ data samples, a "hot cell killer" run at Level-2 for some triggers and in the reconstruction program removes isolated high energy cells from events.

The hot cell killer, called `aida`[42], removes hot cells by looking for large energy deposits that are isolated *longitudinally*. For a cell to be removed, it must meet the following criteria,

- The suspect cell must have $E_T > 10$ GeV.
- $\langle E \rangle_{\text{neighboring cells}} < 0.05 E_{T_{\text{suspect cell}}}$, where $\langle E \rangle_{\text{neighboring cells}}$ is the average *energy*[3] of the longitudinally neighboring cells.

`aida` does not examine transverse neighbor cells. The hot cell killer in Level-2 can only remove one hot cell from the $\not{E}_T$ and total scalar E_T calculations and was only run on events taken by the `missing_et, jet_2_miss` and `scalar_et` triggers. `aida` in `RECO` will remove as many hot cells as it finds. Those removed cells will not be included in $\not{E}_T$ and scalar E_T calculations and will not make up any jets.

The hot cell killer keeps spurious events with large $\not{E}_T$ due only to a hot cell from swamping the high $\not{E}_T$ data sample. Unfortunately, `aida` can sometimes inadvertently remove perfectly good cells that are within jets. The effects of such mistakes are discussed in Section 5.3.4.

[3] `aida` package has a mistake in its code. Instead of calculating the average of the transverse energies of the neighboring cells `aida` actually calculates the average of the energies of the neighboring cells.

CHAPTER 5

ANALYSIS

5.1 Collider Data

This analysis is based on the Run 1B and Run 1C data (runs 72250-93115 and 94478-96972) collected from December 1993 through February 1996 with two unprescaled triggers: `missing_et` for Run 1B and `missing_et_high` for Run 1C. The collected data were reconstructed using `RECO` version 12 with the standard DØ fixed cone jet-finding algorithm for jet cone sizes of 0.3, 0.5, 0.7 and 1.0. This study is limited to jets with cone size of 0.5. After the reconstruction, the data were streamed into manageable file sets and the jet and $\not\!\!E_T$ corrections were applied with the cafix v5.1 software package.[41, 43]

5.1.1 Missing_et and Missing_et_high Triggers

The triggering in DØ is done in a multi-stage system consisting of three basic trigger levels. The `missing_et` and `missing_et_high` triggers exist at Level 1 and Level 2.

At Level 1, `missing_et` and `missing_et_high` require a desired number of trigger towers (0.2×0.2 in $\eta \times \phi$ space) to have $E_T \geq 3$ or 5 GeV as well as Level 1 $\not\!\!E_T$ to be above a certain threshold. Detector pseudorapidity (η_d) of a Level 1 trigger tower can be as high as 4.0 for Run 1B and 2.0 for Run 1C. The Level 1 $\not\!\!E_T$ is cal-

TABLE 5.1. MISSING_ET AND MISSING_ET_HIGHCONFIGURATIONS.

Name	Runs	Level 1 (GeV)	Level 2 (GeV)
missing_et	≤ 85276	$\lvert\eta_d^{\rm jets}\rvert \leq 4$ 1 jet ($E_T \geq 3$) $\not\!\!E_T \geq 30$	$\not\!\!E_T \geq 35$
missing_et	≥ 85277	$\lvert\eta_d^{\rm jets}\rvert \leq 4$ 1 jet ($E_T \geq 5$) $\not\!\!E_T \geq 40$	$\not\!\!E_T \geq 40$
missing_et_high		$\lvert\eta_d^{\rm jets}\rvert \leq 1$ 1 jet ($E_T \geq 5$) $\not\!\!E_T \geq 50$	$\not\!\!E_T \geq 50$

culated from trigger towers within $|\eta_d| \leq 2.4$. The coarse hadronic layers, Massless Gaps, and intercryostat detectors are not included in Level 1 trigger towers and, hence, do not contribute to the Level 1 $\not\!\!E_T$ calculation. The triggers also require good_beam, reflecting the fact that the trigger is inhibited from taking data while the Main Ring is in injection or transition (MRBS_LOSS) or while Main Ring protons are passing through the DØ calorimeter (MICRO_BLANK).

If Level 1 accepts an event, it passes information onto Level 2, also providing it with the list of Level 1 trigger towers. At Level 2, jet-like clusters are reconstructed starting from the "seed" tower list from Level 1. Around each trigger seed centroid, a box of 1.4×1.4 in $\eta \times \phi$ is drawn. The E_T-weighted centroid of this box is taken as a Level 2 jet center. All trigger towers not already claimed by other Level 2 jets are then summed up within a fixed cone radius of 0.7 in $\eta \times \phi$ drawn from the Level 2 jet centroid. Level 2 uses the entire calorimeter for the $\not\!\!E_T$ calculation and may remove at most one cell flagged as hot by the hot cell killer.

The missing_et and missing_et_high requirements are summarized in Table 5.1.

LED events have a hard jet and high $\not\!\!E_T$. As shown in the event selection criteria below, the jet E_T and $\not\!\!E_T$ reauirement (denotes as $E_T/\not\!\!E_T$ from now on) ensures that `missing_et` and `missing_et_high` triggers are fully (100%) efficient based on E. Popkov's trigger study[44].

5.2 Fast MC QSIM

Due to the lack of available resource and support and the traditional detector simulation GEANT[54] being too slow, we use the fast MC QSIM for detector simulation. In the program "Quick Simulation" - QSIM[55], stable interacting particles (not neutrinos or LSP's), which are generated by a physics generator (PYTHIA[56] for this analysis in particular), are grouped into jets by the D0pjet algorithm[58] when they hit the calorimeter or are simply designated as electrons or muons if they are isolated from the jets. The energies of these objects are smeared according to their resolutions as measured from data. $\not\!\!E_T$ in QSIM is calculated based on all the smeared objects as well as the unclustered energy. Comparison of QSIM and GEANT found that the agreement between the respective jet and electron E_T spectra as well as the $\not\!\!E_T$ spectra was very good[57].

PYTHIA includes a model for hadronization, as well as for the production of additional quarks or gluons in the event (initial and final state radiation). To decay any taus in the event, we use TAUOLA[60] interfaced with PYTHIA. Most signal and background MC samples (except $W/Z \to \tau$) are generated in PYTHIA with the lower limit of transverse momentum for hard $2 \to 2$ processes at $\sim 3\sigma_{\not\!\!E_T}$ below 100 GeV. This is done to impose an initial E_T threshold in order to reduce the number of events we need to process. The $\not\!\!E_T$ resolution $\sigma_{\not\!\!E_T}$ is defined in Equation 4.15. $W/Z \to \tau$ (inclusive) MC samples are generated with the lower limit of transverse momentum for hard $2 \to 2$ processes at 10 GeV.

5.3 Event Selection Criteria

The goal of event selection criteria or *cuts* is to select as many signal events while rejecting as many background events as possible. Using appropriate MC and data samples, differences between the signal and backgrounds are studied and thus the cuts are developed based on the understanding of the differences. The subsequent sections describe the selection criteria and the differences between signal and background events to justify them.

5.3.1 Total Calorimeter Scalar Transverse Energy

In order to eliminate events due to high energy cosmic rays showering in the calorimeter and calorimeter electronics failures (e.g., bad BLS cards), events are required to have no greater than 1.8 TeV of scalar transverse energy (S_T) deposited in the calorimeter. S_T is defined as the scalar sum of cell E_T over the entire calorimeter. Events are also required to have $S_T \geq 0$ GeV. This requirement eliminates events with large amounts of negative energy in the calorimeter. Negative energy arises when a previous event saturated some calorimeter preamps, and the current event was taken before those preamps returned to baseline levels. The efficiency of the S_T requirement was studied elsewhere[46] and was found to be 100% for hard scattering events.

5.3.2 Scalar Transverse Energy of the Main Ring Region

Protons traveling in the Main Ring accelerator (MR) can be lost in the regions where the MR passes through the DØ detector resulting in large energy deposits in

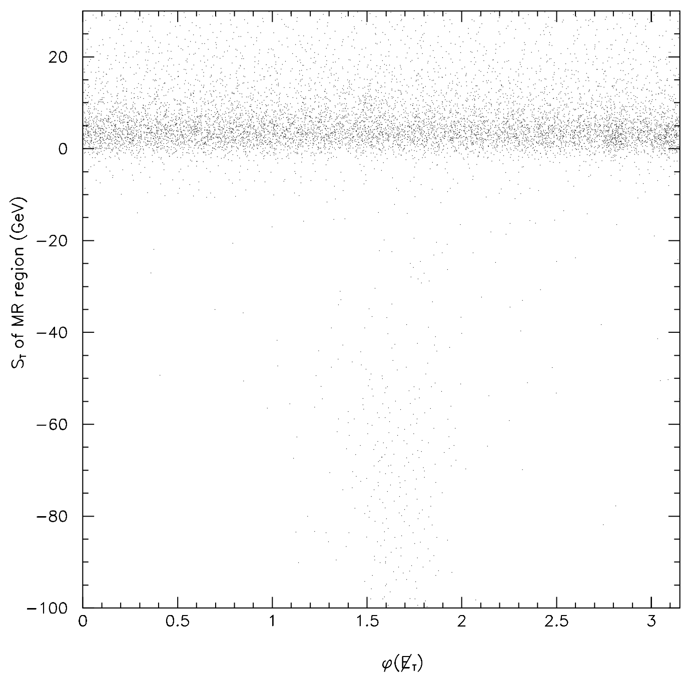

Figure 5.1. S_T of the MR region for events with $\not{E}_T > 60$ GeV collected by `missing_et` and `missing_et_high` triggers.

the MR Region of the calorimeter (all CC Coarse Hadronic and EC Outer Hadronic cells). Most of the events with false jets and/or $\not{E}_T$ due to MR activity are removed by vetoing the `MRBS_LOSS` and `MICRO_BLANK` terms, by the scalar transverse energy requirement (Section 5.3.1) and by the "good jet" requirement (Section 5.3.8). It was observed that a small fraction of events collected by the `missing_et` triggers may have a significant $\not{E}_T$ due to negative energy in the MR region. Figure 5.1 shows the scalar transverse energy of the MR region[1] vs $\phi_{\not{E}_T}$ for `missing_et` events with $\not{E}_T$ >60 GeV. It is clearly shown that the negative energy in the MR region causes $\not{E}_T$ to point in the direction of the MR region ($\phi_{\not{E}_T} \sim 1.7$). In order to suppress such events, S_T of the MR region ($S_T^{\rm MR}$) is required to be larger than –10

[1]The scalar transverse energy of the MR region is defined as the scalar sum of cell E_T over all CC Coarse Hadronic and EC Outer Hadronic cells with $1.57 < \varphi < 1.96$.

GeV. The efficiency of that requirement is derived from the data collected by the inclusive jet triggers. Since a very small fraction of the events does not pass the $S_T^{\mathrm{MR}} > -10$ GeV requirement, the efficiency is assumed to be 100 %[44].

5.3.3 Vertex Position

To assure that events are well centered in the detector, the z-position of the primary vertex determined by the DØRECO program is required to be within ± 60 cm of the center of the detector. The distribution of the z-position of the primary vertex is studied with $Z \to ee$ sample. The shape of the distribution is compatible with a Gaussian centered at zero and sigma of 25.5 ± 0.27 cm[44]. For MC samples, this requirement is applied to the simulated vertex position. As shown in Figure 5.2, the variation in the z position is about 200 cm.

5.3.4 Removed Cells from Jets

Anomalous isolated high energy calorimeter cells (hot cells) can generate $\not{E}_T$ and spurious jets. The hot cell killer routine, `aida`, runs at Level 2 for the `missing_et` triggers. Rarely, it has been observed that a jet will have a longitudinal shower profile such that a cell within a jet cone will meet the removal criteria, although the cell's energy is probably not anomalous. Even though it is rare for the hot cell killer to remove a cell from a real jet, this "overefficiency" has a significant effect on the determination of the QCD multijet background. Applying a $\not{E}_T$ requirement also tends to select such balanced events with a good cell removed and enhances the contamination. Since it would take a significant amount of effort to employ a better

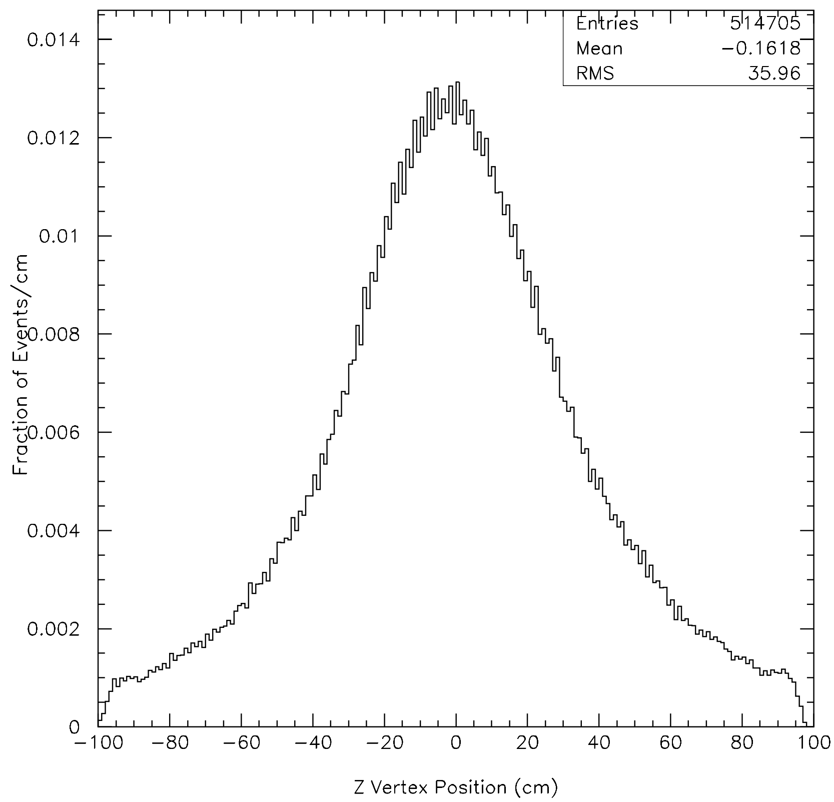

Figure 5.2. The z- position of the primary vertex of the events in the `missing_et` and `missing_et_high` data set.

hot cell removal algorithm[2] and the hot cell background is very hard to simulate, events with hot cells in jets are rejected altogether. The following criteria must be met to reject such events:

- A cell that was removed by `aida` must be within $\Delta R = 0.707$ (in $\eta \times \phi$ space) of the axis of a jet.
- That jet must have $E_T > 15$ GeV and $|\eta| < 3.5$.

An LED event will be rejected if a jet has a cell removed by `aida`, so an efficiency must be calculated. As shown in the study by E. Popkov[44], a measurement of the efficiency from the data was obtained with a sample of clean events that are not enhanced in hot cells using the `ele_1_mon` and `em1_gis_high` triggers. To simulate the effects of `aida` removing cells from jets, each MC event (signal and background) is rejected with a probability determined from the study[44] by applying to each jet the efficiency according to its η and E_T.

As for jet with $E_T \leq 15$ GeV or $|\eta| \geq 3.5$, the removed cells are added back in unless they are true hot cells (cells found by the QCD group that appeared to be recurring hot cells)[45] and jet E_T and $\not{E}_T$ are recalculated.

5.3.5 Isolated Muon Veto

Since only LED events with hadronic cascade decays are sought, events with isolated muons (with respect to the leading jet) are vetoed (electrons and photons are vetoed with the "good jet" requirements discussed in 5.3.8 to avoid the leading jet being an EM object). An event is rejected if it has a muon meeting the standard loose

[2] One would have to recover hot cells back into jets, apply a new hot cell killer and recalculate parameters of jets and $\not{E}_T$ for all data events of interest. That is a very intensive CPU and data handling task.

muon criteria used by the DØ Top group as shown in Table 5.2.[46, 47] Here prezap

TABLE 5.2. REQUIREMENTS FOR MUON REJECTION.

Prezap (Run # $<$ 89,000)	Postzap	
CF μ (Quadrant $\leq$ 4)	CF μ (Quadrant $\leq$ 4)	EF μ (4 $<$Quadrant $\leq$ 12)
IFW4 $\leq$ 1	IFW4 $\leq$ 1	IFW4 = 0
P_T >15 GeV		
(Hfrac >0.6 and Efrac(H1) >0) or Hfrac = 1		
IFW1 $\neq$ 5		

(Run # $<$ 89,000) is when only CF muons ($|\eta|$<1) are vetoed when forward muon chambers suffered low efficiency due to accelerated aging[48],[49], IFW4 is the muon quality word, Hfrac is the fraction of hadronic layers that have a cell contributing to the muon track out of the total number of hadronic layers the track traverses, Efrac(H1) is the fraction of energy in the outermost layer of the calorimeter within the core road out of the total energy (sum of all layers) within the core, IFW1 is the missed layer word, as shown in Section 4.6.

The standard loose muon criteria require a good quality track in the muon system with $p_T > 15$ GeV that has an associated good quality muon track in the calorimeter. In addition, in order to reduce the LED signal inefficiency due to vetoing events with b-quark muons from the leading jet, only events with muons isolated from the leading hadronic activity are rejected.

The muon veto is applied to all signal and background samples. For Monte Carlo, there is a correction to the efficiency. If a muon meeting the muon criteria is found in a Monte Carlo event, the event is rejected at a rate[46, 47] given in Table 5.3 and for non-musmear MC (QSIM) there is a correction factor of 0.718 on the efficiencies which comes from a $W \rightarrow \mu\nu$ + jets MC sample by comparing the numbers of events passed by the GEANT and QSIM detector simulations.

TABLE 5.3. CORRECTIONS TO MONTE CARLO MUON EFFICIENCIES

Quadrant	Multiplicative Efficiency	
	musmear Postzap Monte Carlo	non-musmear MC
CF	0.937	0.815
EF	0.400	0.337

5.3.6 MTC Cuts

There exists the possibility of losing the muon either because of inefficiency in the muon reconstruction software, chamber inefficiency, or just plain holes in the muon detector coverage. Therefore, to suppress the muon contamination from either W/Z decays or cosmics, Muon Tracking in the Calorimeter package[40] is used to recover the lost muons. The MTC track selection criteria[52] are listed in Table 5.4. The

TABLE 5.4. MTC TRACK SELECTION CRITERIA.

$\Delta\phi_{MTC-\not{E}_T} < 0.25$
$\lvert\eta_{MTC}\rvert < 1.7$
$MTC\ Hfrac > 0.9$
$\chi^2 < 10$
$0 \leq N_{Layer} \leq 18$
$E_{track} > 1/2$ GeV for $\lvert\eta_{MTC}\rvert \leq 1.0$
$E_{track} > 1$ GeV for $\lvert\eta_{MTC}\rvert > 1.0$

MTC matching efficiency is $(94.0 \pm 0.8)\%$[53], and the fake rate is $(11.3 \pm 1.5)\%$[52]. Furthermore, the MTC track is required to be isolated (with respect to the leading jet): $\Delta R_{MTC-jet} > 0.5$.

5.3.7 Missing Transverse Energy Requirement

Missing transverse energy is one of the most powerful discriminants used in selecting LED events and rejecting backgrounds. This analysis uses calorimeter $\not{E}_T$ after jet corrections. The $\not{E}_T$ thresholds used are greater than 150 GeV for `missing_et` and `missing_et_high`. The $\not\!\!E_T$ requirement is applied to all signal and background Monte Carlo samples.

5.3.8 Leading Jet Requirements

The LED events can typically have large missing transverse energy and a high P_T jet. To be as inclusive as possible while providing background rejection, we impose the requirement that an event must contain a "good" leading jet having corrected $E_T > 150$ GeV. We will show the results for $|\eta_d| \leq 1.0$, $|\eta_d| < 1.1$ or $1.5 < |\eta_d| \leq 2.5$, and $|\eta_d| \leq 2.5$ for the purpose of a general study.

A "good" jet must pass the clean jet requirements shown in Table 5.5, where the EM fraction and CH fraction are the fraction of the jet's E_T deposited in the electromagnetic and coarse hadronic layers of the calorimeter, respectively.

TABLE 5.5. GOOD JET REQUIREMENTS.

$0.1 \leq$ EM Fraction ≤ 0.9
CH Fraction ≤ 0.4
$\|\eta_d\| \leq 2.5$

The low end EM fraction requirement eliminates jets formed from hot cells in the hadronic calorimeter. The high end EM fraction cut eliminates electrons and photons, since they deposit nearly all of their energy in the EM calorimeter. The calorimeter was built so that hadronic jets shower in the FH with the CH catching the tails. A jet showering predominately in the CH is in reality probably noise in a CH module or losses from the Main Ring accelerator, hence the purpose of the CH fraction requirement. The η range restriction assures that the jet is not extremely forward and close to the beam pipe. For MC QSIM samples, the efficiency obtained from data is applied according to the jet detector η and jet E_T .[44]

5.3.9 Second Jet Requirements

The LED events can have one or more jets from initial or final state radiation. They are soft jets so we require the second leading jet have $E_T < 50$ GeV to suppress the QCD background. In order to further suppress the QCD multijet events with mismeasured jets, we have imposed an additional requirement: removal of events with $|\Delta\phi_{jet(2)-\not{E}_T}| \leq 15°$ if the second jet has $E_T \geq 15$ GeV and $|\eta_d| \leq 2.5$, which is comparable to the level 2 requirement of some other triggers such as `jet_2_miss` with $|\Delta\phi_{jet(2)-\not{E}_T}| > 0.25$[44]. Figure 5.3 shows the distribution of the $\Delta\phi_{jet(2),\ \not{E}_T}$ for the data sample and MC samples of $Z \rightarrow \nu\nu$ + jets and a set of n and M_D for LED production (a "signal point") with the leading jet $\mathrm{E}_T/\not{E}_T > 115$ GeV and the second jet $\mathrm{E}_T < 50$ GeV and $|\eta_d| \leq 2.5$. We remove events with $|\Delta\phi_{jet(2)-\not{E}_T}| \leq 15°$, as they arise predominantly from measurement errors.

5.3.10 Cosmic Ray Rejection

Cosmic ray radiation can contaminate collider samples, resulting in unbalanced calorimeter energy. If the energy is reconstructed as a jet, it can result in a final state of one (or more) jets and $\not{E}_T$, which is our signal signature. Thus the identification and removal of cosmic rays is an important part of our analysis.

A cosmic ray can produce a monojet plus $\not{E}_T$ final state in two ways: through photon radiation and through minimum ionization in the cells. In the first case, a high energy cosmic ray muon radiates a high energy photon, resulting in a single high E_T jet. In the second case, a cosmic ray muon travels roughly parallel to the beam line, traversing a longer distance in a given cell than a collision-induced muon. The minimum ionization of such a muon can be reconstructed as a high E_T jet.

To identify cosmic ray jets coming from photon radiation, the jet EM energy

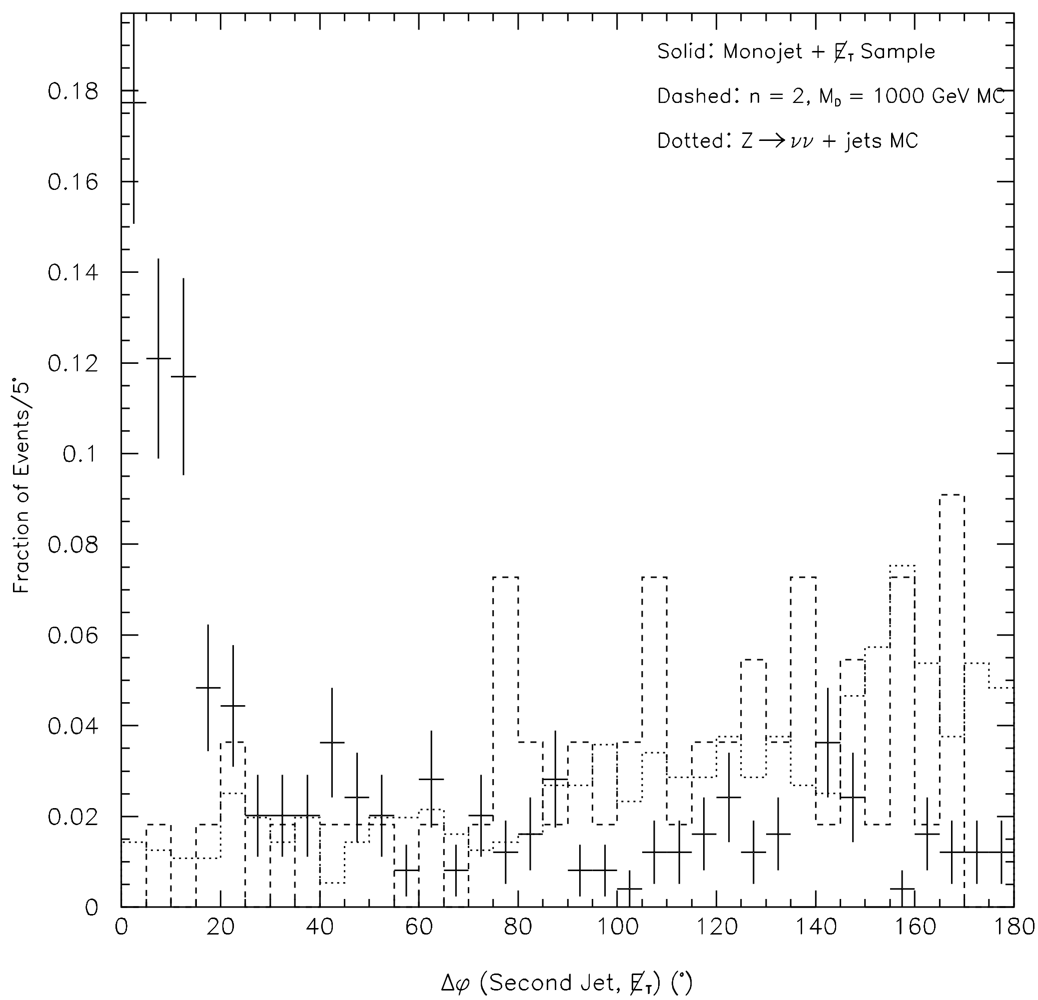

Figure 5.3. The $\Delta\phi_{jet(2),\ \not{E}_T}$ distribution for jet + $\not{E}_T$ data (solid), signal MC for n = 2, M_D = 1000 GeV (dashed), and $Z \to \nu\nu$ + jets MC (dotted); the latter two samples have been normalized to the data.

fraction and jet EM-FH boundary energy fraction are useful. The requirement that leading jet have $0.1 \leq$ EM fraction ≤ 0.9 removes many cosmic ray events from a given data sample[51]. For example, this EM fraction cut removes $\sim 70\%$ of events in a cosmic ray sample (data taken with beam off). Additionally, this EM fraction cut is already part of our "good jet" requirement, see 5.3.8.

Though the EM fraction cut removes most of the localized photons, it does not remove photons emitted by cosmic rays at the junction between the Electromagnetic(EM4) and Fine Hadronic (FH1) layers of the detector. Such events will have roughly equal amounts of EM and hadronic energy, corresponding to an EM fraction of around 0.5. So the EM fraction cut has no effect on such events, and the EM-FH boundary energy fraction for central leading jets ($|\eta_d| \leq 1.0$)[51] is used:

$$f^{em-fh} = (E_T^{em4} + E_T^{fh1})/E_T^{jet}.$$

With the comparison of our missing_et data and jet data[51], the cut is set at $f^{em-fh} < 0.7$. As for the events with no central leading jet, there is no rejection of them by this cut. Since the statistics are low at high jet E_T, we measure the efficiency of this requirement as a function of jet E_T using multijet events. As shown in Figure 5.4, the linear fit gives the result of $(98.5 \pm 0.2)\%$ with χ^2 of 0.6284.

To identify cosmic ray jets coming from minimum ionization, the jet EM tower weight is useful. The shower shapes of the jets from minimum ionization of cosmic rays are different from the jets arising from a beam collision. Collision-induced jets shower radially from the beam axis, and are thus contained in a narrow region in $\eta \times \phi$ space while spreading through several radial regions (electromagnetic, fine hadronic and coarse hadronic). The "jets" produced by cosmic ray muons generally do not pass through the beam axis, and thus deposit energy in a broader region in $\eta \times \phi$ space. So the energy in a given $\eta \times \phi$ tower is contained in a particular radial region. To remove this type of cosmic ray, the EM tower weight for central

($|\eta_d| \leq 1.1$) and forward leading jets ($|\eta_d| > 1.4$)[51] is used:

$$w_{em}^{tower} = \sum (2 \times |f_{em}^i - 1/2| \times E_T^i / E_T^{jet}),$$

where the sum is over the towers in the jet. w_{em}^{tower} is close to one if most of the jet's energy is contained in towers with either high or low EM fraction. With the comparison of our missing_et data and jet data[51], the cut is set at $w_{em}^{tower} < 0.92$. As for the events with neither central nor forward leading jet, there is no rejection of them by this cut. We measure the efficiency of this requirement as a function of jet E_T using multijet events. As shown in Figure 5.4, the linear fit gives the result of $(99.0 \pm 0.2)\%$ with χ^2 of 1.261.

5.3.11 Confirmation of the Primary Vertex

In events with two or more inelastic collisions, the vertex from a low energy collision would be mistakenly associated with that of a high energy collision if more tracks emanate from the vertex of the low energy collision. When a jet is reconstructed with the incorrect vertex, the jet cone is incorrect, and thus we fail to measure the energy that falls outside the incorrect cone and inside the true cone. The transverse energy measurement depends on the location of the vertex and the jet energy corrections compound E_T measurement errors. Hence vertex measurement error can result in significant jet E_T and $\not{E}_T$ measurement errors.

To reduce the effects of vertex measurement error, we use the central ($|\eta_d| \leq 1.0$) leading jet to confirm the location of the primary vertex[50]. If the leading jet is central, the "jet vertex" is calculated by averaging the z positions of the CDC tracks within a 0.5 cone of the jet. Since particles from a secondary vertex can pass through the jet's cone, the cone may include tracks that are not part of the jet. To correct

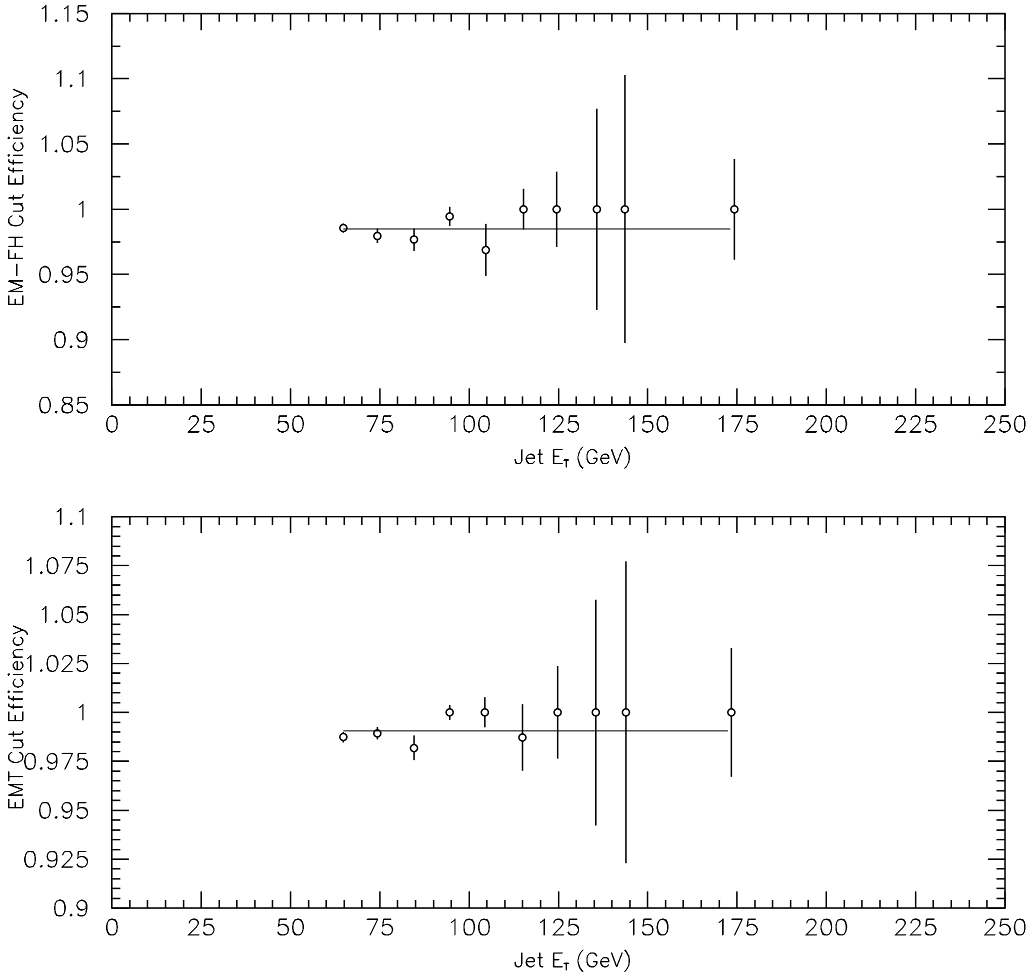

Figure 5.4. EM-FH fraction and EM tower weight cut efficiencies as a function of jet E_T using multijet Events.

for this, we remove the track with the largest deviation from the jet vertex, if the deviation is at least 10 cm ($\sim 5\sigma$). We recalculate the jet vertex and again remove the track with the largest deviation, until no tracks deviate by more than 10 cm from the jet vertex. As for the events with no central leading jet, we assume the primary vertex is ok and keep the events.

We require the distance between leading jet vertex and the reconstructed vertex in z to be less than or equal to 10 cm, which is chosen to maximize the statistical significance of the signal in our data set as shown in Section 5.6.2.1. Since the statistics are low at high jet E_T, we measure the efficiency of this requirement as a function of jet E_T using multijet events. As shown in Figure 5.5, the linear fit gives the result of $(89.8 \pm 0.6)\%$ with χ^2 of 0.7142. In addition, a systematic error is assigned to take into account the events with a single jet where the primary vertex is determined from the tracks of the jet. This topology is not included in the multijet events for single interactions. In the case of multiple interactions, the assumption that the jets are independent means the multijet events should provide an estimate of the jet vertexing efficiency of either single jet or more than one jet. The systematic error is determined from the difference between the efficiency obtained from the multijet events with single interactions and the efficiency from signal MC. The difference is then weighted by the expected percentage of single interactions which gives us an overall systematic error of 1.1% for the vertex confirmation efficiency.

5.4 Applying Analysis Requirements to Data

Using the selection requirements, we define a jet + $\not\!\!E_T$ data sample in which we perform our search for LED. Table 5.6 shows the number of `missing_et` and `missing_et_high` events that pass each successive requirement.

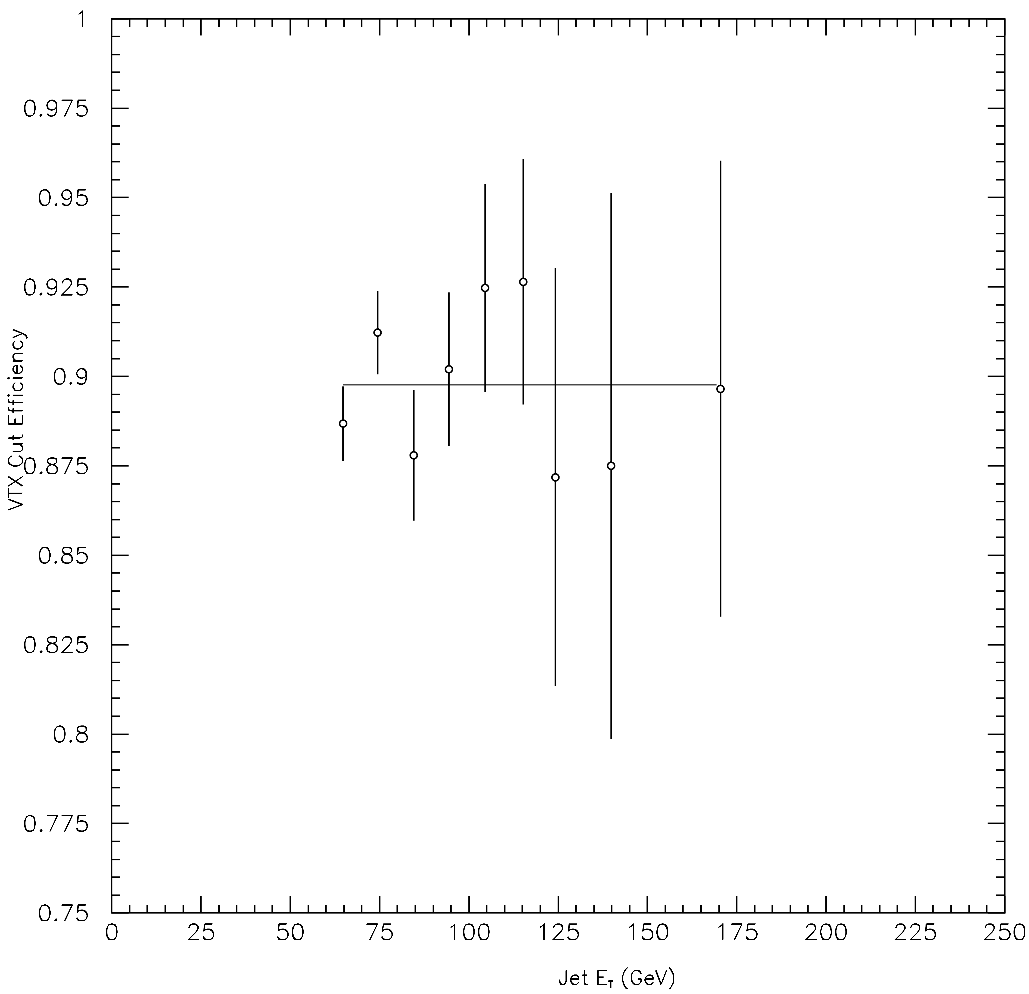

Figure 5.5. Primary vertex confirmation cut efficiency as a function of jet E_T using multijet events.

TABLE 5.6. OBSERVED NUMBER OF EVENTS PASSING EACH REQUIREMENT IN `MISSING_ET`AND `MISSING_ET_HIGH` DATA WITH THE LEADING JET $\mathrm{E}_T/\not\!\!E_T > 150$ GeV AND THE SECOND JET $\mathrm{E}_T < 50$ GeV.

<table>
<tr><td>Cut</td><td colspan="3">Number of Events</td></tr>
<tr><td>No bad runs</td><td colspan="3">461,505</td></tr>
<tr><td>S_T requirements</td><td colspan="3">459,169</td></tr>
<tr><td>Main ring vetos</td><td colspan="3">457,243</td></tr>
<tr><td>Primary vertex position</td><td colspan="3">404,693</td></tr>
<tr><td>Hot cell requirements</td><td colspan="3">301,325</td></tr>
<tr><td>Isolated muon veto</td><td colspan="3">296,742</td></tr>
<tr><td rowspan="2">The leading jet, $\not\!\!E_T$ and the second jet requirements</td><td>$|\eta_d| \leq 1.0$</td><td>$|\eta_d| < 1.1$ or $1.5 < |\eta_d| \leq 2.5$</td><td>$|\eta_d| \leq 2.5$</td></tr>
<tr><td>141</td><td>158</td><td>171</td></tr>
<tr><td>$\Delta\phi_{jet(2)-\not\!\!E_T}$ requirement</td><td>129</td><td>146</td><td>158</td></tr>
<tr><td>Cosmic ray rejections</td><td>69</td><td>78</td><td>90</td></tr>
<tr><td>Primary vertex confirmation</td><td>39</td><td>48</td><td>60</td></tr>
<tr><td>MTC requirements</td><td>38</td><td>47</td><td>58</td></tr>
</table>

5.5 Background Estimation

There are two types of background sources to the LED signature: those with $\not\!\!E_T$ due to one or more neutrinos produced in the event and those with $\not\!\!E_T$ from purely instrumental effects. We will consider W and Z production, QCD jets and cosmic ray separately. Contributions from other sources of background are small and therefore are ignored. This will give us a conservative result in our limit estimation.

5.5.1 W and Z Production

The $p\overline{p}$ collisions produce W and Z bosons. Such events can result in a jets + $\not\!\!E_T$ final state when the incoming quarks radiate one or more high energy quarks or gluons, and when one or more of the W or Z decay products goes undetected. Typical W and Z decay processes include:

1. $(W \rightarrow e\nu)$ + jets
2. $(W \rightarrow \mu\nu)$ + jets
3. $(W \rightarrow \tau\nu)$ (+ jets)
4. $(Z \rightarrow \nu\nu)$ + jets
5. $(Z \rightarrow ee)$ + jets
6. $(Z \rightarrow \mu\mu)$ + jets
7. $(Z \rightarrow \tau\tau)$ (+ jets)

The analysis requirements as described in Section 5.3 are applied to all background Monte Carlo samples. Each background is discussed in subsequent sections. All Monte Carlo samples are generated with PYTHIA 6.127 and processed in QSIM. Since information available by QSIM is very limited, many requirements are applied by cut efficiencies. We use published W/Z differential cross sections[61][62] for normalization of cases 1, 2, 4, 5, and 6 (10,000 events each) to data. The normalization factor is obtained from the ratio between the number of data events in the W/Z p_T range from 50 to 100 GeV and the number of MC events:

$$f_{normalization} = \frac{N_{data}}{N_{MC}}, \tag{5.1}$$

where N_{data} is the sum of the number of events in each W/Z p_T bin ranging from 50 to 100 GeV in References [61] and [62], N_{MC} is the number of MC events passing the same set of kinematic and fiducial cuts and after the correction of luminosity and electron identification efficiencies shown in References [61] and [62].We use cross section results from the DØ WZ cross section subgroup[63] for cases 3 and 7 (200,000 events each).

Our minimum requirements on the leading jet E_T and $\not{E}_T$ already suppress a large fraction of the background from W or Z production. And we will look at different survived W, Z processes below.

The examined W, Z processes that may have $\not{E}_T$ due to one or more neutrinos in the final state are:

$W \to \ell\nu$

W boson decays can be an important background since the neutrino can produce substantial $\not{E}_T$ in the event. The leading jet produced in initial or final state radiation may have substantial E_T; the other jets are typically soft. By our electron and muon vetoes, most of the ($W \to ev, \mu\nu$) + jets and $W \to \tau\nu$ ($\tau \to l\nu\nu$) + jets will be removed. We also have $W \to \tau\nu$ ($\tau \to hadrons$) (+ jets); the $W \to \tau\nu$ channel is our second largest W/Z background.

$Z \to \nu\nu$ and $Z \to \tau\tau$ (+ jets) with at least one $\tau \to l\nu\nu$

Clearly when the Z boson is heavily boosted, Z events could mimic the LED signal if $Z \to \nu\nu$ or if a lepton gets lost for the visible modes. The electron and muon vetoes also suppress the $Z \to \tau\tau$ (at least one $\tau \to l\nu\nu$). $Z \to \nu\nu$ events represent an irreducible background. As shown in Figures 5.6 to 5.17 (distributions have been normalized to data except the two-dimensional plots), $Z \to \nu\nu$ + jets channel has similar leading jet and $\not{E}_T$ distributions as the signal, although it exhibits a larger jet multiplicity than the signal. The leading jet E_T is balanced with $\not{E}_T$ for both $Z \to \nu\nu$ and signal.

Instrumental backgrounds arise from events where the $\not{E}_T$ is solely due to mismeasurements. Examples of possible sources are:

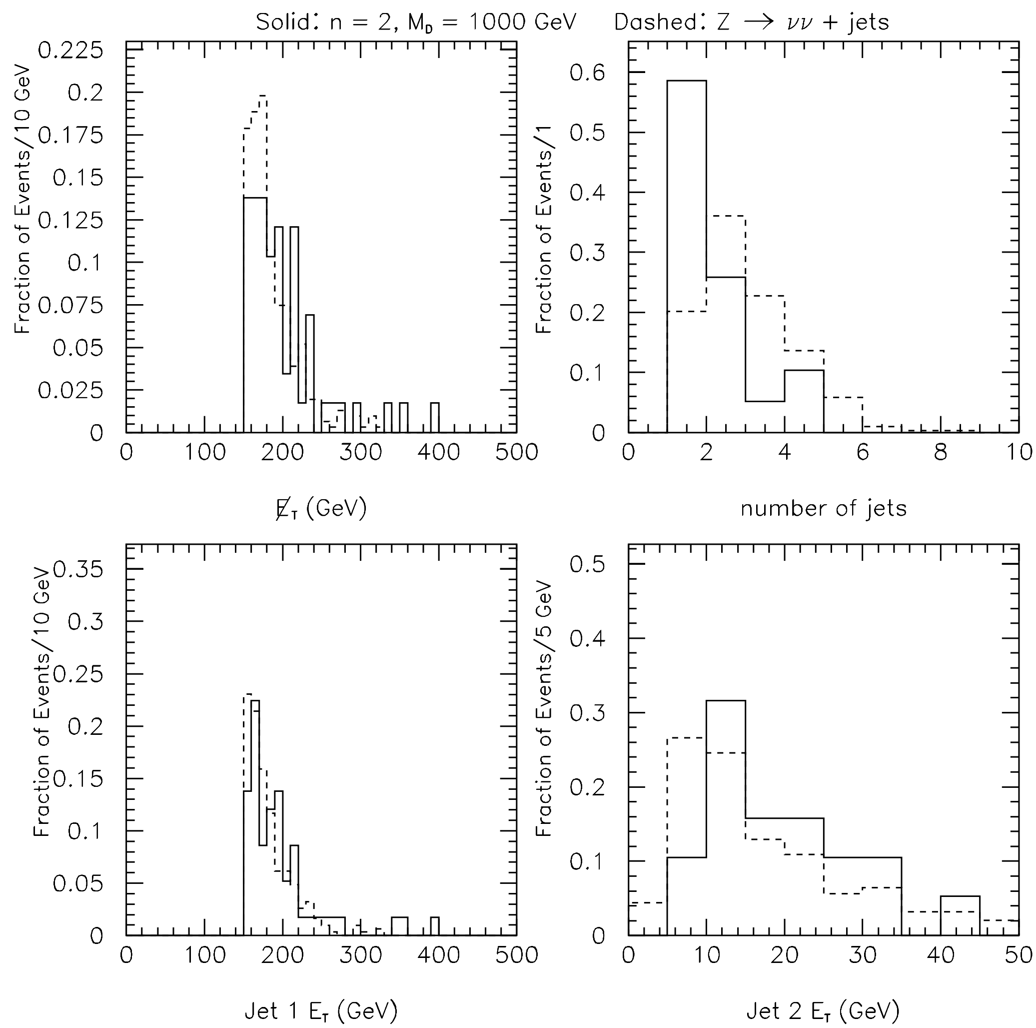

Figure 5.6. Comparison of the expected $Z \to \nu\nu$ + jets background to $n = 2$ and $M_D = 1000$ GeV LED production with the leading jet $\mathrm{E}_T/\not{E}_T > 150$ GeV, the second jet $\mathrm{E}_T < 50$ GeV, and $|\eta_d| \leq 1.0$. Top: $\not{E}_T$ (left) and number of jets (right). Bottom: Leading jet E_T (left) and second jet E_T (right).

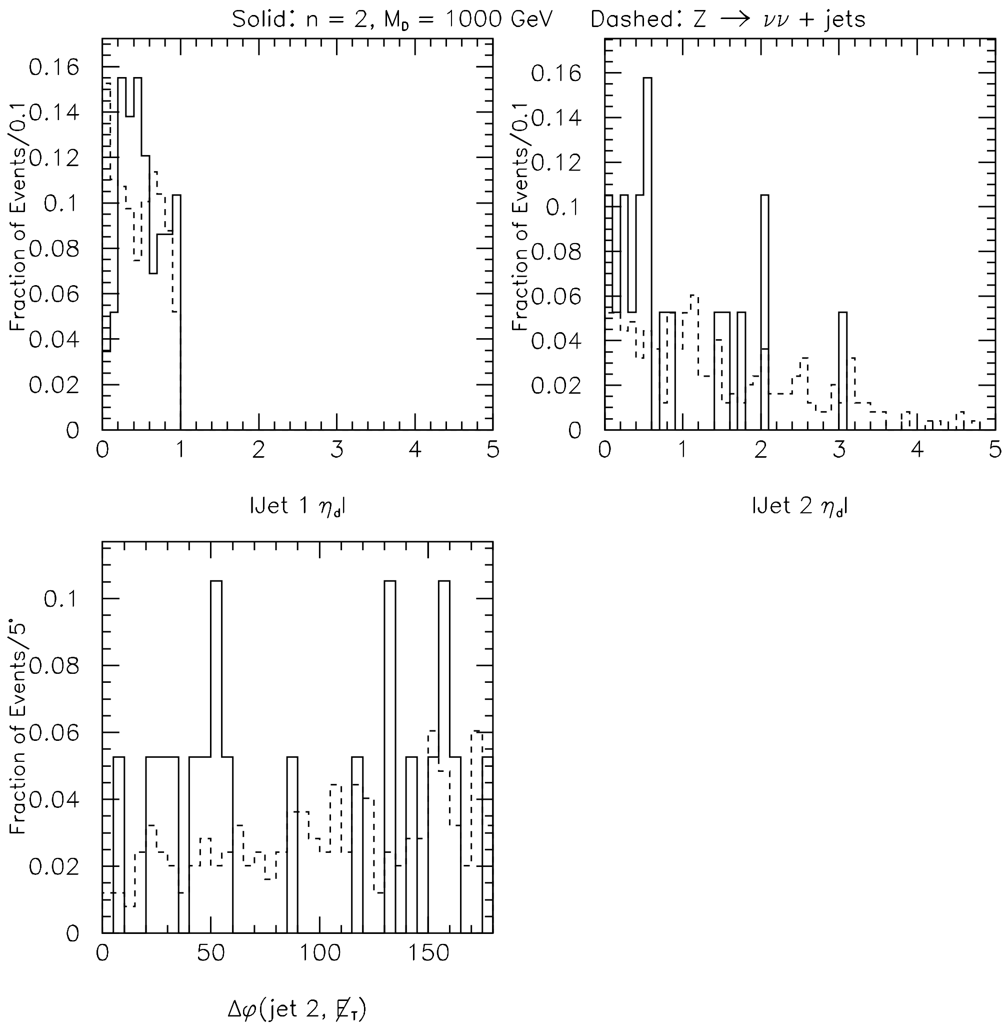

Figure 5.7. Comparison of the expected $Z \to \nu\nu$ + jets background to $n = 2$ and M_D = 1000 GeV LED production with the leading jet $\mathrm{E}_T/\not{E}_T > 150$ GeV, the second jet $\mathrm{E}_T < 50$ GeV, and $|\eta_d| \leq 1.0$. Top: Leading jet η_d (left) and second jet η_d (right). Bottom: $\Delta\varphi$(jet 2, $\not{E}_T$).

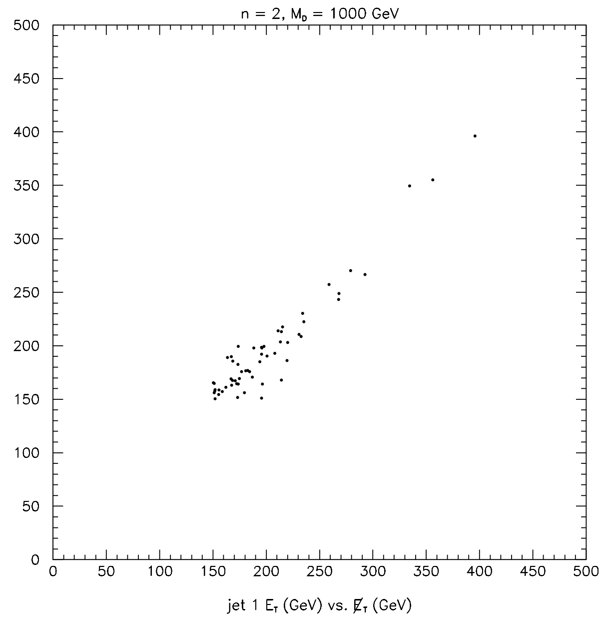

Figure 5.8. Leading jet E_T vs $\not{E}_T$ distribution for $n = 2$ and $M_D = 1000$ GeV LED production (not normalized to data) with the leading jet $\mathrm{E}_T/\not{E}_T > 150$ GeV, the second jet $\mathrm{E}_T < 50$ GeV, and $|\eta_d| \leq 1.0$.

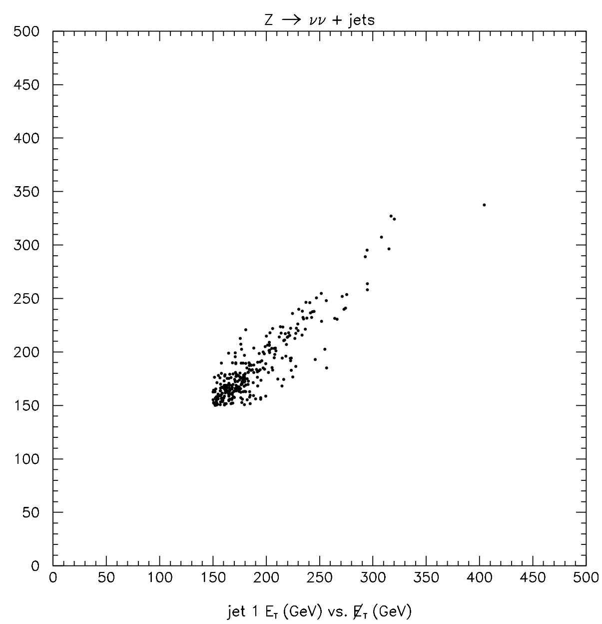

Figure 5.9. Leading jet E_T vs $\not{E}_T$ distribution for $Z \to \nu\nu$ + jets background (not normalized to data) with the leading jet $\mathrm{E}_T/\not{E}_T > 150$ GeV, the second jet $\mathrm{E}_T <$ 50 GeV, and $|\eta_d| \leq 1.0$.

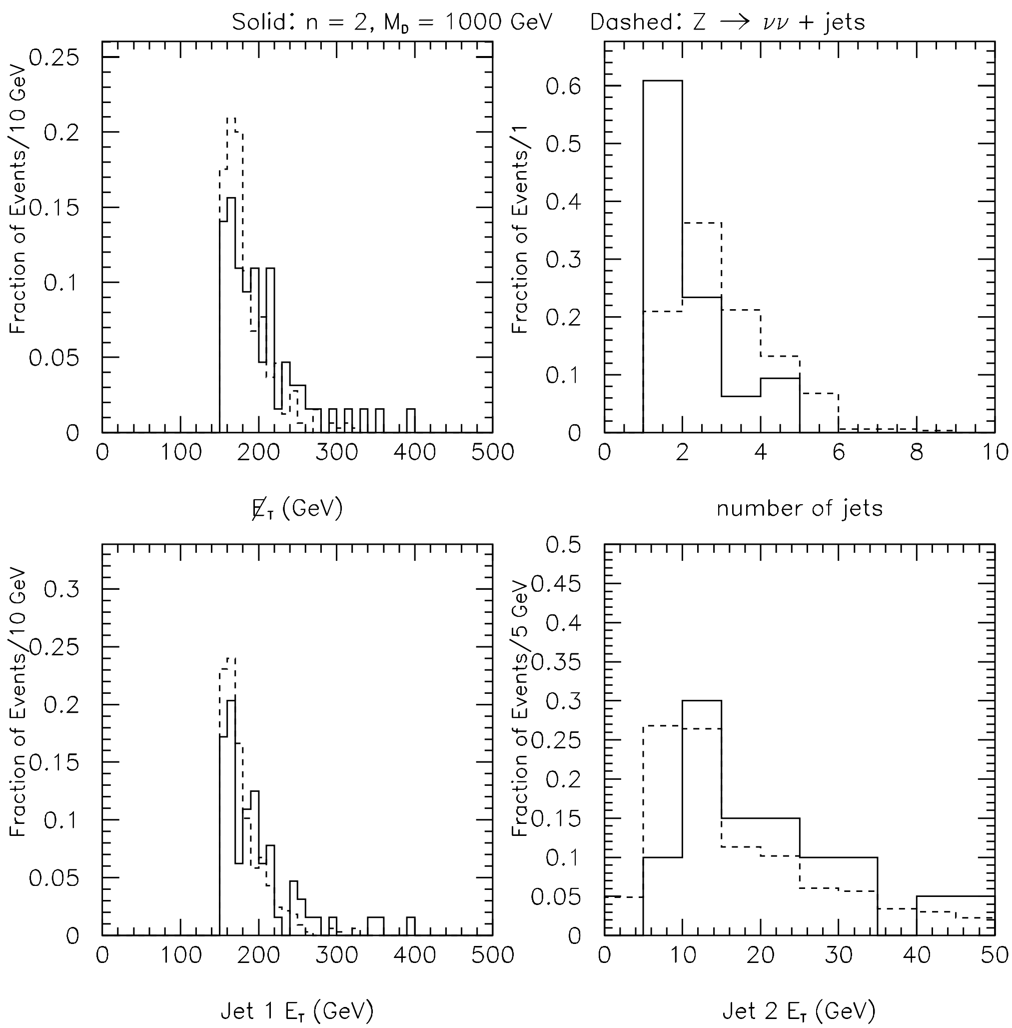

Figure 5.10. Comparison of the expected $Z \to \nu\nu$ + jets background to $n = 2$ and $M_D = 1000$ GeV LED production with the leading jet $\mathrm{E}_T/\not{E}_T > 150$ GeV, the second jet $\mathrm{E}_T < 50$ GeV, and $|\eta_d| < 1.1$ or $1.5 < |\eta_d| \leq 2.5$. Top: $\not{E}_T$ (left) and number of jets (right). Bottom: Leading jet E_T (left) and second jet E_T (right).

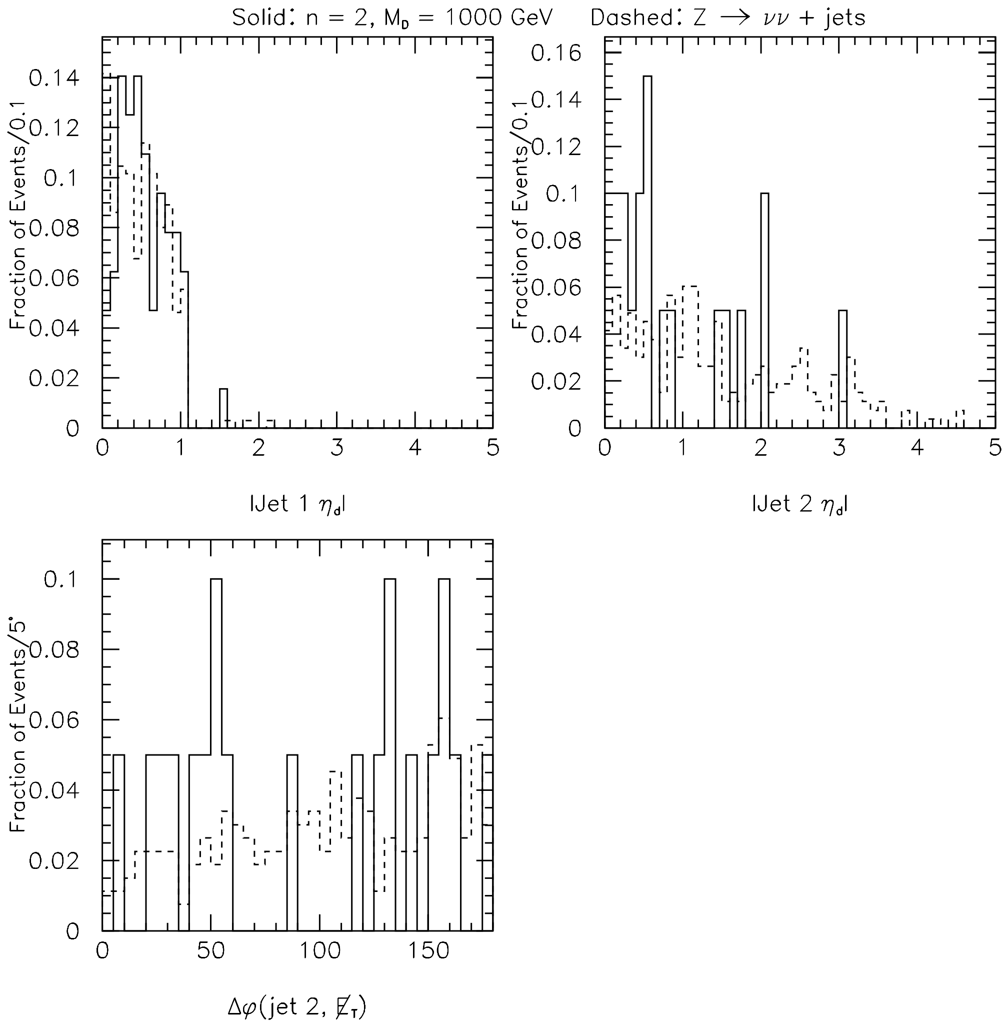

Figure 5.11. Comparison of the expected $Z \rightarrow \nu\nu$ + jets background to $n = 2$ and $M_D = 1000$ GeV LED production with the leading jet $\mathrm{E}_T/\not{E}_T > 150$ GeV, the second jet $\mathrm{E}_T < 50$ GeV, and $|\eta_d| < 1.1$ or $1.5 < |\eta_d| \leq 2.5$. Top: Leading jet η_d (left) and second jet η_d (right). Bottom: $\Delta\varphi(\text{jet } 2,\ \not{E}_T)$.

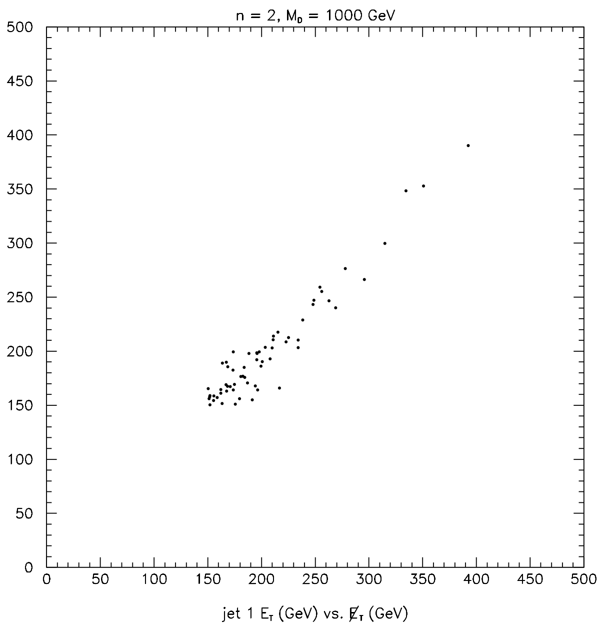

Figure 5.12. Leading jet E_T vs $\not\!\!E_T$ distribution for $n = 2$ and $M_D = 1000$ GeV LED production (not normalized to data) with the leading jet $\mathrm{E}_T/\not\!\!E_T > 150$ GeV, the second jet $\mathrm{E}_T < 50$ GeV, and $|\eta_d| < 1.1$ or $1.5 < |\eta_d| \leq 2.5$.

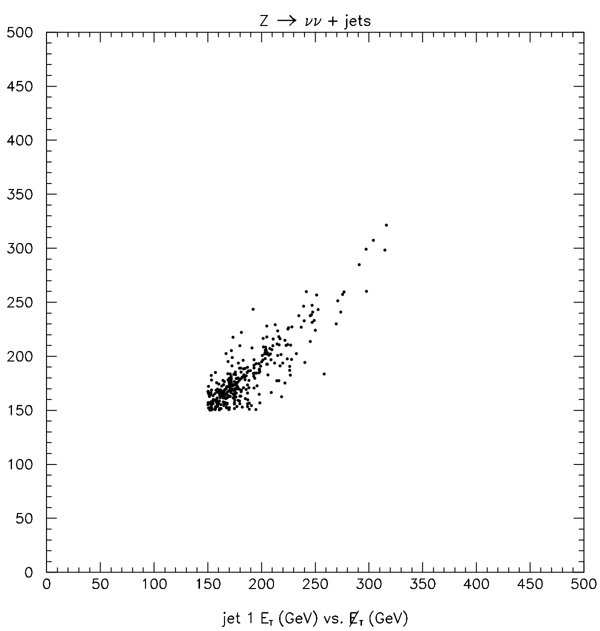

Figure 5.13. Leading jet E_T vs $\not\!\!E_T$ distribution for $Z \to \nu\nu$ + jets background (not normalized to data) with the leading jet $\mathrm{E}_T/\not\!\!E_T > 150$ GeV, the second jet $\mathrm{E}_T <$ 50 GeV, and $|\eta_d| < 1.1$ or $1.5 < |\eta_d| \leq 2.5$.

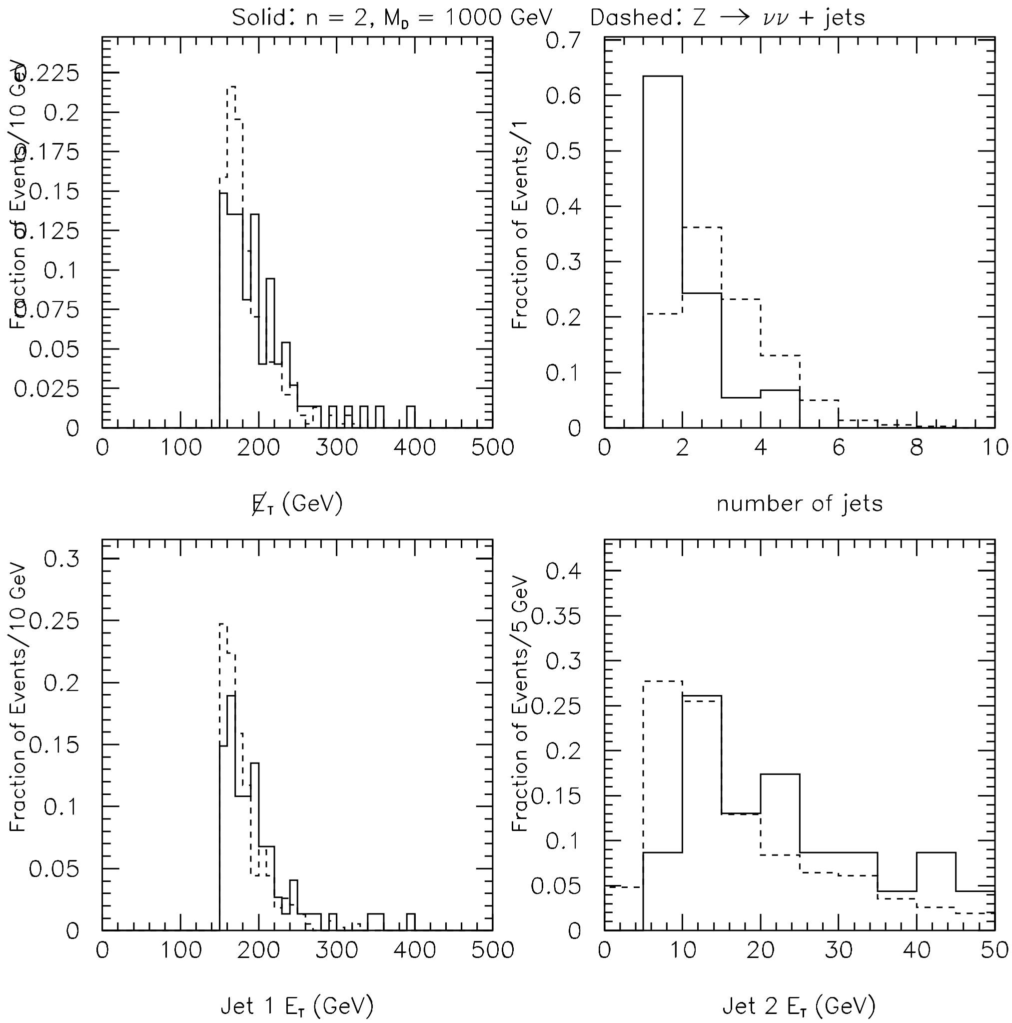

Figure 5.14. Comparison of the expected $Z \to \nu\nu$ + jets background to $n = 2$ and $M_D = 1000$ GeV LED production with the leading jet $E_T/\not\!E_T > 150$ GeV, the second jet $E_T < 50$ GeV, and $|\eta_d| \leq 2.5$. Top: $\not\!E_T$ (left) and number of jets (right). Bottom: Leading jet E_T (left) and second jet E_T (right).

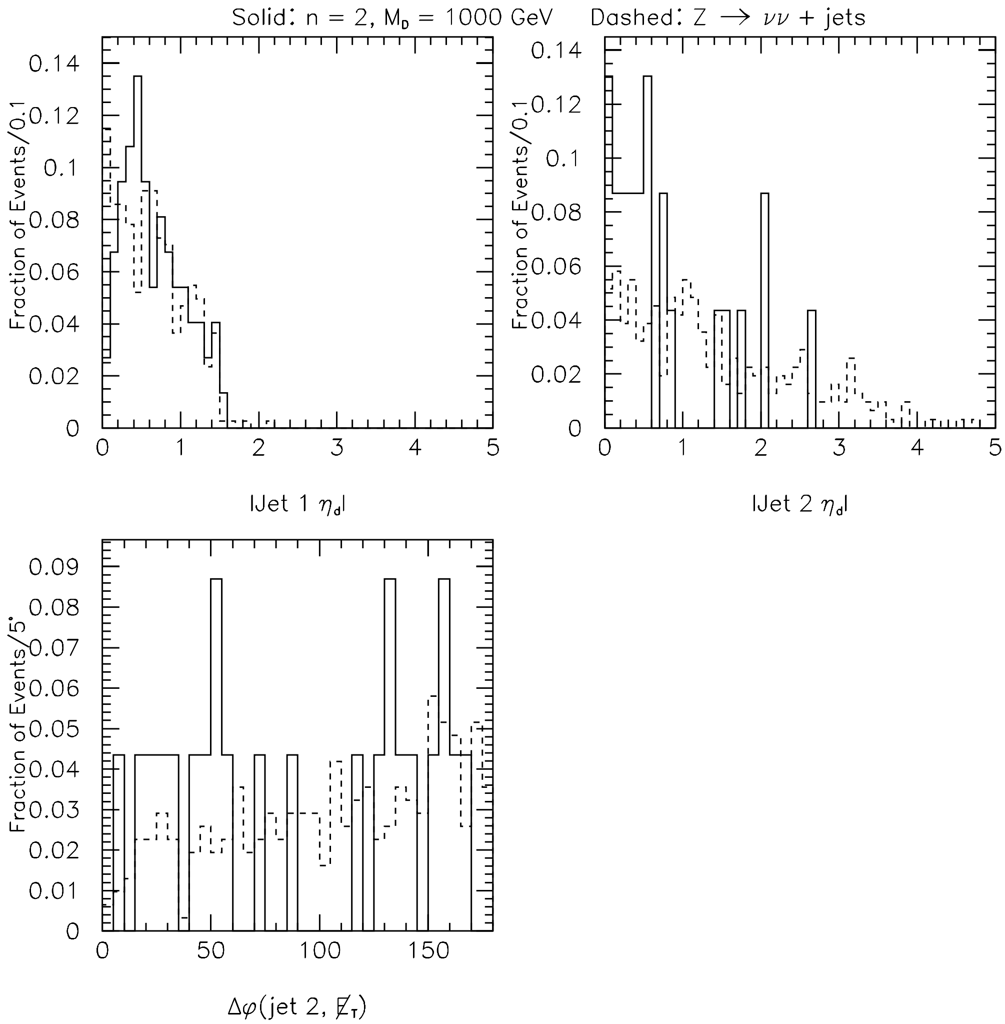

Figure 5.15. Comparison of the expected $Z \to \nu\nu$ + jets background to $n = 2$ and $M_D = 1000$ GeV LED production with the leading jet $E_T/\not\!\!E_T > 150$ GeV, the second jet $E_T < 50$ GeV, and $|\eta_d| \leq 2.5$. Top: Leading jet η_d (left) and second jet η_d (right). Bottom: $\Delta\varphi$(jet 2, $\not\!\!E_T$).

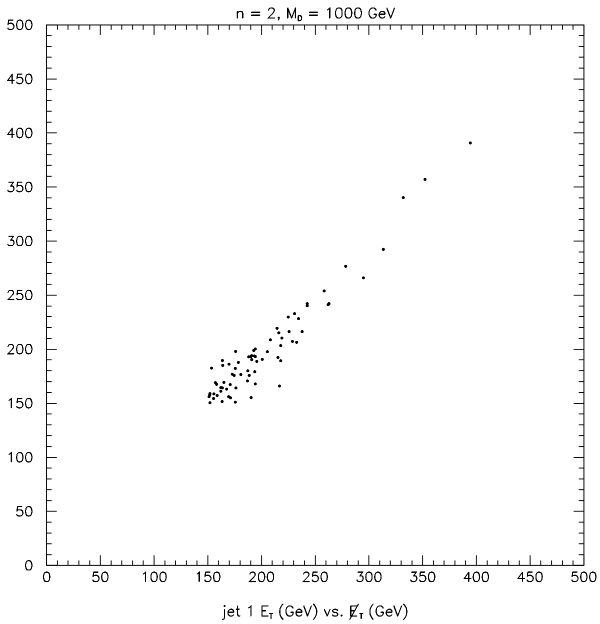

Figure 5.16. Leading jet E_T vs $\not\!\!E_T$ distribution for $n = 2$ and $M_D = 1000$ GeV LED production (not normalized to data) with the leading jet $E_T/\not\!\!E_T > 150$ GeV, the second jet $E_T < 50$ GeV, and $|\eta_d| \leq 2.5$.

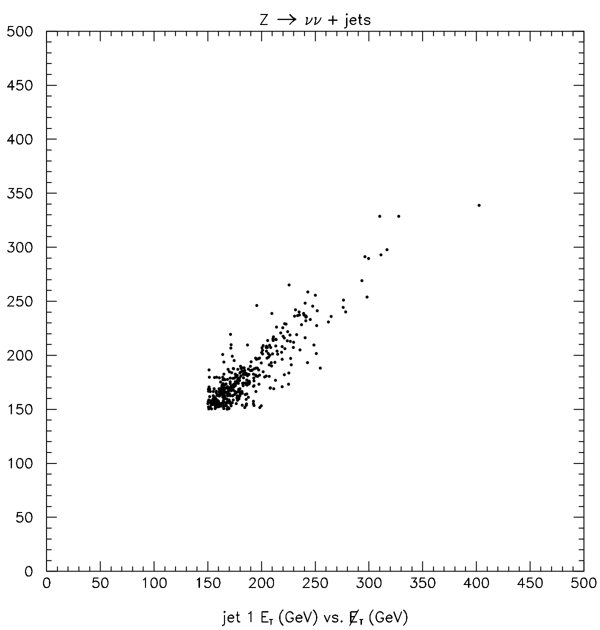

Figure 5.17. Leading jet E_T vs $\not\!\!E_T$ distribution for $Z \rightarrow \nu\nu$ + jets background (not normalized to data) with the leading jet $E_T/\not\!\!E_T > 150$ GeV, the second jet $E_T < 50$ GeV, and $|\eta_d| \leq 2.5$.

$Z \to ee$ + jets, $Z \to \mu\mu$ + jets events where both leptons are lost or mismeasured and $Z \to \tau\tau$ (+ jets) with no $\tau \to l\nu\nu$ but where some jets are lost or mismeasured.

The background contribution from these sources is small.

The number of expected events from W and Z (+ jets) production is calculated using:

$$N = L \times \sigma \times A, \tag{5.2}$$

where L is the luminosity (78.8 $\pm$ 3.9) pb^{-1} after removing the bad runs, σ is the cross section of the process, and A is the acceptance of our cuts as shown in Section 5.3. The error we take for L is 5%, which is larger than the luminosity-weighted average error for Run I (4.41%)[59] since when we process the tapes to get larger size data files (STA/DST) event by event and some of the event files may not be available due to tape problems, etc. Therefore, the luminosity of the data set needs to be corrected, since with different cuts, the missing events are different. 5% is a conservative estimation of such effect. To obtain the error on the cross section, we vary the parton distribution function in PYTHIA to get the difference in cross section. Then we add in quadrature the error of the cross section normalization factor except for ($W \to \tau\nu$) (+ jets) and ($Z \to \tau\tau$) (+ jets). For those two cases, we use the results from the DØ WZ cross section subgroup[63]. All the efficiency errors go into the acceptance error by adding them in quadrature with the error from the jet energy scale. The error from the jet energy scale is the main source of the acceptance error, for example, an error of 19.3% from the jet energy scale contributes into the background estimation of $Z \to \nu\nu$ + jets channel with a central leading jet. The jet energy scale error is determined by calculating the change of acceptance due to the change of E_T^j by one standard deviation of its resolution from GEANT samples of different processes:

$$E_T^j(new) = (1 \pm s) \times E_T^j(nominal) \pm c, \tag{5.3}$$

TABLE 5.7. EXPECTED NUMBER OF EVENTS FROM EACH W OR Z BACKGROUND WITH THE LEADING JET $\mathrm{E}_T/\not\!\!E_T > 150$ GeV, THE SECOND JET $\mathrm{E}_T < 50$ GeV, AND $|\eta_d| \leq 1.0$.

Background	N	σ (pb)	$A \times 10^{-4}$
$Z \to \nu\nu+$ jets	21.0 ± 5.1	8.37 ± 0.90	318.0 ± 67.3
$Z \to ee+$ jets	< 0.0111	1.41 ± 0.15	< 1.0
$Z \to \mu\mu+$ jets	0.0111 ± 0.0115	1.40 ± 0.16	1.00 ± 1.03
$Z \to \tau\tau$ (+ jets)	< 0.0872	221.3 ± 11.2	< 0.05
$W \to e\nu+$ jets	3.14 ± 0.71	6.54 ± 1.06	61.0 ± 9.2
$W \to \mu\nu+$ jets	0.821 ± 0.331	6.51 ± 1.06	16.0 ± 5.8
$W \to \tau\nu$ (+ jets)	5.25 ± 2.32	2220 ± 168	0.300 ± 0.130

TABLE 5.8. EXPECTED NUMBER OF EVENTS FROM EACH W OR Z BACKGROUND WITH THE LEADING JET $\mathrm{E}_T/\not\!\!E_T > 150$ GeV, THE SECOND JET $\mathrm{E}_T < 50$ GeV, AND $|\eta_d| < 1.1$ OR $1.5 < |\eta_d| \leq 2.5$.

Background	N	σ (pb)	$A \times 10^{-4}$
$Z \to \nu\nu+$ jets	22.2 ± 5.6	8.37 ± 0.90	336.0 ± 75.1
$Z \to ee+$ jets	< 0.0111	1.41 ± 0.15	< 1.0
$Z \to \mu\mu+$ jets	0.0111 ± 0.0115	1.40 ± 0.16	1.00 ± 1.03
$Z \to \tau\tau$ (+ jets)	< 0.0872	221.3 ± 11.2	< 0.05
$W \to e\nu+$ jets	3.56 ± 0.89	6.54 ± 1.06	69.0 ± 12.8
$W \to \mu\nu+$ jets	0.872 ± 0.348	6.51 ± 1.06	17.0 ± 6.1
$W \to \tau\nu$ (+ jets)	5.25 ± 2.32	2220 ± 168	0.300 ± 0.130

where $s = 2.5\%$ and $c = 0.5$ GeV and s is raised to 3.5% for jets within $0.8 \leq |\eta_d^j| \leq 1.4$[59]. The W and Z background estimates are shown in Table 5.7 to 5.9 and the production cross section differences between the τ decay channels and other decay channels of W and Z come from different initial energies that these MC samples are generated at (Section 5.2).

5.5.2 QCD Multijet Production and Cosmic Ray

Other sources of the instrumental background come from the multijet production and cosmic ray. Light quark and gluon production are the most common processes

TABLE 5.9. EXPECTED NUMBER OF EVENTS FROM EACH W OR Z BACKGROUND WITH THE LEADING JET $\mathrm{E}_T/\not{E}_T > 150$ GeV, THE SECOND JET $\mathrm{E}_T < 50$ GeV, AND $|\eta_d| \leq 2.5$.

Background	N	σ (pb)	$A \times 10^{-4}$
$Z \to \nu\nu+$ jets	26.3 ± 6.4	8.37 ± 0.90	399.0 ± 84.1
$Z \to ee+$ jets	< 0.0111	1.41 ± 0.15	< 1.0
$Z \to \mu\mu+$ jets	0.0111 ± 0.0115	1.40 ± 0.16	1.00 ± 1.03
$Z \to \tau\tau$ (+ jets)	< 0.0872	221.3 ± 11.2	< 0.05
$W \to e\nu+$ jets	3.82 ± 1.04	6.54 ± 1.06	74.0 ± 15.8
$W \to \mu\nu+$ jets	0.924 ± 0.365	6.51 ± 1.06	18.0 ± 6.4
$W \to \tau\nu$ (+ jets)	6.12 ± 2.56	2220 ± 168	0.350 ± 0.143

at the Tevatron. These processes have no intrinsic $\not{E}_T$, but if mismeasurement occurs in one or more jets in an event, it can cause the event to pass our $\not{E}_T$ requirement. The primary vertex confirmation requirement described in Section 5.3.11 and the $\Delta\phi_{jet(2)-\not{E}_T}$ cut described in Section 5.3.9 eliminate much of the quark and gluon events with vertex and jet energy measurement errors. Monte Carlo events assume measurements with normal detector resolutions, while our sample contains pathological events outside of these resolutions. Thus the data are used to determine how many of these events remain. The primary vertex confirmation cut also acts as a cosmic ray veto. So it will give us an estimation of the remaining cosmics ray events.

We use the events that fail the primary vertex confirmation cut but pass $\Delta\phi_{jet(2)-\not{E}_T}$ cut as our multijet with measurement errors and cosmic ray sample (Q). In the Q sample, the deviation between the leading jet vertex and the reconstructed vertex (Δz) is larger than 10 cm. We use the events that fail $\Delta\phi_{jet(2)-\not{E}_T}$ cut (Section 5.3.9) as our normalization samples (N_1 and N_2) to normalize the Q sample to the data. This means that the normalization samples satisfy $|\Delta\phi_{jet(2)-\not{E}_T}| \leq 15°$ if the second jet $E_T \geq 15$ GeV and $|\eta_d| \leq 2.5$ which is another multijet-dominated region and yet not biased against cosmic rays. The N_1 sample contains events which pass the primary vertex confirmation cut while the N_2 sample contains the events that fail the primary vertex confirmation cut. A lower threshold of 20 GeV on second jet energy is applied to the normalization samples in order to minimize the LED signal contribution. After subtracting the expected W, Z background from the Q, N_1 and N_2 samples, we have:

QCD/cosmics in data: D = Q $\times$ N_1 / N_2,

where QCD/cosmics sample (Q): failed vertex cut but passed $\Delta\phi_{jet(2)-\not{E}_T}$ cut

QCD/cosmics Normalization samples: failed $\Delta\phi_{jet(2)-\not{E}_T}$ cut, with E(2nd jet) $\geq$ 20 GeV

N_1: passed vertex cut

N_2: failed vertex cut

The signal contribution in the Q sample cannot be ignored either, but as we will show in Section 5.6.3 and Chapter 6, the difference between the limit calculation with and without considering the signal contribution in the Q sample is very small. So when calculating the QCD/cosmics background, we ignore the signal contribution in the Q sample. Since the statistical error is large for the QCD/cosmics background estimation, we also ignore the systematic error. When loosening the leading jet E_T and $\not{E}_T$ cuts to 115 GeV and tightening the second jet E_T cut to 40 GeV in order to keep roughly the same E_T ratio between leading jet and second jet, as shown in Table 5.10, the total estimation is consistent with the number of observed events. Tables 5.11 to 5.13 show the number of events in our multijet sample and the normalization factor and the expected number of multijet events in the jets + $\not{E}_T$ data set.

TABLE 5.10. EXPECTED AND OBSERVED NUMBER OF EVENTS WITH THE LEADING JET $E_T/\not\!\!E_T > 115$ GeV, THE SECOND JET $E_T < 40$ GeV AND $|\eta_d| \leq 2.5$.

Event Sample	Number of Events
Multijet/cosmics	52.2 ± 18.3
W and Z	138.8 ± 23.8
Total background	190.9 ± 30.0
Data	198

TABLE 5.11. EXPECTED NUMBER OF MULTIJET/COSMICS EVENTS IN THE DATA SAMPLE WITH THE LEADING JET $E_T/\not\!\!E_T > 150$ GeV, THE SECOND JET $E_T < 50$ GeV, AND $|\eta_d| \leq 1.0$.

Q	N_1/N_2	Expected number of multijet/cosmics events
26.1 ± 5.6	0.299 ± 0.266	7.79 ± 7.14

5.5.3 Background Summary

The number of background estimates from different sources are summarized in Table 5.14 to 5.16. For total W and Z background of the seven decay topologies (Section 5.5.1), the energy scale and luminosity errors are added linearly. All other errors are added in quadrature.

Figures 5.18 to 5.20 compare the $\not\!\!E_T$ distribution of data to total background and a "signal point" with $n = 2$ and $M_D = 1000$ GeV + total background. As we can see, the distributions for data and background are consistent. If interested, the event display for the candidate event with the highest $\not\!\!E_T$ can be found in Appendix A.

TABLE 5.12. EXPECTED NUMBER OF MULTIJET/COSMICS EVENTS IN THE DATA SAMPLE WITH THE LEADING JET $E_T/\not\!\!E_T > 150$ GeV, SECOND JET $E_T < 50$ GeV, AND $|\eta_d| < 1.1$ OR $1.5 < |\eta_d| \leq 2.5$.

Q	N_1/N_2	Expected number of multijet/cosmics events
26.2 ± 5.6	0.299 ± 0.266	7.82 ± 7.16

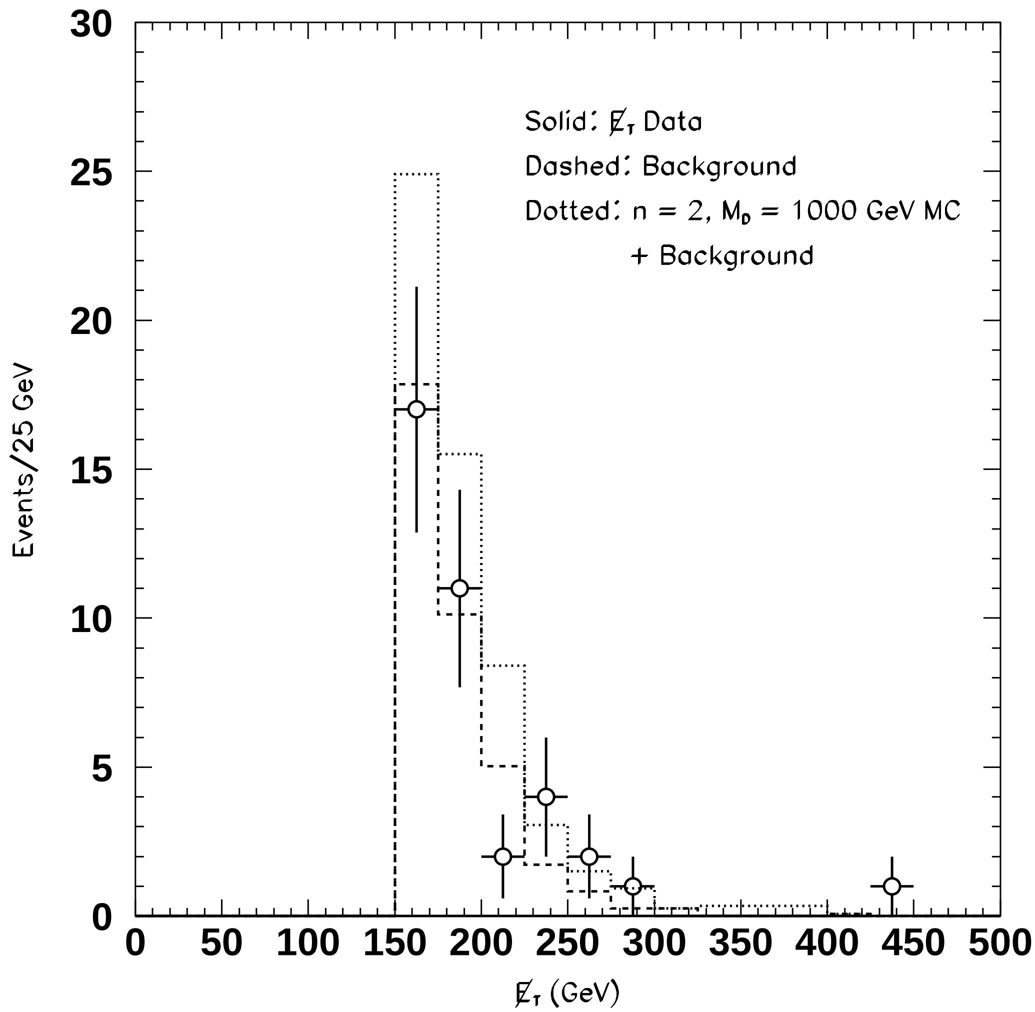

Figure 5.18. Comparison of $\not{E}_T$ distribution of jets + $\not{E}_T$ data (solid) to expected total background (dashed) and $n = 2$ and $M_D = 1000$ GeV LED production + total background (dotted) with the leading jet E_T /$\not{E}_T$ > 150 GeV, the second jet E_T < 50 GeV, and $|\eta_d| \leq 1.0$.

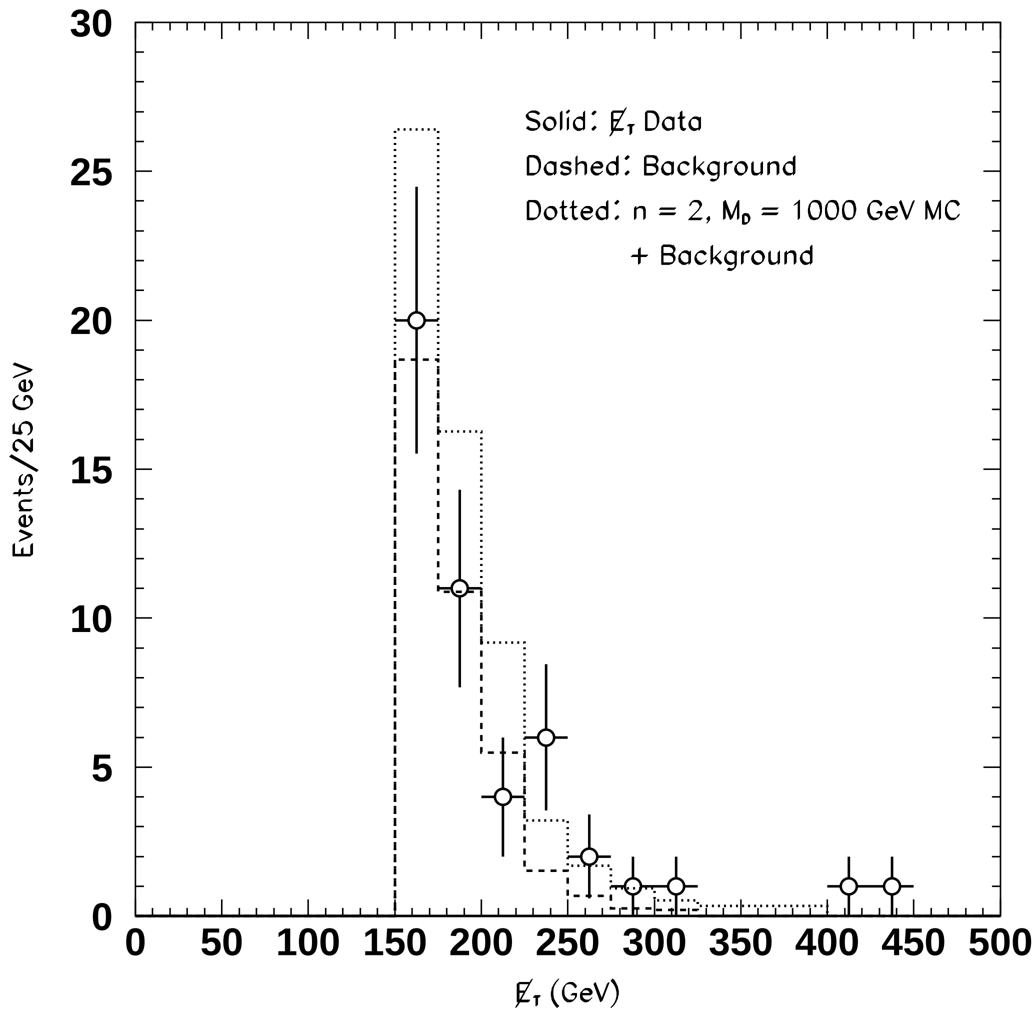

Figure 5.19. Comparison of $\not{E}_T$ distribution of jets + $\not{E}_T$ data (solid) to expected total background (dashed) and $n = 2$ and $M_D = 1000$ GeV LED production + total background (dotted) with the leading jet $E_T/\not{E}_T > 150$ GeV, the second jet $E_T <$ 50 GeV, and $|\eta_d| < 1.1$ or $1.5 < |\eta_d| \leq 2.5$.

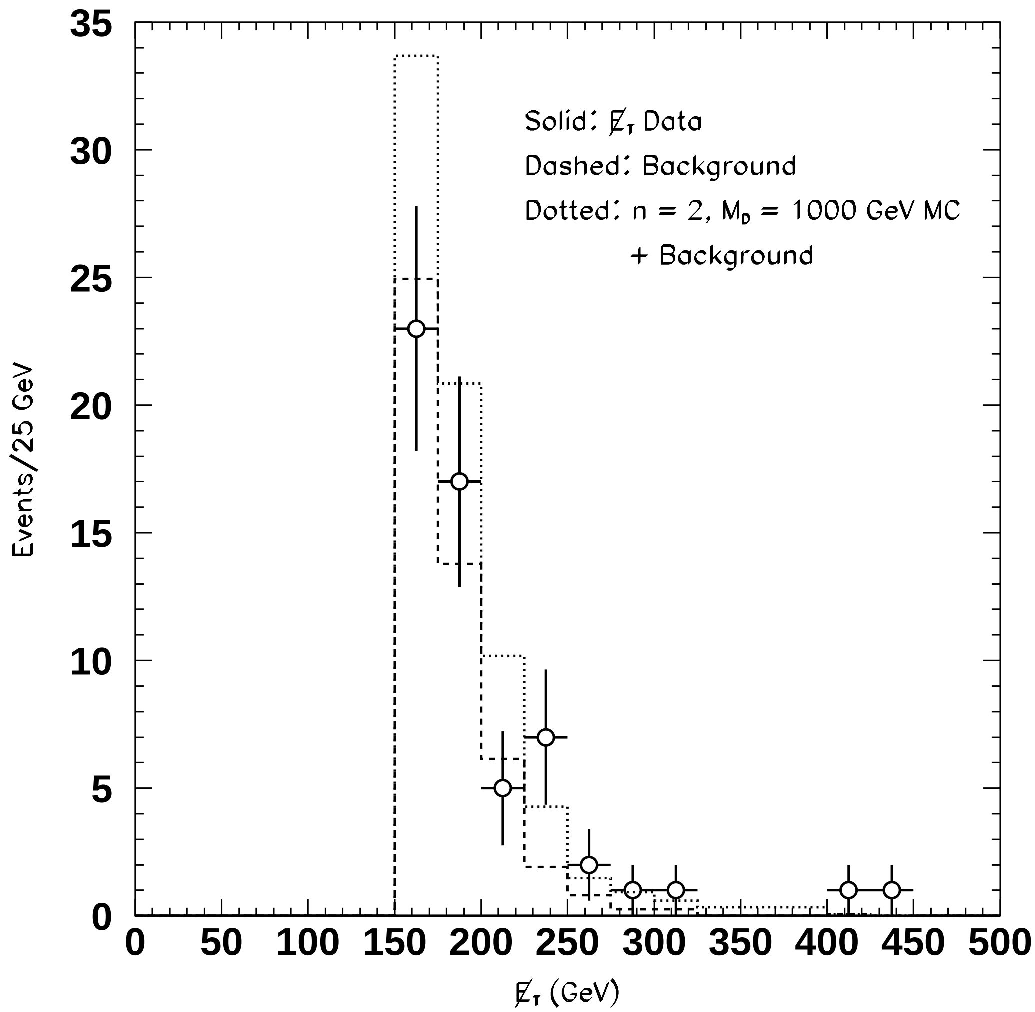

Figure 5.20. Comparison of $\not{E}_T$ distribution of jets + $\not{E}_T$ data (solid) to expected total background (dashed) and $n = 2$ and $M_D = 1000$ GeV LED production + total background (dotted) with the leading jet $\mathrm{E}_T/\not{E}_T > 150$ GeV, the second jet $\mathrm{E}_T <$ 50 GeV, and $|\eta_d| \leq 2.5$.

TABLE 5.13. EXPECTED NUMBER OF MULTIJET/COSMICS EVENTS IN THE DATA SAMPLE WITH THE LEADING JET $E_T/\not{E}_T > 150$ GeV, SECOND JET $E_T < 50$ GeV, AND $|\eta_d| \leq 2.5$.

Q	N_1/N_2	Expected number of multijet/cosmics events
27.0 ± 5.5	0.461 ± 0.348	12.5 ± 9.8

TABLE 5.14. ESTIMATED TOTAL BACKGROUND FOR THE LEADING JET $E_T/\not{E}_T > 150$ GeV, THE SECOND JET $E_T < 50$ GeV, AND $|\eta_d| \leq 1.0$ IN JETS + $\not{E}_T$ DATA.

$N_{W \text{ and } Z \text{ total}}$	30.2 ± 6.4
$N_{\text{QCD/cosmics}}$	7.79 ± 7.14
$N_{\text{Background Total}}$	38.0 ± 9.6
Events in data:	38

5.6 Signal Analysis

5.6.1 Signal Monte Carlo

We use the subroutine by theorists J. Lykken and K. Matchev[64] as the external process with the PYTHIA 6.150 generator for all of our LED Monte Carlo samples. We generate 1000 events for each number of extra dimensions (n) ranging from 2 to 7 with the fundamental mass scale (M_D) ranging from 600 GeV to 1400 GeV (in 200 GeV intervals) except for $n = 7$. For $n = 7$, M_D ranges from 600 GeV to 1200 GeV (in 200 GeV intervals).

TABLE 5.15. ESTIMATED TOTAL BACKGROUND FOR THE LEADING JET $E_T/\not{E}_T > 150$ GeV, THE SECOND JET $E_T < 50$ GeV, AND $|\eta_d| < 1.1$ OR $1.5 < |\eta_d| \leq 2.5$ IN JETS + $\not{E}_T$ DATA.

$N_{W \text{ and } Z \text{ total}}$	31.8 ± 7.2
$N_{\text{QCD/cosmics}}$	7.82 ± 7.16
$N_{\text{Background Total}}$	39.7 ± 10.1
Events in data:	47

TABLE 5.16. ESTIMATED TOTAL BACKGROUND FOR THE LEADING JET $E_T/\not{E}_T > 150$ GeV, THE SECOND JET $E_T < 50$ GeV, AND $|\eta_d| \leq 2.5$ IN JETS + $\not{E}_T$ DATA.

$N_{W \text{ and } Z \text{ total}}$	37.2 ± 8.3
$N_{\text{QCD/cosmics}}$	12.5 ± 9.8
$N_{\text{Background Total}}$	49.7 ± 12.8
Events in data:	58

The number of signal events expected is given by Equation (5.2), where L is the luminosity (78.8 ± 3.9) pb^{-1} after removing the bad runs, σ is the signal production cross section, and A is the signal acceptance of our cuts (Section 5.3). As with the W and Z background estimation, we vary the parton distribution function in PYTHIA to get the variation in cross section for the systematic error. All the efficiency errors go into the acceptance error in quadrature with the error from the jet energy scale. The error of the jet energy scale is calculated using Equation (5.3) from the GEANT samples with $n = 2$ with M_D ranging from 600 GeV to 1400 GeV (in 200 GeV intervals). The reason that we do not calculate the error from the jet energy scale point by point is that it is not practical to have GEANT samples for all points and as we can see in the optimization below, the signal behavior is very much the same with different n. An example of the error breakdown for the signal point with $n = 2$ and $M_D = 1000$ GeV is: the statistical error of the acceptance from the MC sample, 12.7%; the systematic error of the cross section, 5.5%; the systematic error from the jet energy scale, 11.9%; and the total error from the efficiencies and correction factor, 6.6%.

5.6.2 Event Selection Optimization

In order to maximize the statistical significance of the excesses we would observe in the presence of the LED process, optimizations for some of the event selection cuts are studied: the primary vertex confirmation cut (Section 5.3.11), the $\Delta\phi_{jet(2)-\not{E}_T}$ (Section 5.3.9) cut and the kinematic cuts. The signal significance being used is:

$$\overline{s} = \frac{s}{\sqrt{b + \Delta b^2}}, \tag{5.4}$$

where s is the number of LED events expected ("signal"), b is the number of background events expected, and Δb is the error of the estimated background.

5.6.2.1 Optimization for Primary Vertex Confirmation Cut

We calculate the signal significance of the primary vertex confirmation cut with the distance between leading jet vertex and the reconstructed vertex $\Delta z \leq$ 5, 10, 15, 20, and 25 cm for all the signal points. As shown in Figure 5.21 (for signal point with $n = 2$ only) and Figure 5.22 (for all signal points), the signal significance for $\Delta z \leq 10$ cm is the highest for all signal points.

5.6.2.2 Optimization for Detector Eta Cut on the Leading Jet

We calculate the signal significance for the detector Eta cut on the leading jet with $|\eta_d| \leq$ 1.0, 1.5, 2.5 (including and excluding the intercryostat region (ICR): $1.1 \leq |\eta_d| \leq 1.5$), and 3.5 (including and excluding ICR: $1.1 \leq |\eta_d| \leq 1.5$) for all the signal points. As shown in Figure 5.23 (for signal point with $n = 2$ only) and Figure 5.24 (for all signal points), the signal significance for η_d excluding the ICR is higher than

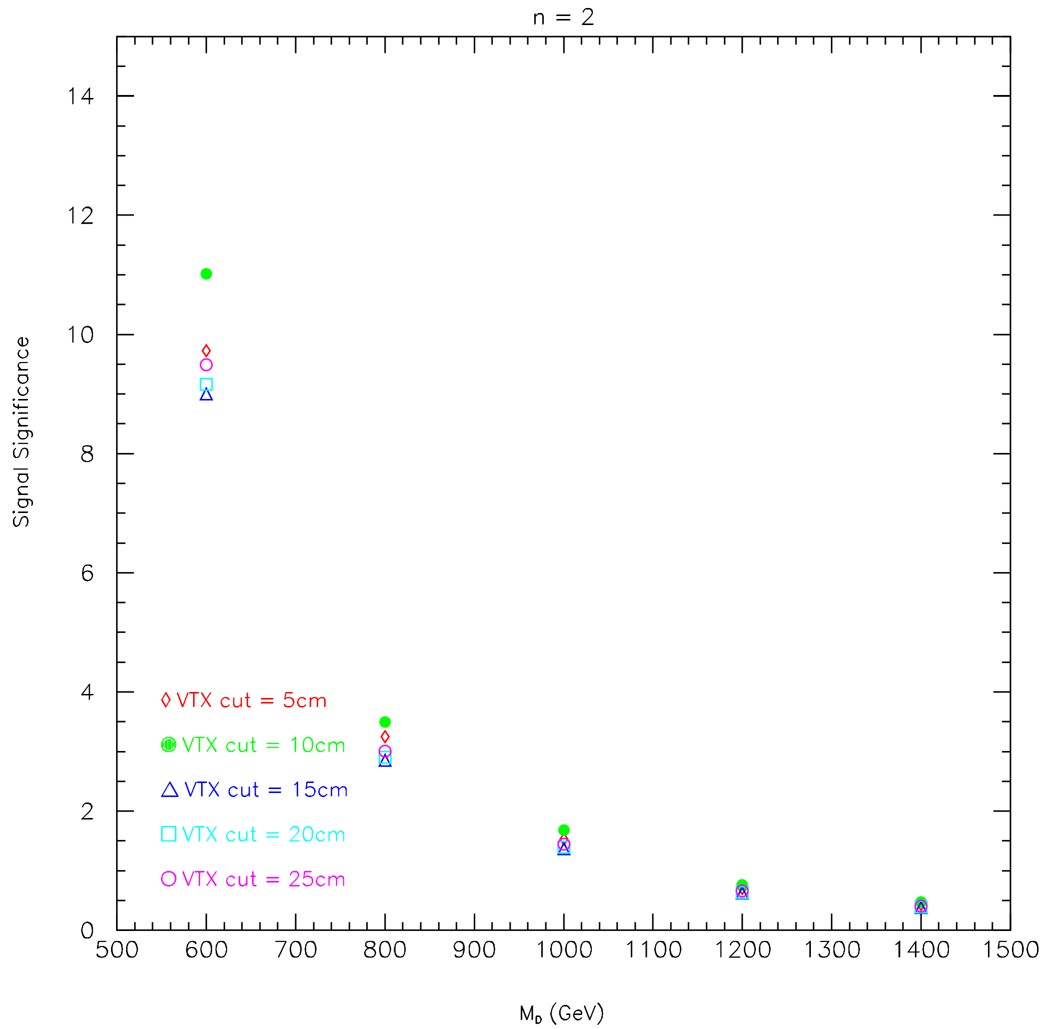

Figure 5.21. Signal significance of the primary vertex confirmation cut for signal points with $n = 2$ and with the leading jet $\mathrm{E}_T/\not{E}_T > 150$ GeV, the second jet $\mathrm{E}_T < 50$ GeV, and $|\eta_d| \leq 2.5$.

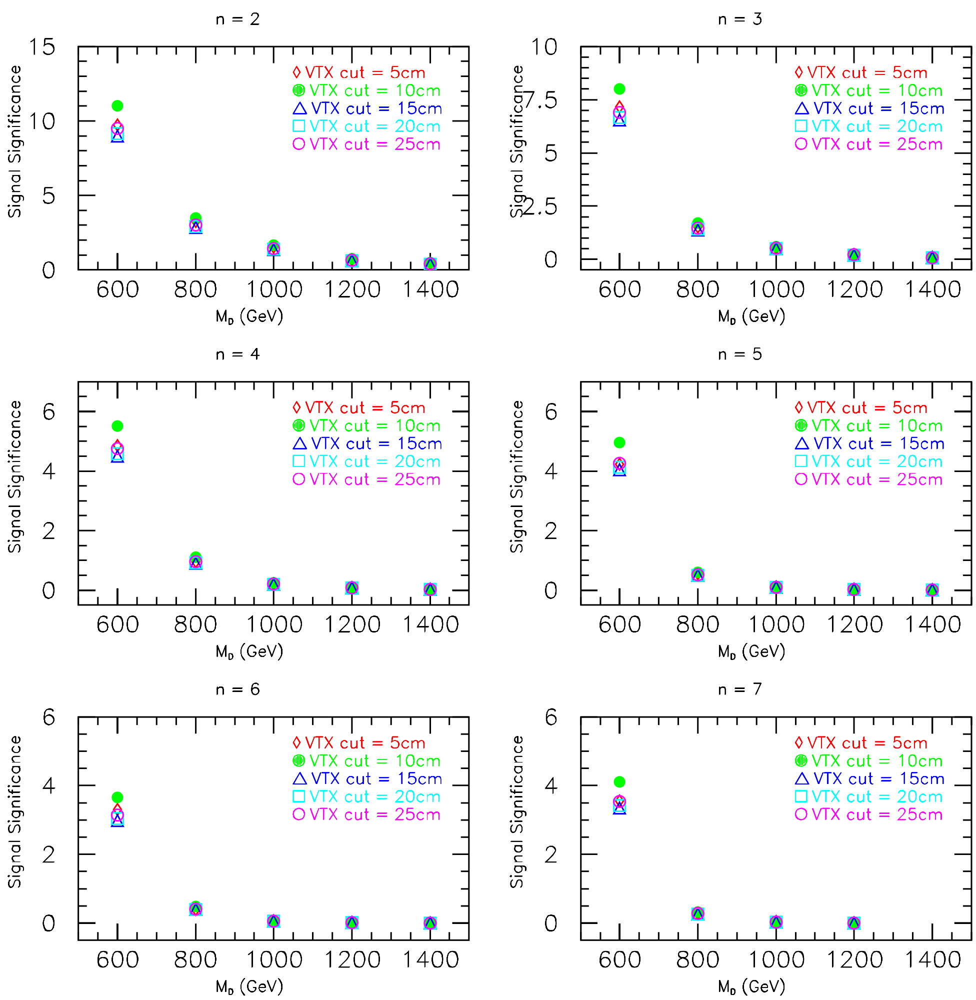

Figure 5.22. Signal significance of the primary vertex confirmation cut for all signal points with the leading jet $E_T/\not{E}_T > 150$ GeV, the second jet $E_T < 50$ GeV, and $|\eta_d| \leq 2.5$.

the signal significance for η_d including the ICR. This is not very surprising since some of our cuts are not effective in removing the backgrounds in the intercryostat region. And the results corresponding to $|\eta_d| \leq 1.0$, $|\eta_d| < 1.1$ or $1.5 < |\eta_d| \leq 2.5$, and $|\eta_d| \leq 2.5$ have already demonstrated this effect. But the signal significance is not very sensitive to this cut.

5.6.2.3 Optimization for Kinematic Cuts

We calculate the signal significance for the leading jet $E_T/\not{E}_T$ thresholds ranging from 115 GeV to 160 GeV (in 5 GeV intervals) and second jet $E_T \leq 30, 40, 50$ GeV on our available STA sample. As shown in Figure 5.25 (for signal point with $n = 2$ and $M_D = 800$ GeV only), the signal significance drops as the leading jet $E_T/\not{E}_T$ lower limit increases, while it increases as we raise the upper limit of second jet E_T despite the statistical fluctuation. Our current kinematic cuts are chosen not based on this optimization but with consideration to the final sample size and reference to [5].

5.6.3 Calculation of the Limits

With no excess of events over the Standard Model backgrounds, upper limits on the cross section for production LED are calculated. Lower limits on M_D for different n values can then be inferred from the upper cross section limits. A 95% confidence level (CL) cross section limit is calculated within Bayesian statistics and is described in Reference [65]. A brief outline of the calculation for the significance is given here.

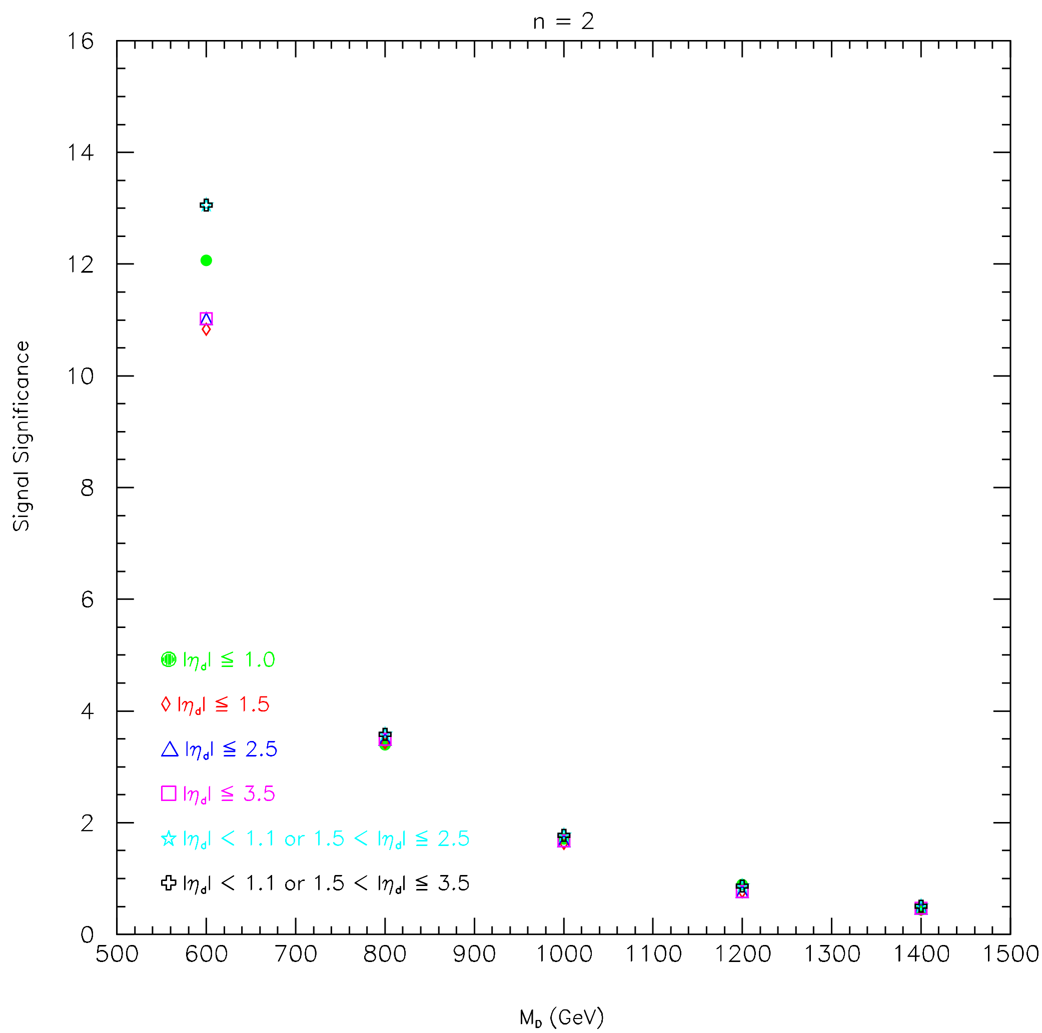

Figure 5.23. Signal significance of detector η cut on the leading jet for signal points with $n = 2$ and with the leading jet $\mathrm{E}_T/\not{E}_T > 150$ GeV and the second jet $\mathrm{E}_T < 50$ GeV.

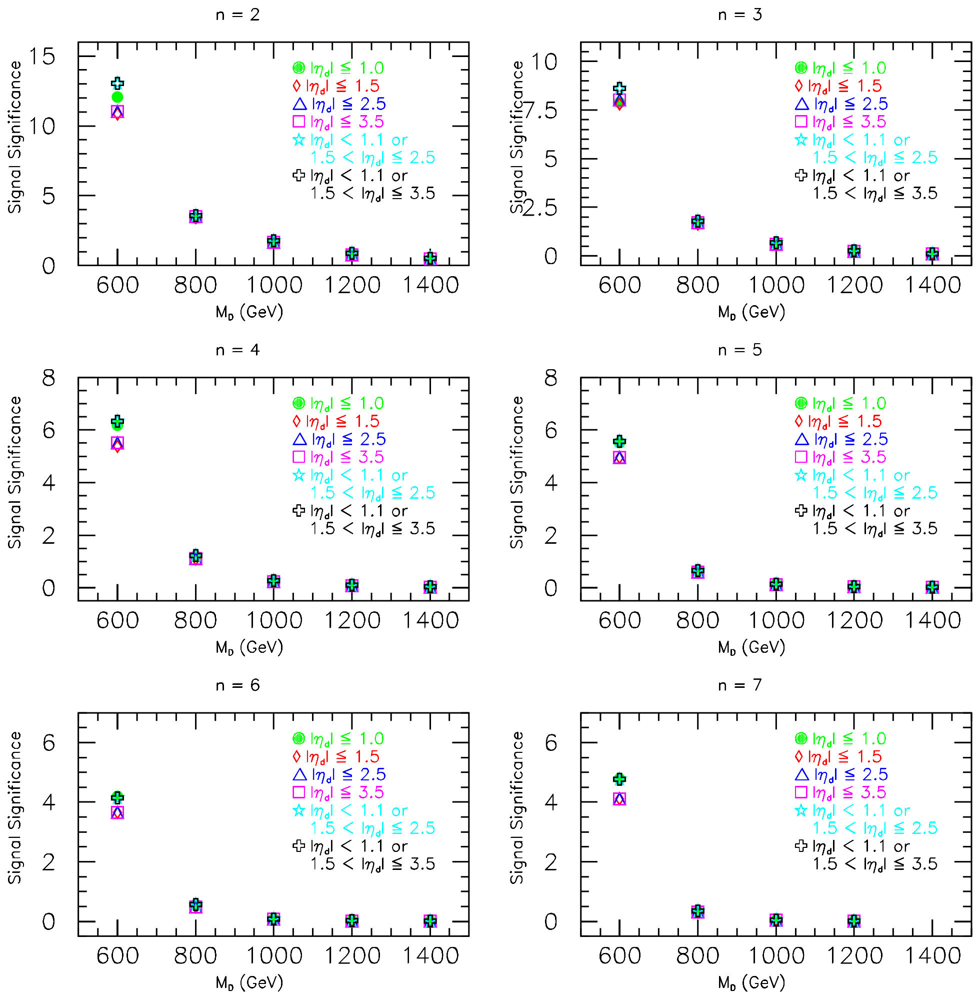

Figure 5.24. Signal significance of detector η cut on the leading jet for all signal points with the leading jet $\mathrm{E}_T/\not{E}_T > 150$ GeV and the second jet $\mathrm{E}_T < 50$ GeV.

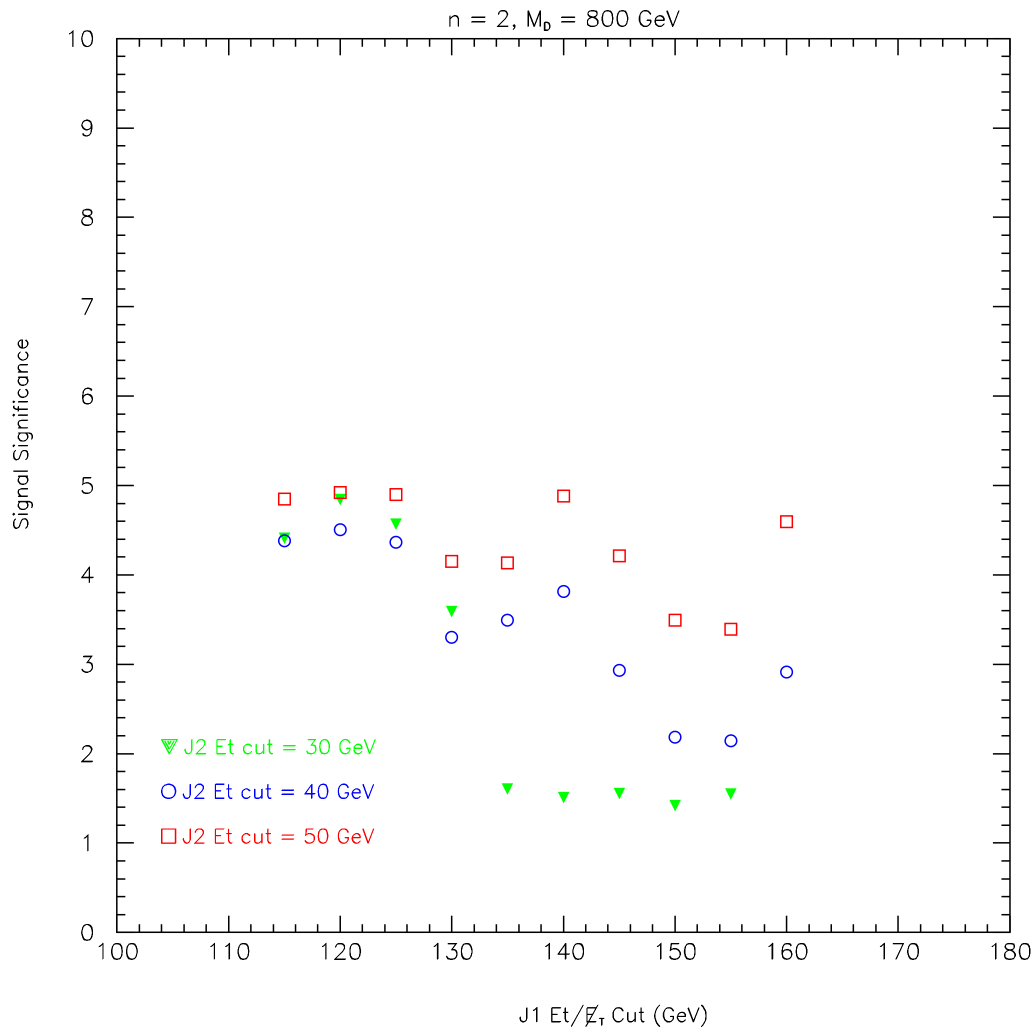

Figure 5.25. Signal significance of the kinematic cuts for signal point with $n = 2$, $M_D = 800$ GeV.

The expression that drives this calculation is from Bayes Theorem,

$$P(h|d,I) \propto P(d|h,I)P(h|I). \tag{5.5}$$

This equation states that the probability that a hypothesis h is true given the data d and other information I is proportional to the *likelihood* of observing the data d given the hypothesis h times the *prior probability* of hypothesis h being true without considering the data. The probability that hypothesis h is true is inferred from the data and the prior information. The constant of proportionality is determined from normalizing $P(h|d,I)$.

For this analysis, the model or hypothesis for the expected number of events (μ) in terms of the signal cross section (σ), the signal (if it exists) acceptance (ϵ), the integrated luminosity (L), and the expected background (b) is given by

$$\mu = b + L\epsilon\sigma. \tag{5.6}$$

The likelihood function for observing the data is the Poisson distribution. The probability or likelihood of observing k events in the data given an expectation value of μ is

$$P(k|\mu,I) = \frac{e^{-\mu}\mu^k}{k!}. \tag{5.7}$$

With the model of Equation (5.6), Equation (5.7) becomes

$$P(k|\sigma,L,\epsilon,b,I) = \frac{e^{-(b+L\epsilon\sigma)}(b+L\epsilon\sigma)^k}{k!}. \tag{5.8}$$

This expression is the probability of observing k events given σ, L, ϵ, and b.

The other needed part of Equation (5.5) is the prior probabilities for the parameters. The prior probability for the signal cross section is taken to be flat,

$$P(\sigma|I) = \begin{cases} 1/\sigma_{\max} & \text{if } 0 \le \sigma \le \sigma_{\max}, \\ 0 & \text{otherwise.} \end{cases} \tag{5.9}$$

$\sigma_{\max}$ is chosen to be large enough so that the likelihood that the true signal cross section is greater than $\sigma_{\max}$ is negligible. The prior probabilities for the luminosity, background, and signal efficiencies are represented by truncated Gaussians with the mean being the parameter value and standard deviation the parameter error.

With these parts, Bayes Theorem gives

$$P(\sigma\, L\epsilon\, b|k, I) \propto \frac{e^{-(b+L\epsilon\sigma)}(b + L\epsilon\sigma)^k}{k!} P(\sigma|I)\, P(L\,\epsilon\, b|I). \tag{5.10}$$

This equation is the joint probability distribution for the signal cross section, luminosity, signal efficiency, and background estimation. The desired result is the probability distribution for the signal cross section (σ), and so the other *nuisance parameters* are integrated out,

$$P(\sigma|k, I) = \int_0^\infty dL \int_0^1 d\epsilon \int_0^\infty db P(\sigma\, L\,\epsilon\, b|k, I). \tag{5.11}$$

$P(\sigma|k, I)$ is the probability distribution for the signal cross section given the data observed. The relevant result to report from a search is an upper limit on the signal cross section. The standard limit is at the 95% confidence level (CL), which can be determined by solving

$$0.95 = \int_0^{\sigma_{95}} P(\sigma|k, I) d\sigma, \tag{5.12}$$

where σ_{95} is the sought 95% CL upper limit.

Table 5.17, 5.19 and 5.21 list the 95% C.L. cross section limit for various signal model points with leading jet $|\eta_d| \leq 1.0$, $|\eta_d| \leq 2.5$ (excluding and including ICR: $1.1 \leq |\eta_d| \leq 1.5$). Table 5.18, 5.20 and 5.22 list the 95% C.L. cross section limit for various signal model points with leading jet $|\eta_d| \leq 1.0$, $|\eta_d| \leq 2.5$ (excluding and including ICR: $1.1 \leq |\eta_d| \leq 1.5$) while the signal contribution in the Q sample of QCD/cosmics estimation (Section 5.5.2) is being considered. The error of cross section is combined into the acceptance error in the tables. Comparing the calculated 95% C.L. cross section upper limit σ_{ul} in Table 5.17 and 5.18, Table 5.19 and 5.20,

Table 5.21 and 5.22, we can see that the difference in the limit is small for most sets of n and M_D of LED production; and for the points with larger difference (still small), they are clearly excluded if we compare the number of expected signal events with the number of observed events.

The signal generation is based on an effective low-energy theory, valid below the scale of M_D[5]. In hadron colliders the elementary scattering processes occur at different center-of-mass energies. In order to get an idea of the ultraviolet sensitivity, we also generate all the signal points with the effective center-of-mass energy in the parton collision $\sqrt{\hat{s}} < M_D$ which is denoted as σ_a in Table 5.23. When σ_b (no restriction on $\sqrt{\hat{s}}$) is about the same as σ_a, the dominant contribution comes from momenta smaller than M_D and the effective theory is fully applicable. When the difference between them is large, the ultraviolet contributions become important and the calculation is not under control. The perturbativity is dependent on the minimum jet E_T and n. The larger the value of n or the minimum jet E_T, the sooner the non-perturbative region is reached[5].

TABLE 5.17. NUMBER OF OBERVED DATA EVENTS, N_{obs}, EXPECTED TOTAL BACKGROUND EVENTS, $N_{background}^{total}$ AND ITS BREAKDOWN IN VARIOUS SOURCES, EXPECTED SIGNAL EVENTS, N_{signal}, SIGNAL ACCEPTANCE, A_{signal} , LED PRODUCTION CROSS SECTION AT EACH MODEL POINT AND THE CALCULATED 95% C.L. CROSS SECTION UPPER LIMIT WITH THE LEADING JET $E_T/\not{E}_T > 150$ GeV, THE SECOND JET $E_T < 50$ GeV, AND $|\eta_d| \leq 1.0$.

n	M_D (GeV)	N_{obs}	$N_{background}^{total}$	N_{total}^{WZ}	$N_{QCD/\cos}$	N_{signal}	a_{signal} (%)	σ_{th} (pb)	σ_{ul} (pb)
2	600	38	38.0 ± 9.6	30.2 ± 6.4	7.8 ± 7.1	138 ± 25	5.3 ± 0.9	32.96	6.284
2	800	38	38.0 ± 9.6	30.2 ± 6.4	7.8 ± 7.1	38.7 ± 8.0	4.7 ± 0.9	10.44	7.377
2	1000	38	38.0 ± 9.6	30.2 ± 6.4	7.8 ± 7.1	19.5 ± 3.9	5.8 ± 1.1	4.265	5.906
2	1200	38	38.0 ± 9.6	30.2 ± 6.4	7.8 ± 7.1	10.2 ± 1.7	6.3 ± 1.0	2.056	5.168
2	1400	38	38.0 ± 9.6	30.2 ± 6.4	7.8 ± 7.1	5.06 ± 0.86	5.8 ± 0.9	1.108	5.655
3	600	38	38.0 ± 9.6	30.2 ± 6.4	7.8 ± 7.1	89.9 ± 15.5	6.3 ± 1.0	18.11	5.217
3	800	38	38.0 ± 9.6	30.2 ± 6.4	7.8 ± 7.1	19.7 ± 3.8	5.8 ± 1.1	4.311	5.835
3	1000	38	38.0 ± 9.6	30.2 ± 6.4	7.8 ± 7.1	7.34 ± 1.42	6.6 ± 1.2	1.411	5.121
3	1200	38	38.0 ± 9.6	30.2 ± 6.4	7.8 ± 7.1	2.86 ± 0.46	6.4 ± 1.0	0.5676	5.064
3	1400	38	38.0 ± 9.6	30.2 ± 6.4	7.8 ± 7.1	1.16 ± 0.20	5.6 ± 0.9	0.2622	5.844
4	600	38	38.0 ± 9.6	30.2 ± 6.4	7.8 ± 7.1	70.6 ± 11.7	7.0 ± 1.1	12.79	4.649
4	800	38	38.0 ± 9.6	30.2 ± 6.4	7.8 ± 7.1	13.8 ± 2.5	7.7 ± 1.3	2.278	4.305
4	1000	38	38.0 ± 9.6	30.2 ± 6.4	7.8 ± 7.1	2.96 ± 0.57	6.3 ± 1.2	0.5967	5.361
4	1200	38	38.0 ± 9.6	30.2 ± 6.4	7.8 ± 7.1	1.07 ± 0.17	6.8 ± 1.0	0.2004	4.735
4	1400	38	38.0 ± 9.6	30.2 ± 6.4	7.8 ± 7.1	0.357 ± 0.059	5.7 ± 0.9	0.07953	5.712
5	600	38	38.0 ± 9.6	30.2 ± 6.4	7.8 ± 7.1	63.1 ± 10.3	7.5 ± 1.2	10.68	4.331
5	800	38	38.0 ± 9.6	30.2 ± 6.4	7.8 ± 7.1	7.59 ± 1.41	6.7 ± 1.2	1.438	4.988
5	1000	38	38.0 ± 9.6	30.2 ± 6.4	7.8 ± 7.1	1.49 ± 0.29	6.3 ± 1.2	0.3004	5.369
5	1200	38	38.0 ± 9.6	30.2 ± 6.4	7.8 ± 7.1	0.437 ± 0.070	6.6 ± 1.0	0.08405	4.894
5	1400	38	38.0 ± 9.6	30.2 ± 6.4	7.8 ± 7.1	0.175 ± 0.027	7.8 ± 1.1	0.02851	4.108
6	600	38	38.0 ± 9.6	30.2 ± 6.4	7.8 ± 7.1	47.9 ± 8.3	6.1 ± 1.0	9.957	5.386
6	800	38	38.0 ± 9.6	30.2 ± 6.4	7.8 ± 7.1	6.48 ± 1.16	8.2 ± 1.4	1.002	4.036
6	1000	38	38.0 ± 9.6	30.2 ± 6.4	7.8 ± 7.1	0.965 ± 0.181	7.3 ± 1.3	0.1678	4.588
6	1200	38	38.0 ± 9.6	30.2 ± 6.4	7.8 ± 7.1	0.228 ± 0.035	7.4 ± 1.1	0.03903	4.336
6	1400	38	38.0 ± 9.6	30.2 ± 6.4	7.8 ± 7.1	0.0699 ± 0.0106	7.8 ± 1.1	0.01137	4.108
7	600	38	37.8 ± 9.6	30.2 ± 6.4	7.8 ± 7.1	54.6 ± 9.1	7.0 ± 1.1	9.986	4.658
7	800	38	38.0 ± 9.6	30.2 ± 6.4	7.8 ± 7.1	4.04 ± 0.75	6.9 ± 1.2	0.7422	4.840
7	1000	38	38.0 ± 9.6	30.2 ± 6.4	7.8 ± 7.1	0.511 ± 0.099	6.5 ± 1.2	0.09974	5.199
7	1200	38	38.0 ± 9.6	30.2 ± 6.4	7.8 ± 7.1	0.105 ± 0.016	6.9 ± 1.0	0.01932	4.674

TABLE 5.18. NUMBER OF OBERVED DATA EVENTS, N_{obs}, EXPECTED TOTAL BACKGROUND EVENTS, $N^{total}_{background}$ AND ITS BREAKDOWN IN VARIOUS SOURCES WITH SIGNAL CONTRIBUTION IN THE Q SAMPLE OF QCD ESTIMATION CONSIDERED, EXPECTED SIGNAL EVENTS, N_{signal}, SIGNAL ACCEPTANCE, A_{signal} , LED PRODUCTION CROSS SECTION AT EACH MODEL POINT AND THE CALCULATED 95% C.L. CROSS SECTION UPPER LIMIT WITH THE LEADING JET $E_T/\not{E}_T > 150$ GeV, THE SECOND JET $E_T < 50$ GeV, AND $|\eta_d| \leq 1.0$.

n	M_D (GeV)	N_{obs}	$N^{total}_{background}$	N^{WZ}_{total}	$N_{QCD/\cos}$	N_{signal}	a_{signal} (%)	σ_{th} (pb)	σ_{ul} (pb)
2	600	38	31.0 ± 7.1	30.2 ± 6.4	0.8 ± 3.0	138 ± 25	5.3 ± 0.9	32.96	6.744
2	800	38	36.0 ± 8.4	30.2 ± 6.4	5.8 ± 5.5	38.7 ± 8.0	4.7 ± 0.9	10.44	7.257
2	1000	38	37.0 ± 9.0	30.2 ± 6.4	6.8 ± 6.3	19.5 ± 3.9	5.8 ± 1.1	4.265	5.838
2	1200	38	37.5 ± 9.3	30.2 ± 6.4	7.3 ± 6.7	10.2 ± 1.7	6.3 ± 1.0	2.056	5.108
2	1400	38	37.7 ± 9.4	30.2 ± 6.4	7.5 ± 6.9	5.06 ± 0.86	5.8 ± 0.9	1.108	5.601
3	600	38	33.7 ± 7.5	30.2 ± 6.4	3.5 ± 3.8	89.9 ± 15.5	6.3 ± 1.0	18.11	5.180
3	800	38	37.0 ± 9.0	30.2 ± 6.4	6.8 ± 6.3	19.7 ± 3.8	5.8 ± 1.1	4.311	5.771
3	1000	38	37.7 ± 9.4	30.2 ± 6.4	7.5 ± 6.8	7.34 ± 1.42	6.6 ± 1.2	1.411	5.102
3	1200	38	37.9 ± 9.5	30.2 ± 6.4	7.6 ± 7.0	2.86 ± 0.46	6.4 ± 1.0	0.5676	5.074
3	1400	38	37.9 ± 9.6	30.2 ± 6.4	7.7 ± 7.1	1.16 ± 0.20	5.6 ± 0.9	0.2622	5.858
4	600	38	35.0 ± 7.9	30.2 ± 6.4	4.8 ± 4.7	70.6 ± 11.7	7.0 ± 1.1	12.79	4.546
4	800	38	37.4 ± 9.2	30.2 ± 6.4	7.1 ± 6.6	13.8 ± 2.5	7.7 ± 1.3	2.278	4.254
4	1000	38	37.8 ± 9.5	30.2 ± 6.4	7.6 ± 7.0	2.96 ± 0.57	6.3 ± 1.2	0.5967	5.396
4	1200	38	38.0 ± 9.6	30.2 ± 6.4	7.7 ± 7.1	1.07 ± 0.17	6.8 ± 1.0	0.2004	4.726
4	1400	38	38.0 ± 9.6	30.2 ± 6.4	7.8 ± 7.1	0.357 ± 0.059	5.7 ± 0.9	0.07953	5.725
5	600	38	35.0 ± 7.9	30.2 ± 6.4	4.8 ± 4.6	63.1 ± 10.3	7.5 ± 1.2	10.68	4.227
5	800	38	37.7 ± 9.4	30.2 ± 6.4	7.4 ± 6.8	7.59 ± 1.41	6.7 ± 1.2	1.438	4.962
5	1000	38	37.9 ± 9.6	30.2 ± 6.4	7.7 ± 7.1	1.49 ± 0.29	6.3 ± 1.2	0.3004	5.383
5	1200	38	38.0 ± 9.6	30.2 ± 6.4	7.8 ± 7.1	0.437 ± 0.070	6.6 ± 1.0	0.08405	4.900
5	1400	38	38.0 ± 9.6	30.2 ± 6.4	7.8 ± 7.1	0.175 ± 0.027	7.8 ± 1.1	0.02851	4.118
6	600	38	35.6 ± 8.2	30.2 ± 6.4	5.4 ± 5.2	47.9 ± 8.3	6.1 ± 1.0	9.957	5.262
6	800	38	37.7 ± 9.4	30.2 ± 6.4	7.5 ± 6.8	6.48 ± 1.16	8.2 ± 1.4	1.002	4.005
6	1000	38	38.0 ± 9.6	30.2 ± 6.4	7.7 ± 7.1	0.965 ± 0.181	7.3 ± 1.3	0.1678	4.586
6	1200	38	38.0 ± 9.6	30.2 ± 6.4	7.8 ± 7.1	0.228 ± 0.035	7.4 ± 1.1	0.03903	4.348
6	1400	38	38.0 ± 9.6	30.2 ± 6.4	7.8 ± 7.1	0.0699 ± 0.0106	7.8 ± 1.1	0.01137	4.111
7	600	38	35.7 ± 8.3	30.2 ± 6.4	5.5 ± 5.2	54.6 ± 9.1	7.0 ± 1.1	9.986	4.550
7	800	38	37.8 ± 9.5	30.2 ± 6.4	7.6 ± 7.0	4.04 ± 0.75	6.9 ± 1.2	0.7422	4.868
7	1000	38	38.0 ± 9.6	30.2 ± 6.4	7.8 ± 7.1	0.511 ± 0.099	6.5 ± 1.2	0.09974	5.208
7	1200	38	38.0 ± 9.6	30.2 ± 6.4	7.8 ± 7.1	0.105 ± 0.016	6.9 ± 1.0	0.01932	4.677

TABLE 5.19. NUMBER OF OBERVED DATA EVENTS, N_{obs}, EXPECTED TOTAL BACKGROUND EVENTS, $N^{total}_{background}$ AND ITS BREAKDOWN IN VARIOUS SOURCES, EXPECTED SIGNAL EVENTS, N_{signal}, SIGNAL ACCEPTANCE, A_{signal} , LED PRODUCTION CROSS SECTION AT EACH MODEL POINT AND THE CALCULATED 95% C.L. CROSS SECTION UPPER LIMIT WITH THE LEADING JET $E_T/\not{E}_T > 150$ GeV, THE SECOND JET $E_T < 50$ GeV, AND $|\eta_d| < 1.1$ OR $1.5 < |\eta_d| \leq 2.5$.

n	M_D (GeV)	N_{obs}	$N^{total}_{background}$	N^{WZ}_{total}	$N_{QCD/\cos}$	N_{signal}	a_{signal} (%)	σ_{th} (pb)	σ_{ul} (pb)
2	600	47	39.7 ± 10.1	31.8 ± 7.2	7.8 ± 7.2	156 ± 27	6.0 ± 1.0	32.96	7.168
2	800	47	39.7 ± 10.1	31.8 ± 7.2	7.8 ± 7.2	42.8 ± 8.5	5.2 ± 1.0	10.44	8.569
2	1000	47	39.7 ± 10.1	31.8 ± 7.2	7.8 ± 7.2	21.2 ± 4.3	6.3 ± 1.2	4.265	7.165
2	1200	47	39.7 ± 10.1	31.8 ± 7.2	7.8 ± 7.2	10.4 ± 1.7	6.4 ± 1.0	2.056	6.624
2	1400	47	39.7 ± 10.1	31.8 ± 7.2	7.8 ± 7.2	6.02 ± 1.05	6.9 ± 1.1	1.108	6.220
3	600	47	39.7 ± 10.1	31.8 ± 7.2	7.8 ± 7.2	103 ± 17	7.2 ± 1.1	18.11	5.891
3	800	47	39.7 ± 10.1	31.8 ± 7.2	7.8 ± 7.2	21.4 ± 4.0	6.3 ± 1.1	4.311	6.938
3	1000	47	39.7 ± 10.1	31.8 ± 7.2	7.8 ± 7.2	8.12 ± 1.60	7.3 ± 1.4	1.411	6.086
3	1200	47	39.7 ± 10.1	31.8 ± 7.2	7.8 ± 7.2	3.00 ± 0.48	6.7 ± 1.0	0.5676	6.285
3	1400	47	39.7 ± 10.1	31.8 ± 7.2	7.8 ± 7.2	1.30 ± 0.23	6.3 ± 1.0	0.2622	6.823
4	600	47	39.7 ± 10.1	31.8 ± 7.2	7.8 ± 7.2	75.6 ± 12.1	7.5 ± 1.1	12.79	5.621
4	800	47	39.7 ± 10.1	31.8 ± 7.2	7.8 ± 7.2	14.7 ± 2.6	8.2 ± 1.4	2.278	5.237
4	1000	47	39.7 ± 10.1	31.8 ± 7.2	7.8 ± 7.2	3.15 ± 0.62	6.7 ± 1.3	0.5967	6.645
4	1200	47	39.7 ± 10.1	31.8 ± 7.2	7.8 ± 7.2	1.17 ± 0.18	7.4 ± 1.0	0.2004	5.641
4	1400	47	39.7 ± 10.1	31.8 ± 7.2	7.8 ± 7.2	0.401 ± 0.069	6.4 ± 1.0	0.07953	6.679
5	600	47	39.7 ± 10.1	31.8 ± 7.2	7.8 ± 7.2	66.5 ± 10.6	7.9 ± 1.2	10.68	5.330
5	800	47	39.7 ± 10.1	31.8 ± 7.2	7.8 ± 7.2	7.71 ± 1.40	6.8 ± 1.2	1.438	6.388
5	1000	47	39.7 ± 10.1	31.8 ± 7.2	7.8 ± 7.2	1.61 ± 0.32	6.8 ± 1.3	0.3004	6.552
5	1200	47	39.7 ± 10.1	31.8 ± 7.2	7.8 ± 7.2	0.477 ± 0.074	7.2 ± 1.0	0.08405	5.810
5	1400	47	39.7 ± 10.1	31.8 ± 7.2	7.8 ± 7.2	0.193 ± 0.031	8.6 ± 1.3	0.02851	4.908
6	600	47	39.7 ± 10.1	31.8 ± 7.2	7.8 ± 7.2	49.4 ± 8.4	6.3 ± 1.0	9.957	6.765
6	800	47	39.7 ± 10.1	31.8 ± 7.2	7.8 ± 7.2	6.79 ± 1.18	8.6 ± 1.4	1.002	4.987
6	1000	47	39.7 ± 10.1	31.8 ± 7.2	7.8 ± 7.2	0.979 ± 0.191	7.4 ± 1.4	0.1678	5.986
6	1200	47	39.7 ± 10.1	31.8 ± 7.2	7.8 ± 7.2	0.246 ± 0.037	8.0 ± 1.1	0.03903	5.208
6	1400	47	39.7 ± 10.1	31.8 ± 7.2	7.8 ± 7.2	0.0735 ± 0.0119	8.2 ± 1.3	0.01137	5.158
7	600	47	39.7 ± 10.1	31.8 ± 7.2	7.8 ± 7.2	56.9 ± 9.3	7.3 ± 1.1	9.986	5.799
7	800	47	39.7 ± 10.1	31.8 ± 7.2	7.8 ± 7.2	4.21 ± 0.76	7.2 ± 1.2	0.7422	6.022
7	1000	47	39.7 ± 10.1	31.8 ± 7.2	7.8 ± 7.2	0.558 ± 0.110	7.1 ± 1.4	0.09974	6.263
7	1200	47	39.7 ± 10.1	31.8 ± 7.2	7.8 ± 7.2	0.111 ± 0.017	7.3 ± 1.1	0.01932	5.736

TABLE 5.20. NUMBER OF OBERVED DATA EVENTS, N_{obs}, EXPECTED TOTAL BACKGROUND EVENTS, $N^{total}_{background}$ AND ITS BREAKDOWN IN VARIOUS SOURCES WITH SIGNAL CONTRIBUTION IN THE Q SAMPLE OF QCD ESTIMATION CONSIDERED, EXPECTED SIGNAL EVENTS, N_{signal}, SIGNAL ACCEPTANCE, A_{signal} , LED PRODUCTION CROSS SECTION AT EACH MODEL POINT AND THE CALCULATED 95% C.L. CROSS SECTION UPPER LIMIT WITH THE LEADING JET $E_T/\not{E}_T > 150$ GeV, THE SECOND JET $E_T < 50$ GeV, AND $|\eta_d| < 1.1$ OR $1.5 < |\eta_d| \leq 2.5$.

n	M_D (GeV)	N_{obs}	$N^{total}_{background}$	N^{WZ}_{total}	$N_{QCD/\cos}$	N_{signal}	a_{signal} (%)	σ_{th} (pb)	σ_{ul} (pb)
2	600	47	32.7 ± 7.8	31.8 ± 7.2	0.8 ± 3.0	156 ± 27	6.0 ± 1.0	32.96	7.930
2	800	47	38.0 ± 9.2	31.8 ± 7.2	6.1 ± 5.7	42.8 ± 8.5	5.2 ± 1.0	10.44	8.621
2	1000	47	38.8 ± 9.6	31.8 ± 7.2	6.9 ± 6.4	21.2 ± 4.3	6.3 ± 1.2	4.265	7.186
2	1200	47	39.2 ± 9.8	31.8 ± 7.2	7.3 ± 6.7	10.4 ± 1.7	6.4 ± 1.0	2.056	6.669
2	1400	47	39.4 ± 10.0	31.8 ± 7.2	7.6 ± 7.0	6.02 ± 1.05	6.9 ± 1.1	1.108	6.232
3	600	47	35.4 ± 8.2	31.8 ± 7.2	3.6 ± 3.8	103 ± 17	7.2 ± 1.1	18.11	6.073
3	800	47	38.8 ± 9.6	31.8 ± 7.2	6.9 ± 6.4	21.4 ± 4.0	6.3 ± 1.1	4.311	6.962
3	1000	47	39.4 ± 10.0	31.8 ± 7.2	7.6 ± 6.9	8.12 ± 1.60	7.3 ± 1.4	1.411	6.089
3	1200	47	39.6 ± 10.1	31.8 ± 7.2	7.7 ± 7.1	3.00 ± 0.48	6.7 ± 1.0	0.5676	6.269
3	1400	47	39.6 ± 10.1	31.8 ± 7.2	7.8 ± 7.1	1.30 ± 0.23	6.3 ± 1.0	0.2622	6.818
4	600	47	36.4 ± 8.5	31.8 ± 7.2	4.5 ± 4.5	75.6 ± 12.1	7.5 ± 1.1	12.79	5.717
4	800	47	38.9 ± 9.7	31.8 ± 7.2	7.1 ± 6.5	14.7 ± 2.6	8.2 ± 1.4	2.278	5.248
4	1000	47	39.5 ± 10.0	31.8 ± 7.2	7.7 ± 7.0	3.15 ± 0.62	6.7 ± 1.3	0.5967	6.627
4	1200	47	39.6 ± 10.1	31.8 ± 7.2	7.8 ± 7.1	1.17 ± 0.18	7.4 ± 1.0	0.2004	5.626
4	1400	47	39.7 ± 10.1	31.8 ± 7.2	7.8 ± 7.2	0.401 ± 0.069	6.4 ± 1.0	0.07953	6.675
5	600	47	36.4 ± 8.5	31.8 ± 7.2	4.6 ± 4.5	66.5 ± 10.6	7.9 ± 1.2	10.68	5.413
5	800	47	39.4 ± 10.0	31.8 ± 7.2	7.5 ± 6.9	7.71 ± 1.40	6.8 ± 1.2	1.438	6.400
5	1000	47	39.6 ± 10.1	31.8 ± 7.2	7.8 ± 7.1	1.61 ± 0.32	6.8 ± 1.3	0.3004	6.552
5	1200	47	39.7 ± 10.1	31.8 ± 7.2	7.8 ± 7.1	0.477 ± 0.074	7.2 ± 1.0	0.08405	5.812
5	1400	47	39.7 ± 10.1	31.8 ± 7.2	7.8 ± 7.2	0.193 ± 0.031	8.6 ± 1.3	0.02851	4.906
6	600	47	37.3 ± 8.9	31.8 ± 7.2	5.5 ± 5.2	49.4 ± 8.4	6.3 ± 1.0	9.957	6.825
6	800	47	39.3 ± 9.9	31.8 ± 7.2	7.5 ± 6.8	6.79 ± 1.18	8.6 ± 1.4	1.002	5.010
6	1000	47	39.6 ± 10.1	31.8 ± 7.2	7.8 ± 7.1	0.979 ± 0.191	7.4 ± 1.4	0.1678	5.982
6	1200	47	39.7 ± 10.1	31.8 ± 7.2	7.8 ± 7.2	0.246 ± 0.037	8.0 ± 1.1	0.03903	5.204
6	1400	47	39.7 ± 10.1	31.8 ± 7.2	7.8 ± 7.2	0.0735 ± 0.0119	8.2 ± 1.3	0.01137	5.158
7	600	47	37.4 ± 8.9	31.8 ± 7.2	5.5 ± 5.2	56.9 ± 9.3	7.3 ± 1.1	9.986	5.846
7	800	47	39.5 ± 10.0	31.8 ± 7.2	7.6 ± 7.0	4.21 ± 0.76	7.2 ± 1.2	0.7422	6.015
7	1000	47	39.7 ± 10.1	31.8 ± 7.2	7.8 ± 7.1	0.558 ± 0.110	7.1 ± 1.4	0.09974	6.263
7	1200	47	39.7 ± 10.1	31.8 ± 7.2	7.8 ± 7.2	0.111 ± 0.017	7.3 ± 1.1	0.01932	5.734

TABLE 5.21. NUMBER OF OBERVED DATA EVENTS, N_{obs}, EXPECTED TOTAL BACKGROUND EVENTS, $N^{total}_{background}$ AND ITS BREAKDOWN IN VARIOUS SOURCES, EXPECTED SIGNAL EVENTS, N_{signal}, SIGNAL ACCEPTANCE, A_{signal} , LED PRODUCTION CROSS SECTION AT EACH MODEL POINT AND THE CALCULATED 95% C.L. CROSS SECTION UPPER LIMIT WITH THE LEADING JET $E_T/\not{E}_T > 150$ GeV, THE SECOND JET $E_T < 50$ GeV, AND $|\eta_d| \leq 2.5$.

n	M_D (GeV)	N_{obs}	$N^{total}_{background}$	N^{WZ}_{total}	$N_{QCD/\cos}$	N_{signal}	a_{signal} (%)	σ_{th} (pb)	σ_{ul} (pb)
2	600	58	49.7 ± 12.8	37.2 ± 8.3	12.5 ± 9.8	161 ± 28	6.2 ± 1.0	32.96	8.256
2	800	58	49.7 ± 12.8	37.2 ± 8.3	12.5 ± 9.8	51.0 ± 9.9	6.2 ± 1.2	10.44	8.514
2	1000	58	49.7 ± 12.8	37.2 ± 8.3	12.5 ± 9.8	24.5 ± 4.8	7.3 ± 1.4	4.265	7.248
2	1200	58	49.7 ± 12.8	37.2 ± 8.3	12.5 ± 9.8	11.2 ± 1.8	6.9 ± 1.1	2.056	7.325
2	1400	58	49.7 ± 12.8	37.2 ± 8.3	12.5 ± 9.8	6.90 ± 1.17	7.9 ± 1.3	1.108	6.432
3	600	58	49.7 ± 12.8	37.2 ± 8.3	12.5 ± 9.8	117 ± 19	8.2 ± 1.2	18.11	6.122
3	800	58	49.7 ± 12.8	37.2 ± 8.3	12.5 ± 9.8	24.8 ± 4.6	7.3 ± 1.3	4.311	7.133
3	1000	58	49.7 ± 12.8	37.2 ± 8.3	12.5 ± 9.8	8.78 ± 1.66	7.9 ± 1.4	1.411	6.638
3	1200	58	49.7 ± 12.8	37.2 ± 8.3	12.5 ± 9.8	3.53 ± 0.55	7.9 ± 1.2	0.5676	6.334
3	1400	58	49.7 ± 12.8	37.2 ± 8.3	12.5 ± 9.8	1.47 ± 0.25	7.1 ± 1.2	0.2622	7.177
4	600	58	49.7 ± 12.8	37.2 ± 8.3	12.5 ± 9.8	80.6 ± 12.6	8.0 ± 1.2	12.79	6.259
4	800	58	49.7 ± 12.8	37.2 ± 8.3	12.5 ± 9.8	16.2 ± 2.8	9.0 ± 1.5	2.278	5.695
4	1000	58	49.7 ± 12.8	37.2 ± 8.3	12.5 ± 9.8	3.53 ± 0.66	7.5 ± 1.4	0.5967	6.981
4	1200	58	49.7 ± 12.8	37.2 ± 8.3	12.5 ± 9.8	1.30 ± 0.20	8.2 ± 1.2	0.2004	6.074
4	1400	58	49.7 ± 12.8	37.2 ± 8.3	12.5 ± 9.8	0.458 ± 0.076	7.3 ± 1.2	0.07953	6.937
5	600	58	49.7 ± 12.8	37.2 ± 8.3	12.5 ± 9.8	72.4 ± 11.2	8.6 ± 1.3	10.68	5.812
5	800	58	49.7 ± 12.8	37.2 ± 8.3	12.5 ± 9.8	8.84 ± 1.60	7.8 ± 1.4	1.438	6.632
5	1000	58	49.7 ± 12.8	37.2 ± 8.3	12.5 ± 9.8	1.75 ± 0.33	7.4 ± 1.4	0.3004	7.096
5	1200	58	49.7 ± 12.8	37.2 ± 8.3	12.5 ± 9.8	0.510 ± 0.079	7.7 ± 1.1	0.08405	6.491
5	1400	58	49.7 ± 12.8	37.2 ± 8.3	12.5 ± 9.8	0.222 ± 0.035	9.9 ± 1.5	0.02851	5.058
6	600	58	49.7 ± 12.8	37.2 ± 8.3	12.5 ± 9.8	53.4 ± 8.8	6.8 ± 1.1	9.957	7.433
6	800	58	49.7 ± 12.8	37.2 ± 8.3	12.5 ± 9.8	6.95 ± 1.22	8.8 ± 1.5	1.002	5.843
6	1000	58	49.7 ± 12.8	37.2 ± 8.3	12.5 ± 9.8	1.11 ± 0.21	8.4 ± 1.5	0.1678	6.211
6	1200	58	49.7 ± 12.8	37.2 ± 8.3	12.5 ± 9.8	0.255 ± 0.039	8.3 ± 1.2	0.03903	6.007
6	1400	58	49.7 ± 12.8	37.2 ± 8.3	12.5 ± 9.8	0.0780 ± 0.0126	8.7 ± 1.3	0.01137	5.782
7	600	58	49.7 ± 12.8	37.2 ± 8.3	12.5 ± 9.8	60.0 ± 9.6	7.7 ± 1.2	9.986	6.530
7	800	58	49.7 ± 12.8	37.2 ± 8.3	12.5 ± 9.8	4.62 ± 0.84	7.9 ± 1.4	0.7422	6.552
7	1000	58	49.7 ± 12.8	37.2 ± 8.3	12.5 ± 9.8	0.605 ± 0.115	7.7 ± 1.4	0.09974	6.815
7	1200	58	49.7 ± 12.8	37.2 ± 8.3	12.5 ± 9.8	0.119 ± 0.018	7.8 ± 1.2	0.01932	6.414

TABLE 5.22. NUMBER OF OBERVED DATA EVENTS, N_{obs}, EXPECTED TOTAL BACKGROUND EVENTS, $N^{total}_{background}$ AND ITS BREAKDOWN IN VARIOUS SOURCES WITH SIGNAL CONTRIBUTION IN THE Q SAMPLE OF QCD ESTIMATION CONSIDERED, EXPECTED SIGNAL EVENTS, N_{signal}, SIGNAL ACCEPTANCE, A_{signal} , LED PRODUCTION CROSS SECTION AT EACH MODEL POINT AND THE CALCULATED 95% C.L. CROSS SECTION UPPER LIMIT WITH THE LEADING JET $E_T/\not{E}_T > 150$ GeV, THE SECOND JET $E_T < 50$ GeV, AND $|\eta_d| \leq 2.5$.

n	M_D (GeV)	N_{obs}	$N^{total}_{background}$	N^{WZ}_{total}	$N_{QCD/\cos}$	N_{signal}	a_{signal} (%)	σ_{th} (pb)	σ_{ul} (pb)
2	600	58	40.1 ± 9.6	37.2 ± 8.3	2.9 ± 4.9	161 ± 28	6.2 ± 1.0	32.96	9.203
2	800	58	47.0 ± 11.5	37.2 ± 8.3	9.8 ± 7.9	51.0 ± 9.9	6.2 ± 1.2	10.44	8.582
2	1000	58	48.3 ± 12.0	37.2 ± 8.3	11.1 ± 8.8	24.5 ± 4.8	7.3 ± 1.4	4.265	7.261
2	1200	58	49.0 ± 12.4	37.2 ± 8.3	11.8 ± 9.3	11.2 ± 1.8	6.9 ± 1.1	2.056	7.304
2	1400	58	49.2 ± 12.5	37.2 ± 8.3	12.0 ± 9.4	6.90 ± 1.17	7.9 ± 1.3	1.108	6.418
3	600	58	43.1 ± 10.0	37.2 ± 8.3	5.9 ± 5.6	117 ± 19	8.2 ± 1.2	18.11	6.406
3	800	58	48.6 ± 12.2	37.2 ± 8.3	11.4 ± 9.0	24.8 ± 4.6	7.3 ± 1.3	4.311	7.182
3	1000	58	49.2 ± 12.5	37.2 ± 8.3	12.0 ± 9.4	8.78 ± 1.66	7.9 ± 1.4	1.411	6.616
3	1200	58	49.4 ± 12.7	37.2 ± 8.3	12.2 ± 9.6	3.53 ± 0.55	7.9 ± 1.2	0.5676	6.321
3	1400	58	49.6 ± 12.8	37.2 ± 8.3	12.4 ± 9.7	1.47 ± 0.25	7.1 ± 1.2	0.2622	7.188
4	600	58	43.6 ± 10.1	37.2 ± 8.3	6.4 ± 5.8	80.6 ± 12.6	8.0 ± 1.2	12.79	6.479
4	800	58	48.6 ± 12.2	37.2 ± 8.3	11.4 ± 9.0	16.2 ± 2.8	9.0 ± 1.5	2.278	5.706
4	1000	58	49.4 ± 12.7	37.2 ± 8.3	12.2 ± 9.6	3.53 ± 0.66	7.5 ± 1.4	0.5967	6.967
4	1200	58	49.6 ± 12.8	37.2 ± 8.3	12.4 ± 9.7	1.30 ± 0.20	8.2 ± 1.2	0.2004	6.076
4	1400	58	49.6 ± 12.8	37.2 ± 8.3	12.4 ± 9.7	0.458 ± 0.076	7.3 ± 1.2	0.07953	6.940
5	600	58	44.2 ± 10.3	37.2 ± 8.3	7.0 ± 6.1	72.4 ± 11.2	8.6 ± 1.3	10.68	5.966
5	800	58	49.2 ± 12.5	37.2 ± 8.3	12.0 ± 9.4	8.84 ± 1.60	7.8 ± 1.4	1.438	6.594
5	1000	58	49.6 ± 12.7	37.2 ± 8.3	12.4 ± 9.7	1.75 ± 0.33	7.4 ± 1.4	0.3004	7.100
5	1200	58	49.6 ± 12.8	37.2 ± 8.3	12.4 ± 9.7	0.510 ± 0.079	7.7 ± 1.1	0.08405	6.491
5	1400	58	49.7 ± 12.8	37.2 ± 8.3	12.5 ± 9.8	0.222 ± 0.035	9.9 ± 1.5	0.02851	5.054
6	600	58	46.4 ± 11.2	37.2 ± 8.3	9.2 ± 7.5	53.4 ± 8.8	6.8 ± 1.1	9.957	7.496
6	800	58	49.1 ± 12.5	37.2 ± 8.3	11.9 ± 9.4	6.95 ± 1.22	8.8 ± 1.5	1.002	5.798
6	1000	58	49.6 ± 12.8	37.2 ± 8.3	12.4 ± 9.7	1.11 ± 0.21	8.4 ± 1.5	0.1678	6.215
6	1200	58	49.6 ± 12.8	37.2 ± 8.3	12.4 ± 9.7	0.255 ± 0.039	8.3 ± 1.2	0.03903	6.005
6	1400	58	49.7 ± 12.8	37.2 ± 8.3	12.5 ± 9.8	0.0780 ± 0.0126	8.7 ± 1.3	0.01137	5.779
7	600	58	46.1 ± 11.0	37.2 ± 8.3	8.9 ± 7.3	60.0 ± 9.6	7.7 ± 1.2	9.986	6.601
7	800	58	49.3 ± 12.6	37.2 ± 8.3	12.2 ± 9.5	4.62 ± 0.84	7.9 ± 1.4	0.7422	6.536
7	1000	58	49.6 ± 12.8	37.2 ± 8.3	12.4 ± 9.7	0.605 ± 0.115	7.7 ± 1.4	0.09974	6.824
7	1200	58	49.7 ± 12.8	37.2 ± 8.3	12.5 ± 9.8	0.119 ± 0.018	7.8 ± 1.2	0.01932	6.406

TABLE 5.23. LED PRODUCTION CROSS SECTION WITH ALL $\sqrt{\hat{s}}$, σ_b, AND LED PRODUCTION CROSS SECTION WITH $\sqrt{\hat{s}} <$ M$_D$, σ_a, AT EACH MODEL POINT.

n	M_D (GeV)	σ_b (pb)	σ_a (pb)
2	600	32.96	30.15
2	800	10.44	10.26
2	1000	4.265	4.257
2	1200	2.056	2.056
2	1400	1.108	1.108
3	600	18.11	14.14
3	800	4.311	4.069
3	1000	1.411	1.399
3	1200	0.5676	0.5673
3	1400	0.2622	0.2622
4	600	12.79	7.554
4	800	2.278	1.966
4	1000	0.5967	0.5822
4	1200	0.2004	0.2000
4	1400	0.07953	0.07952
5	600	10.68	4.319
5	800	1.438	1.082
5	1000	0.3004	0.2837
5	1200	0.08405	0.08358
5	1400	0.02851	0.02851
6	600	9.957	2.550
6	800	1.002	0.6241
6	1000	0.1678	0.1506
6	1200	0.03903	0.03857
6	1400	0.01137	0.01136
7	600	9.986	1.489
7	800	0.7422	0.3676
7	1000	0.09974	0.08352
7	1200	0.01932	0.01890

CHAPTER 6

RESULTS

The 95% confidence level M_D exclusion limits and maximum sensitivities are determined by interpolating from the points just above the exclusion contour and the points just below the exclusion contour and they are listed in Table 6.1 to 6.3 for leading jet $|\eta_d| \leq 1.0$, $|\eta_d| \leq 2.5$ (excluding and including ICR: $1.1 \leq |\eta_d| \leq 1.5$). The maximum sensitivity is calculated by setting the observed number of events equal to the total background estimation. We also scale the signal cross section with a constant K-factor of 1.34 used in the the search for LED in dielectron and diphoton production[67] as reference to account for the next-to-leading order (NLO) effects since there is no NLO MC available. No error for the K-factor is considered. This value of the K-factor is for Drell-Yan from theory calculations[68]:

$$K = 1 + \frac{\alpha_s}{2\pi}\frac{4}{3}(1 + \frac{4}{3}\pi^2). \tag{6.1}$$

The M_D limit with signal contribution in the Q sample considered is also listed. The difference between it and the M_D limit without considering signal contribution in the Q sample is negligible, so the we do not consider the signal contribution in the Q sample for any of our QCD/cosmics background calculations and limit estimations. The exclusion contours are plotted in Figures 6.1 to 6.3 with comparison to M_D limits from different LEP experiments in $e^+e^- \to G\gamma$ channel[69]. As we can see, the limit with central leading jet is the highest comparing to the other two η_d ranges. This is because all the cuts are well defined in the central region. As for the cases with leading jet $|\eta_d| \leq 2.5$ (excluding and including ICR: $1.1 \leq |\eta_d| \leq 1.5$), the difference in the limit is very small since the background removal in the forward region is not significantly better than in the intercryostat region. So the results with central leading jet is the choice for publication.

TABLE 6.1. 95 % C.L. EXCLUSION LIMIT AND MAX. SENSITIVITY FOR THE LEADING JET $E_T/\not{E}_T > 150$ GeV, THE SECOND JET $E_T < 50$ GeV, AND $|\eta_d| \leq 1.0$.

n	2	3	4	5	6	7
M_D limit with signal contribution in Q sample considered (TeV)	0.890	0.736	0.685	0.640	0.627	0.618
M_D limit without considering signal contribution in Q sample (TeV)	0.886	0.734	0.683	0.639	0.626	0.617
M_D limit with K-factor applied on cross section (TeV)	0.987	0.797	0.728	0.661	0.646	0.629
Maximum M_D sensitivity (TeV)	0.886	0.734	0.683	0.639	0.626	0.617
Maximum M_D sensitivity with K-factor applied on cross section (TeV)	0.987	0.797	0.728	0.661	0.646	0.629

From Equation 2.2, the M_D limits can be translated in terms of R as shown in Tables 6.4 (no K-factor) and 6.5 (with K-factor).

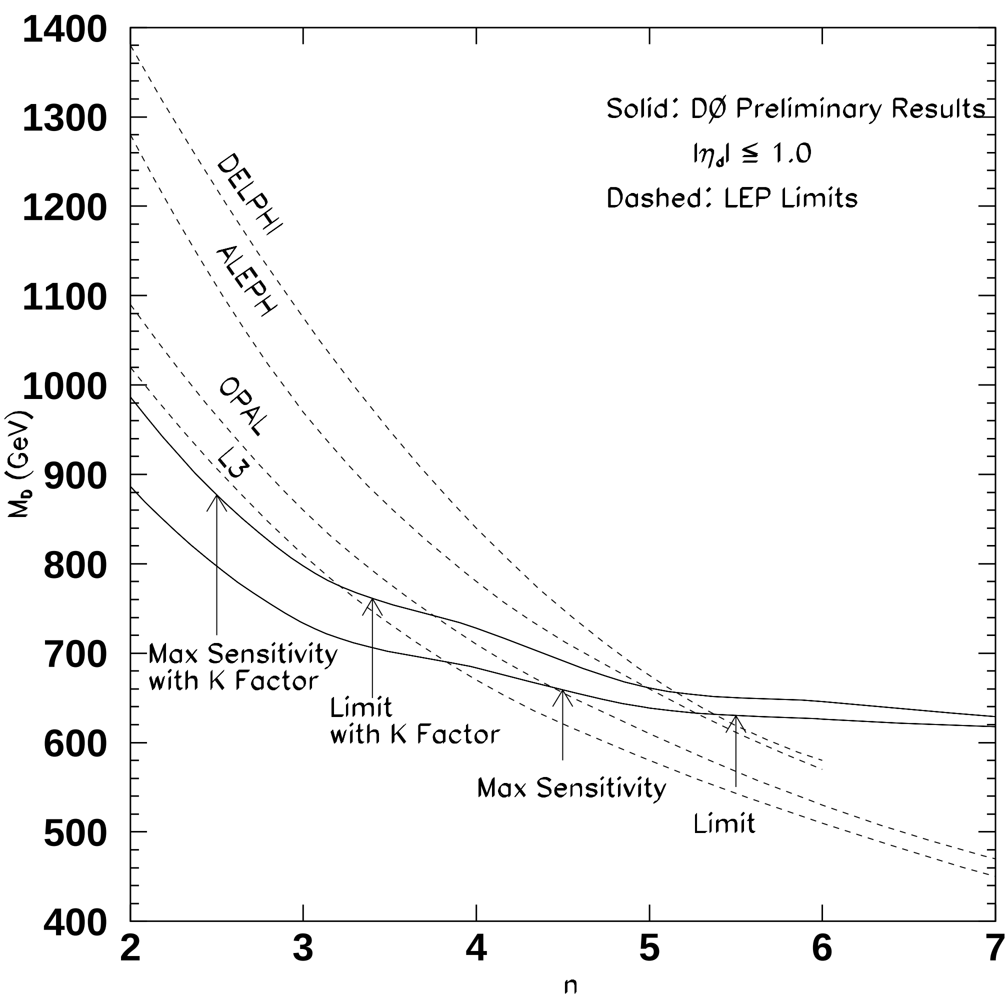

Figure 6.1. 95% C.L. exclusion contour for LED with the leading jet $E_T/\not{E}_T > 150$ GeV, the second jet $E_T < 50$ GeV, and $|\eta_d| \leq 1.0$.

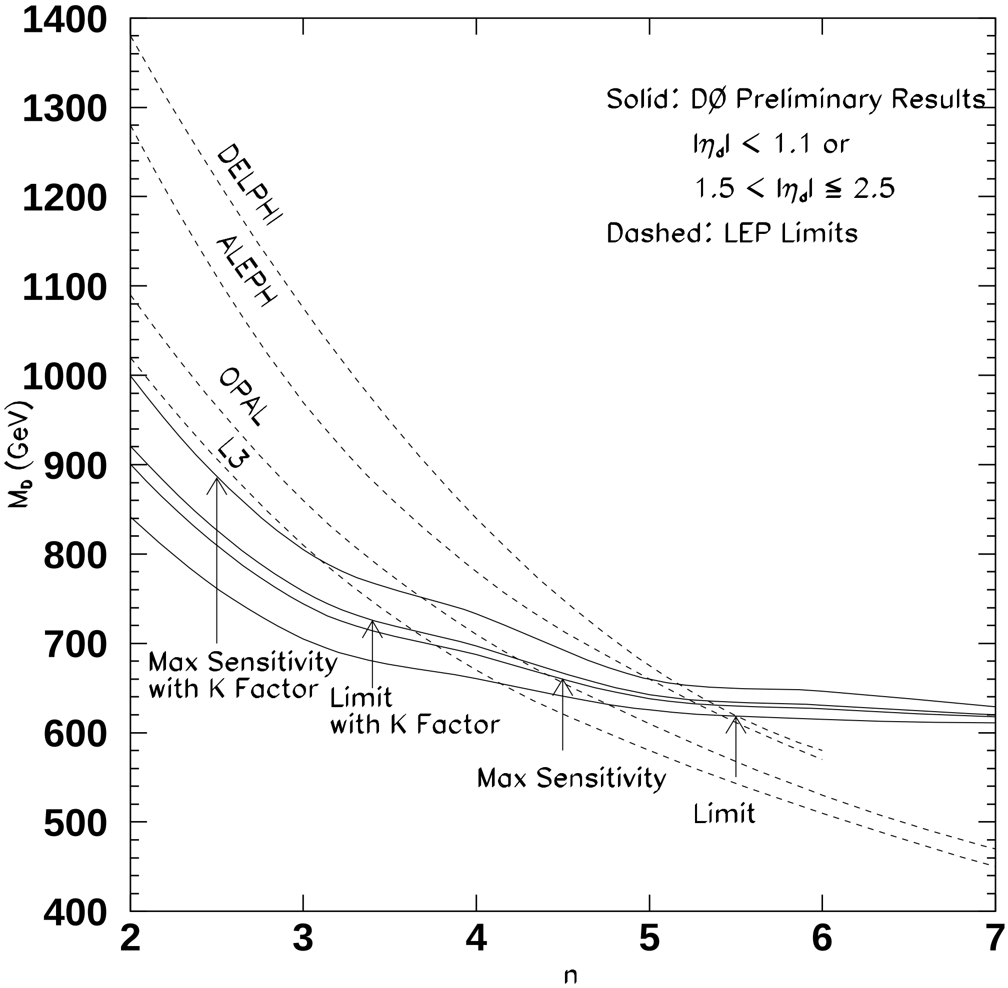

Figure 6.2. 95% C.L. exclusion contour for LED with the leading jet $E_T/\not{E}_T > 150$ GeV, the second jet $E_T < 50$ GeV, and $|\eta_d| < 1.1$ or $1.5 < |\eta_d| \leq 2.5$.

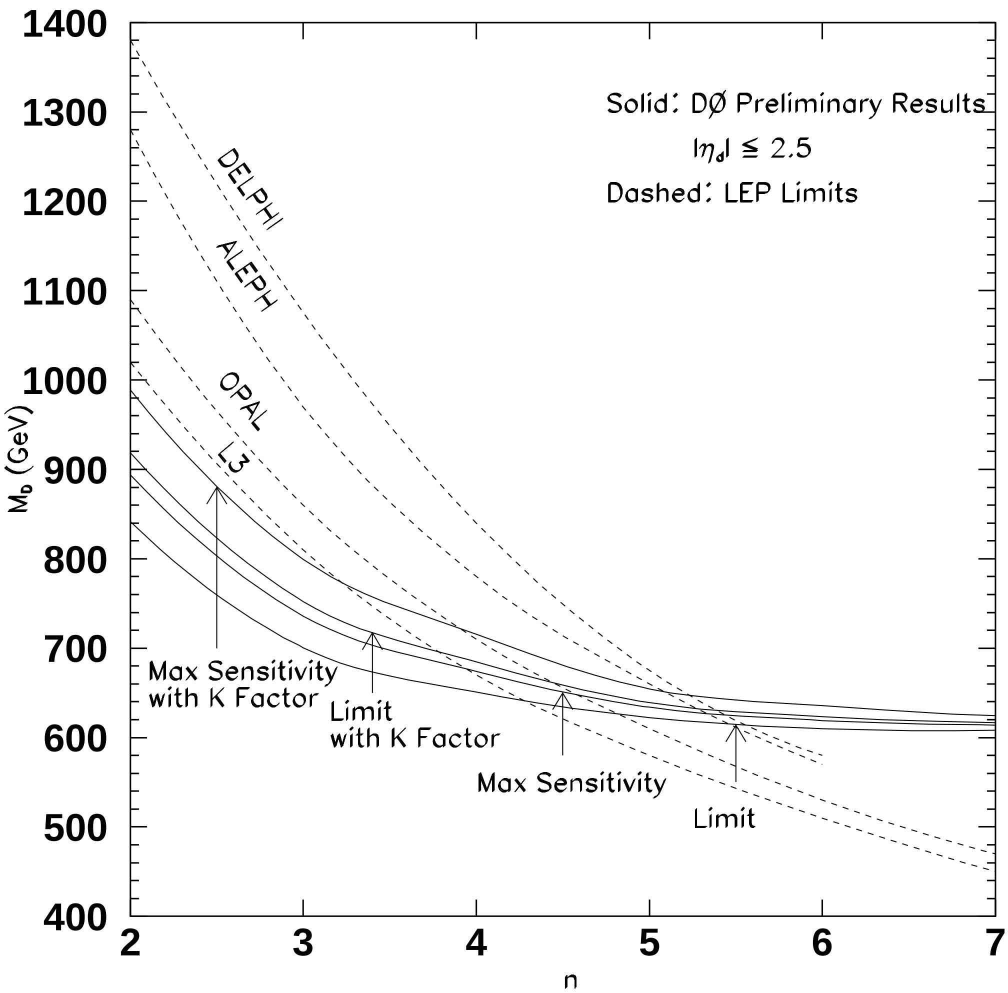

Figure 6.3. 95% C.L. exclusion contour for LED with the leading jet $E_T/\not{E}_T > 150$ GeV, the second jet $E_T < 50$ GeV, and $|\eta_d| \leq 2.5$.

TABLE 6.2. 95 % C.L. EXCLUSION LIMIT AND MAX. SENSITIVITY FOR THE LEADING JET $E_T/\not{E}_T > 150$ GeV, THE SECOND JET $E_T < 50$ GeV, AND $|\eta_d| < 1.1$ OR $1.5 < |\eta_d| \leq 2.5$.

n	2	3	4	5	6	7
M_D limit with signal contribution in Q sample considered (TeV)	0.840	0.704	0.660	0.625	0.614	0.611
M_D limit without considering signal contribution in Q sample (TeV)	0.842	0.705	0.660	0.625	0.615	0.611
M_D limit with K-factor applied on cross section (TeV)	0.921	0.758	0.697	0.643	0.631	0.620
Maximum M_D sensitivity (TeV)	0.900	0.744	0.687	0.638	0.626	0.618
Maximum M_D sensitivity with K-factor	1.00	0.805	0.733	0.660	0.646	0.629
applied on cross section (TeV)						

TABLE 6.3. 95 % C.L. EXCLUSION LIMIT AND MAX. SENSITIVITY FOR THE LEADING JET $E_T/\not{E}_T > 150$ GeV, THE SECOND JET $E_T < 50$ GeV, AND $|\eta_d| \leq 2.5$.

n	2	3	4	5	6	7
M_D limit with signal contribution in Q sample considered (TeV)	0.840	0.698	0.649	0.622	0.610	0.608
M_D limit without considering signal contribution in Q sample (TeV)	0.842	0.700	0.651	0.622	0.610	0.608
M_D limit with K-factor applied on cross section (TeV)	0.919	0.752	0.685	0.639	0.623	0.617
Maximum M_D sensitivity (TeV)	0.894	0.736	0.674	0.634	0.619	0.614
Maximum M_D sensitivity with K-factor applied on cross section (TeV)	0.989	0.800	0.716	0.654	0.636	0.624

TABLE 6.4. 95 % C.L. EXCLUSION LIMIT ON THE SIZE OF EXTRA DIMENTION, R, DERIVED FROM THE M_D LIMIT (NO K-FACTOR) WITH THE LEADING JET $E_T/\not{E}_T > 150$ GeV AND THE SECOND JET $E_T < 50$ GeV.

n	R limit with $\lvert\eta_d\rvert \leq 1.0$ (m)	R limit with $\lvert\eta_d\rvert < 1.1$ or $1.5 < \lvert\eta_d\rvert \leq 2.5$ (m)	R limit with $\lvert\eta_d\rvert \leq 2.5$ (m)
2	6.1×10^{-4}	6.8×10^{-4}	6.8×10^{-4}
3	6.0×10^{-9}	6.4×10^{-9}	6.5×10^{-9}
4	1.7×10^{-11}	1.8×10^{-11}	1.8×10^{-11}
5	5.3×10^{-13}	5.4×10^{-13}	5.5×10^{-13}
6	5.0×10^{-14}	5.1×10^{-14}	5.1×10^{-14}
7	9.1×10^{-15}	9.2×10^{-15}	9.3×10^{-15}

TABLE 6.5. 95 % C.L. EXCLUSION LIMIT ON THE SIZE OF EXTRA DIMENTION, R, DERIVED FROM THE M_D LIMIT (WITH K-FACTOR) WITH THE LEADING JET $E_T/\not{E}_T > 150$ GeV AND THE SECOND JET $E_T < 50$ GeV.

n	R limit with $\lvert\eta_d\rvert \leq 1.0$ (m)	R limit with $\lvert\eta_d\rvert < 1.1$ or $1.5 < \lvert\eta_d\rvert \leq 2.5$ (m)	R limit with $\lvert\eta_d\rvert \leq 2.5$ (m)
2	4.9×10^{-4}	5.7×10^{-4}	5.7×10^{-4}
3	5.2×10^{-9}	5.7×10^{-9}	5.7×10^{-9}
4	1.6×10^{-11}	1.7×10^{-11}	1.7×10^{-11}
5	5.0×10^{-13}	5.2×10^{-13}	5.3×10^{-13}
6	4.8×10^{-14}	4.9×10^{-14}	5.0×10^{-14}
7	8.9×10^{-15}	9.1×10^{-15}	9.1×10^{-15}

CHAPTER 7

CONCLUSION

We have searched for evidence of large extra-dimension in the jets + $\not{E}_T$ data set. The data are consistent with the Standard Model predictions and we find no evidence of LED in the jet + $\not{E}_T$ final state. Based on the consistency of the data with the Standard Model, we set limits on the fundamental mass scale M_D for LED. The limits we set compliment the LED results from LEP experiments at higher number of extra dimensions n.

This analysis is the first direct search of real graviton emission at hadron colliders in the jet + $\not{E}_T$ final state. Future experiments at the Tevatron and the Large Hadron Collider (LHC) will be able to provide higher sensitivity and bigger perturbative region for the LED search. An example of the maximum sensitivity estimation is shown in Table 7.1 for Run II Tevatron[5].We can see that the sensitivity is definitely higer. For LHC, the maximum sensitivity could reach multiple TeV.

TABLE 7.1. MAXIMUM M_D SENSITIVITY WHICH CAN BE REACHED BY REQUIRING $\sigma_{signal} > 205\ fb$ WITH THE ACCEPTANCE CUTS OF THE LEADING JET $E_T > 150$ GeV AND $|\eta_d| < 3$[5].

n	2	3	4	5
Max. M_D sensitivity for Tevatron $\sqrt{s} = 2$ TeV, $L > 300$ pb^{-1} (TeV)	1.40	1.15	1.00	0.90

APPENDIX A

A CANDIDATE EVENT

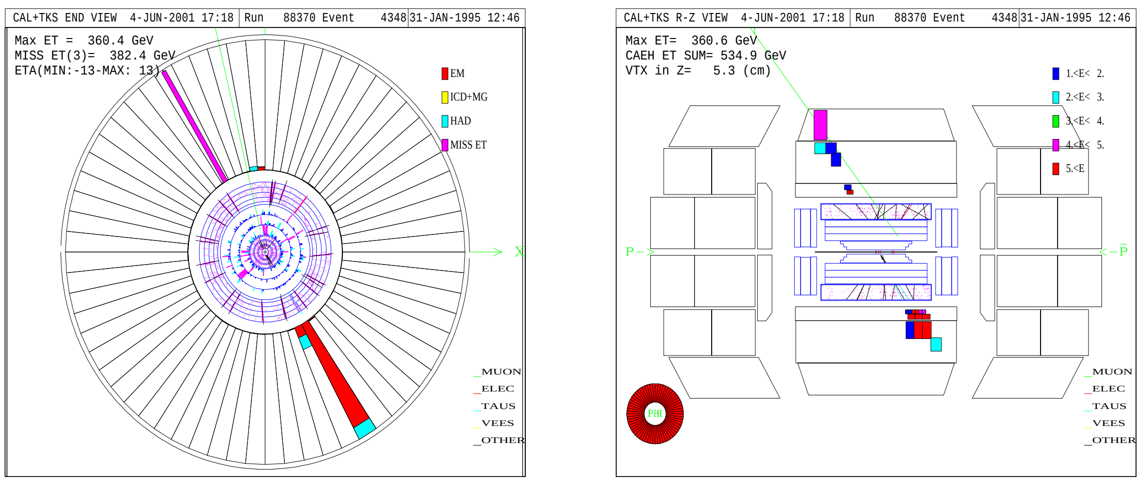

Figure A.1. End (left) and side (right) views of the candidate event with the highest $\not{E}_T$. The leading jet E_T = 466 GeV and $\not{E}_T$ = 443 GeV in this event.

BIBLIOGRAPHY

[1] S. L. Glashow, Nucl. Phys. **22**, 579 (1961); S. Weinberg, Phys. Rev. Lett. **19**, 1264 (1967); A. Salam, *Elementary Particle Theory*, ed. N. Svartholm, 367, (1968).

[2] C. Quigg, "Gauge Theories of the Strong, Weak, and Electromagnetic Interactions", Addison-Wesley (1983).

[3] P. W. Higgs, Phys. Lett. **12**, 132 (1964).

[4] N. Arkani-Hamed, S. Dimopoulos, and G. Dvali, Phys. Lett. B **429**, 263 (1998); preprint hep-ph/9807344.

[5] G. Giudice, R. Rattazzi, and J.D. Wells, Nucl. Phys. **B544**, 3 (1999).

[6] C.D. Hoyle, U. Schmidt, B.R. Heckel, E.G. Adelberger, J.H. Gundlach, D.J. Kapner, and H.E. Swanson, Phys. Rev. Lett. **86,** 1418 (2001).

[7] E. G. Floratos and G. K. Leontaris, Phys. Lett. **B 465,** 95 (1999)**;** A. Kehagias and K. Sfetsos, *ibid.* **472**, 39 (2001).

[8] T. Han, J.D. Lykken, and R.-J. Zhang, Phys. Rev. **D59**, 105006 (1999).

[9] J. Thompson, FERMILAB-TM-1909 (1994).

[10] DØ Collaboration, S. Abachi *et al.*, Nucl. Instr. and Meth. **A338**, 185 (1994), and references therein; S. Snyder, "The DØ Detector", DØ Internal Note 2500, 1995.

[11] http://www-d0.fnal.gov/online/RunI/Analysis/LogLum/run1_online_summary.html

[12] A. Clark *et al.*, Nucl. Instr. and Meth. **A315**, 193 (1992).

[13] J. F. Detoeuf *et al.*, Nucl. Instr. and Meth. **A279**, 310 (1989).

[14] A. Clark *et al.*, Nucl. Instr. and Meth. **A279**, 243 (1989).

[15] S. Wimpenny *et al.*, Nucl. Instr. and Meth. **A279**, 107 (1989).

[16] P. Franzini *et al.*, Nucl. Instr. and Meth. **A289**, 438 (1990).

[17] A. Spadafora *et al.*, Nucl. Instr. and Meth. **A315**, 279 (1992).

[18] C. Brown *et al.*, Nucl. Instr. and Methods, **A279**, 121 (1990).

[19] G. S. Gao and R. Partridge, IEEE Trans. Nucl. Sci. **38**(2), 286 (1992).

[20] J. Bantly *et al.*, "DØ Luminosity Monitor Constant for the 1994-1996 Tevatron Run", DØ Internal Note 3199, 1997 (unpublished).

[21] DØ Collaboration, M. Abolins *et al.*, IEEE Trans. Nucl. Sci. **36**(1), 384 (1989).

[22] DØ Collaboration, M. Abolins *et al.*, Nucl. Instr. and Meth. **A289**, 543 (1990).

[23] D. Edmunds, S. Gross, and P. Laurens, in *IEEE Nucl. Sci. Symp.* (IEEE, Norfolk, Va., 1994).

[24] J. Butler, "Main Ring Deadtime", DØ Internal Note 1682, 1993 (unpublished).

[25] M. Fortner *et al.*, IEEE Trans. Nucl. Sci. **38(2)**, 480 (1991).

[26] M. Goossens *et al.*, CERN Program Library Q100/Q101 (1995).

[27] G. Manning *et al.*, "DØ Software Documentation", Technical report, (URL: http://www-d0.fnal.gov/software/offline_document.ps)

[28] I. Adam *et al.*, "The Micro DST Format", DØ Internal Note 2327, 1995.

[29] N. J. Hadley, "Cone Algorithm for Jet Finding", DØ Internal Note 904 (unpublished); A. R. Baden and N. J. Hadley, "Jets and Kinematics", DØ Internal Note 957 (unpublished).

[30] B. Abbott *et al.*, "Jet Energy Scale at DØ", DØ Internal Note 3287, 1997.

[31] Z. J. Casilum and R. Hirosky, "Jet Reconstruction Efficiency", DØ Internal Note 3324 (unpublished).

[32] M. Bhattacharjee *et al.*, "Jet Energy Resolutions", DØ Internal Note 2887 (unpublished).

[33] M. Paterno, "A Monte Carlo Study of the DØ Calorimeter Missing E_T Resolution", DØ Internal Note 1374, 1992 (unpublished); M. Paterno, "A Study of the DØ Calorimeter $\not\!\!E_T$ Resolution Using Low E_T Jet Triggers", DØ Internal Note 1782, 1993 (unpublished).

[34] R. Kehoe, *Search for the Top Quark in Dielectron Final States at $\sqrt{s}$ = 1.8 TeV and Measurement of the Response of the DØ U/LAr Calorimeter to Jets*, Ph.D. Thesis, University of Notre Dame, 1997, (unpublished); S Youssef, Comp. Phys. Comm. **45**, 423 (1987).

[35] T. C. Awes *et al*, Nucl. Instr. and Methods **A311**, 130 (1991)

[36] R. J. Genik II, *The Search for Di-lepton Signatures from Squarks and Gluinos in $p\bar{p}$ Collisions at $\sqrt{s}$ = 1.8 TeV*, Ph.D. Thesis, Michigan State University, 1998 (unpublished).

[37] M. Narain and U. Heintz, "A Likelihood Test for Electron ID", DØ Internal Note 2386, 1994

[38] C. Gerber *et al*, "Muon Momentum Determination", DØ Internal Note 2140 (unpublished).

[39] J. Thompson, *Search for the Top Quark in Muon + Jets Channel at DØ*, Ph.D. Thesis, State University of New York at Stony Brook, 1994 (unpublished).

[40] E. Gallas, "The MTC Package (Muon Tracking in the DØ Calorimeter", DØ Internal Note 2066, 1995

[41] DØ Collaboration, B. Abbott *et al.*, Nucl. Instr. and Methods **A424**, 352 (1999)

[42] G. Manning *et al.*, "DØ Software Documentation", Calorimeter Reconstruction Section, DØ Internal Document (unpublished).

[43] B. Abbott *et al.*, "Jet Energy Scale (Cafix 5.1)", DØ Internal Note 3139 (unpublished).

[44] E. Popkov and R. Ruchti, "A Search for Squarks and Gluinos Using Jets and Missing Energy Signature", DØ Internal Note 3622, 2000

[45] L. Babukhadia *et al.*, "Hot cells and Jets at DØ (AIDA Cell Restoration)", DØ Internal Note 3139 (unpublished).

[46] A. L. Lyon and M. Paterno, "A Search for Squarks and Gluinos with the Jets and Missing Energy Signature in Run 1b", DØ internal note (unpublished).

[47] J. Butler *et. al.,* "Measurement of the Top Quark Production Cross Section Using Lepton + Jets Events", DØ Internal Note 2978, 1995 (unpublished).

[48] T. Marshall and H. Haggerty, "Crud Removal from Muon Drift Chamber Wires Using *Zap* Cleaning", DØ Internal Note 2556, 1995 (unpublished).

[49] J. M. Butler, "EF Muon ID for b-Tagging in the Post-Zap Era", DØ Internal Note 2602, 1995 (unpublished).

[50] C. Hays, "Run 1 Search for New Physics with the Two Jets Plus $\not\!\!E_T$ Final State", DØ Internal Note 3769, 2000 (unpublished).

[51] C. Hays, "Calorimeter-Based Cosmic Ray Rejection", DØ Internal Note 3814, 2001 (unpublished).

[52] D. Karmgard, "Search for Second Generation Scalar Leptoquarks in the $\mu\mu jj$ Channel", DØ Internal Note 3518, 1998

[53] M. Adams *et al.,* "Measurement of $Z\gamma \rightarrow \mu\mu\gamma$ and Limits on Trilinear $ZZ\gamma$ and $Z\gamma\gamma$ Couplings", DØ Internal Note 3230, 1997

[54] "GEANT Detector Description and Simulation Tool", CERN Program Library Long Writeup W5013, 1994.

[55] S. Eno, R. Genik, J. Hobbs, and L. Lueking, "The fast MC QSIM", DØ Internal Note 3587, 1999

[56] T. Sjostrand, Comp. Phys. Comm. **82**, 74 (1994)

[57] Z. Zhou, *Search for an mSUGRA Signature in the electron + jets + $\not\!\!E_T$ Final State in $p\bar{p}$ Collisions at $\sqrt{s} = 1.8$ TeV*, Ph.D. Thesis, Iowa State University, 2001 (unpublished).

[58] B. Klima, C. Stewart, "PJET - Parton Jets in the Monte Carlo", DØ Internal Note 905, 1989 (unpublished); D. Norman, "Some Comments on Pjets", DØ Internal Note 1065, 1990 (unpublished).

[59] A. Belyaev *et al.,* "Electroweak Production of Single Top Quarks at DØ", DØ Internal Note 3772, 2000

[60] S. Jadach, J. H. Kuhn, and Z. Was, Comp. Phys. Comm. **64**, 275 (1990); M. Jezabek *et. al.,* Comp. Phys. Comm. **70**, 69 (1992); S. Jadach *et. al.,* Comp. Phys. Comm. **76**, 361 (1993); P. Golonka, E. Richter-Was, and Z. Was, hep-ph/0009302, (2000); Z. Was, Nucl. Phys. Proc. Suppl. **98**, 96 (2001).

[61] DØ Collaboration, B. Abbott *et al.*, Phys. Lett. B513, 292 (2001).

[62] DØ Collaboration, B. Abbott *et al.*, Phys. Rev. Lett. {84} 2792 (2000).

[63] http://www-d0.fnal.gov/public/wz/xsection/xsection.html

[64] J. Lykken and K. Matchev, private code.

[65] I. Bertram *et al.*, "A Recipe for the Construction of Confidence Limits", DØ Internal Note 2775a, 1995 (unpublished)

[66] P. C. Bhat, H. B. Prosper, and S. S. Snyder, "Bayesian Analysis of Multi-Source Data", FERMILAB-Pub 96/397, 1997

[67] DØ Collaboration, B. Abbott *et al.*, Phys. Rev. Lett. {86} 1156 (2001); G. Landsberg "Search for Large Spatial Extra Dimensions Using Electrons and Photons", DØ Internal Note 3729, 2000

[68] V. Barger and R. Phillips, "Collider Physics", Perseus Pr, 1996.

[69] B. Vachon, preprint hep-ex/0201029 v2, (2002).